THÈSE DE DOCTORAT

École doctorale: *Physique et Sciences de la Matière*

Spécialité : **Physique des Plasmas**

Transport turbulent et néoclassique de quantité de mouvement toroïdale dans les plasmas de tokamak

Présentée par :
Jérémie Abiteboul

Thèse soutenue publiquement le 30 octobre 2012 devant le jury composé de :

Pr. Frank JENKO	Rapporteur
Dr. Olivier SAUTER	Rapporteur
Pr. Alain POCHEAU	Examinateur
Pr. Eric SONNENDRÜCKER	Examinateur
Dr. Philippe GHENDRIH	Directeur de thèse
Dr. Virginie GRANDGIRARD	Responsable CEA

Laboratoire d'accueil :
Institut de **R**echerche sur la **F**usion par confinement **M**agnétique
CEA – Cadarache
13108 Saint-Paul-lez-Durance, France

Oct 2009 – Oct 2012

Abstract

The goal of magnetic confinement devices such as tokamaks is to produce energy from nuclear fusion reactions in plasmas at low densities and high temperatures. Experimentally, toroidal flows have been found to significantly improve the energy confinement, and therefore the performance of the machine. As extrinsic momentum sources will be limited in future fusion devices such as ITER, an understanding of the physics of toroidal momentum transport and the generation of intrinsic toroidal rotation in tokamaks would be an important step in order to predict the rotation profile in experiments. Among the mechanisms expected to contribute to the generation of toroidal rotation is the transport of momentum by electrostatic turbulence, which governs heat transport in tokamaks. Due to the low collisionality of the plasma, kinetic modeling is mandatory for the study of tokamak turbulence. In principle, this implies the modeling of a six-dimensional distribution function representing the density of particles in position and velocity phase-space, which can be reduced to five dimensions when considering only frequencies below the particle cyclotron frequency. This approximation, relevant for the study of turbulence in tokamaks, leads to the so-called gyrokinetic model and brings the computational cost of the model within the presently available numerical resources. In this work, we study the transport of toroidal momentum in tokamaks in the framework of the gyrokinetic model. First, we show that this reduced model is indeed capable of accurately modeling momentum transport by deriving a local conservation equation of toroidal momentum, and verifying it numerically with the gyrokinetic code GYSELA. Secondly, we show how electrostatic turbulence can break the axisymmetry and generate toroidal rotation, while a strong link between turbulent heat and momentum transport is identified, as both exhibit the same large-scale avalanche-like events. The dynamics of turbulent transport are then analyzed and, although the conventional gyro-Bohm scaling is recovered on average, local processes are found to be clearly non-diffusive. The impact of scrape-off layer flows on core toroidal rotation is also analyzed by modifying the boundary conditions in GYSELA. Finally, the equilibrium magnetic field in tokamaks, which is not rigorously axisymmetric, provides another means of breaking the toroidal symmetry, through purely collisional processes. This effect is found to contribute significantly to toroidal momentum transport and can compete with the turbulence-driven toroidal rotation in tokamaks.

Résumé

L'objectif de la fusion par confinement magnétique, et notamment du tokamak, est de produire de l'énergie à partir des réactions de fusion nucléaire, dans un plasma à faible densité et haute température. Expérimentalement, une amélioration de la performance des tokamaks a été observée en présence de rotation toroïdale. Or, les sources extérieurs de quantité de mouvement seront très limitées dans les futurs tokamaks, et notamment ITER. Une compréhension de la physique de la génération intrinsèque de rotation toroïdale permettrait donc de prédire les profils de rotation dans les expériences futures. Parmi les mécanismes envisagés, on s'intéresse ici à la génération de rotation par la turbulence, qui domine le transport de la chaleur dans les tokamaks. Les plasmas de fusion étant faiblement collisionnels, la modélisation de cette turbulence suppose un modèle cinétique décrivant la fonction de distribution des particules dans l'espace des phases à six dimensions (position et vitesse). Cependant, ce modèle peut être réduit à cinq dimensions pour des fréquences inférieures à la fréquence cyclotronique des particules. Le modèle gyrocinétique qui découle de cette approximation est alors accessible avec les ressources numériques actuelles. Les travaux présentés portent sur l'étude du transport de quantité de mouvement toroïdale dans les plasmas de tokamak, dans le cadre du modèle gyrocinétique. Dans un premier temps, nous montrons que ce modèle réduit permet une description précise du transport de quantité de mouvement en dérivant une équation locale de conservation. Cette équation est vérifiée numériquement à l'aide du code gyrocinétique GYSELA. Ensuite, nous montrons comment la turbulence électrostatique peut briser l'axisymétrie du système, générant ainsi de la rotation toroïdale. Un lien fort entre transport de chaleur et transport de quantité de mouvement est mis en évidence, les deux présentant des avalanches à grande échelle. La dynamique du transport turbulent est analysée en détail et, bien que l'estimation standard gyro-Bohm soit vérifiée en moyenne, des phénomènes on-diffusifs sont observés. L'effet des écoulements de bord du plasma sur la rotation toroïdale dans le cœur est étudié en modifiant les conditions aux bords dans le code GYSELA. Enfin, le champ magnétique d'équilibre, qui n'est pas rigoureusement axisymétrique, peut également participer à la génération de rotation toroïdale, via des mécanismes purement collisionnels. Dans un tokamak, cet effet est suffisamment important pour entrer en compétition avec la rotation générée par la turbulence électrostatique.

Contents

List of Figures

Chapter 1

Introduction

> Continued greenhouse gas emissions at or above current rates would cause further warming and induce many changes in the global climate system during the 21^{st} century that would very likely be larger than those observed during the 20^{th} century.
> (...) Societies can respond to climate change by *adapting* to its impacts and by reducing greenhouse gas emissions (*mitigation*) thereby reducing the rate and magnitude of change.
> (...) Unmitigated climate change would, in the long term, be likely to exceed the capacity of natural, managed and human systems to adapt. Reliance on adaptation alone could eventually lead to a magnitude of climate change to which effective adaptation is not possible, or will only be available at very high social, environmental and economic costs.
>
> *Fourth Assessment Report of the Intergovernmental Panel on Climate Change*, 2007. IPCC, Geneva, Switzerland

Nuclear fusion has emerged over the course of the 20th century as a possible source of energy for our future. In particular, the *tokamak* concept is considered as a likely candidate to satisfy mankind's growing energy demands. In this introductory chapter, the basics of controlled nuclear fusion are briefly reviewed, with a special emphasis on the tokamak configuration. Next, the important issue of toroidal rotation in tokamaks, which is the main topic of this thesis, is presented. Finally, the question of the models available to describe the collective processes responsible for momentum transport in fusion plasmas is addressed.

1.1 Controlled nuclear fusion

1.1.1 Nuclear fusion

For light elements, the fusion of two nuclei to form a larger one can lead to the release of energy, because the binding energy of the newly created atom will be greater than the sum of the binding energies of the two original nuclei. This is best illustrated by the positive slope for light nuclei (especially hydrogen and helium isotopes) of the binding energy curve, Fig. 1.1, which represents the *average* binding energy per nucleon as a function of the number of nucleons. Symmetrically, the negative slope for heavier nuclei implies that the fission of such an atom (for instance a Uranium atom) into two lighter nuclei can lead

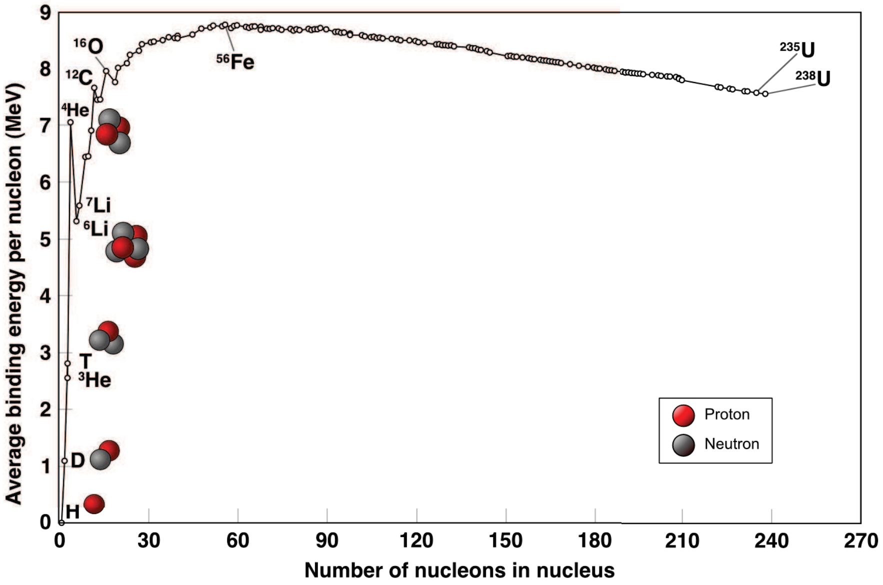

Figure 1.1: Average binding energy per nucleon as a function of the number of nucleons per nucleus. Only the points corresponding to the most abundant isotopes are shown. The iron atom with A=56 nucleons is the most tightly bounded nucleus.

to released energy. This latter process is the basis for nuclear fission reactors, while the former is the energy source which fuels stars.

Of the various reactions able to produce energy through the fusion of two nuclei, the fusion of a deuterium nucleus (D) with a tritium nucleus (T) has the highest cross-section at low energies, i.e. the highest probability for the reaction to occur. This reaction leads to the creation of a helium atom and a neutron, with each product of the reaction carrying a part of the liberated energy:

$$ {}^{2}_{1}D + {}^{3}_{1}T \longrightarrow {}^{4}_{2}He\,(3.5MeV) + {}^{1}_{0}n\,(14.1MeV) \tag{1.1} $$

The cross-section for this reaction is maximum for energies of approximately 70keV, and drops sharply below 10keV, which appears as a minimum energy for a nuclear fusion reactor to be viable. In order to have a significant amount of particles at such energies, the reactants must be heated up to temperatures above several keVs, i.e. around $10^8 K$ [1]. At such temperatures, the hydrogen atoms will be fully ionized, corresponding to the *plasma* state of matter [2].

---

[1] We assume here that *thermal* methods are used to obtain nuclear fusion, meaning that the reactant is assumed to be near thermodynamic equilibrium with a particle distribution “close” to a Maxwellian. In this scenario, the cross-section of the reaction will be significant mainly for the tails of the distribution. Another possibility is via *non-thermal* methods where the fusion process relies on the fact that at least one of the reactants has a significantly non-Maxwellian distribution, for example with a large population of highly energetic particles with a higher cross-section. However, such methods exhibit fundamental limitations due to the problem of power recycling [Rid97].

[2] On Earth, plasmas are found naturally only in the form of auroras (Northern and Southern polar lights). However, they represent roughly 99% of visible matter in the Universe, including stars, the interstellar medium and intergalactic space.

1.1.2 The Lawson criterion

Although a fraction of the fusion energy is used to heat the plasma and maintain a suitable temperature for fusion reactions, additional heating is required, performed either by injecting energetic particles or by radio-frequency heating. As the aim is to produce energy from nuclear fusion reactors, the key figure of merit is the *amplification factor*, i.e. the ratio between the power produced by nuclear fusion reactions and the external power necessary to heat the plasma. Intuitively, the key parameters one can maximize to obtain a favorable ratio are

- the ion temperature T_i of the plasma, which in turn increases the cross-section of the D-T reaction,
- its density n, which increases the number of reactions,
- the quality of the energy confinement in the plasma, which is directly linked to the energy input required to maintain the plasma at a given temperature.

The latter is usually described in terms of the confinement time τ_E, which corresponds to the characteristic time for the plasma to cool down in the absence of any heat source.

Taking into account the main sources and sinks of energy in the system, one can obtain a direct relation between the amplification factor Q and these three operational parameters [Law57]. Assuming that an amplification factor of at least 40 is necessary for an economically viable fusion reactor, one finds a condition on the triple product of the three parameters:

$$n\,T_i \tau_E \geq 3.10^{21}\,keV\,s^{-1} \tag{1.2}$$

The quantities considered in this crude estimate are the volume averaged temperature and density. Note that this condition can be significantly modified when taking into account other factors, such as density and temperature profiles, or impurity concentration.

1.1.3 The tokamak concept for plasma confinement

Several possibilities can be considered in order to reach the Lawson criterion, depending on how one confines the plasma. In order to maximize the cross-section of the D-T reaction, the optimal temperature range is $T_i \gtrsim 20\,keV$. Thus, with two parameters remaining in the triple product, two main directions can be explored[3] to satisfy the Lawson criterion:

- *Inertial confinement* aims at obtaining very dense plasmas ($n \sim 10^{31} m^{-3}$) with low energy confinement time ($\tau_E \sim 10^{-11} s$). This is achieved by compressing a fuel target consisting of a deuterium-tritium pellet. The energy necessary for the compression of the pellet is usually delivered by intense laser beams.
- *Magnetic confinement* uses the fact that the trajectories of the charged particles in the plasma can be guided by magnetic fields. The plasmas produced in this case are at lower densities ($n \sim 10^{20} m^{-3}$) but the confinement time is larger ($\tau_E \sim 1s$). Of the numerous magnetic configurations that can be considered to confine the plasma, the *tokamak*[4] design is considered at the moment to be the most promising.

---

[3] Note that a third method of confinement is theoretically available: in stars, plasma confinement is ensured by gravity. However, the mass needed to satisfy the Lawson criterion through gravitational confinement is such that this form of confinement is not accessible for nuclear fusion reactors.

[4] From the Russian ***To****roidal'naya* ***ka****mera s* ***ma****gnitnymi* ***k****atushkami*, literally "toroidal chamber with magnetic coils".

In the tokamak configuration, the plasma is confined in a toroidal chamber by a helical magnetic field, as can be seen in Fig. 1.2, which shows a schematic view of a tokamak. The toroidal component of the magnetic field is generated by external coils, while its poloidal component is generated by a toroidal plasma current. When inductive, this current is obtained by varying the magnetic flux in the central solenoid, while the plasma acts as the secondary winding of a transformer. Assuming only collisional transport, this configuration provides a very good confinement of the plasma. However, experiments have shown that the energy confinement time is lower than expected from collisional theory, and is in fact dominated by micro-scale turbulence in the plasma.

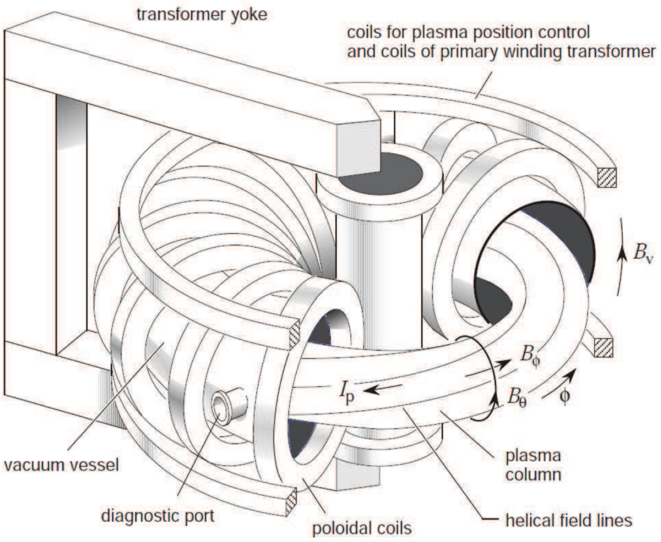

Figure 1.2: Schematic view of a tokamak

Since the first tokamaks operated in the late 1950s at the Kurchatov Institute in Moscow, many devices have been built throughout the world to explore various operational regimes and technologies. At the moment, the largest device is the Joint European Torus (JET) tokamak, which has reached an amplification factor $Q \sim 0.7$. The next step on the path to a functioning nuclear reactor is the experimental tokamak ITER, currently being built in Cadarache (France), which aims to reach $Q = 10$, demonstrating the capability of tokamaks to produce more fusion power than the power required to operate them.

1.2 Toroidal rotation in tokamaks

The issue of toroidal rotation in tokamaks, which is the focus of this thesis, has been identified in recent years as an important factor for the performance of fusion reactors (for a review of theoretical and experimental results, see [deG09]). Experiments have shown that a sufficient level of toroidal rotation can stabilize certain magnetohydrodynamic (MHD) modes, such as the resistive wall mode [BW94] or the neoclassical tearing mode [PPJ+08]. Moreover, toroidal rotation impacts energy transport through the saturation of turbulence by sheared flows [BDT90], and can therefore contribute to the formation and sustainment of improved confinement regimes such as transport barriers. Thus, toroidal rotation can have a significant impact on the energy confinement time, and therefore on the capability of fusion reactors to produce energy.

In most present experiments, toroidal rotation is largely controlled by external sources, namely through the torque due to neutral beam injection (NBI). However, for future experiments such as ITER, as well as for reactors, the torque from NBI is expected to be small. Fortunately, in the absence of external torque, toroidal rotation has been observed experimentally. This phenomenon is referred to as *spontaneous* or *intrinsic* rotation, and has been reported in a large number of tokamaks. Attempts have been made to unify the different experimental results, leading for instance to the so-called Rice scaling [RICd+07] for the increased level of toroidal rotation after the transition to an improved confinement regimes.

However, no clear picture has emerged so far as to the exact process generating intrinsic rotation, as many different physical effects may play a role, such as MHD activity, micro-turbulence, plasma-wall interaction or the effects of fast particles. A better understanding of the physics of intrinsic rotation, and more generally of momentum transport, would be an important step in order to anticipate the level of rotation and therefore the performance of future devices. This thesis addresses the issue of intrinsic generation and transport of toroidal rotation by electrostatic micro-turbulence, as well as the role of collisional processes due to the non-axisymmetry of the magnetic configuration.

1.3 Modeling turbulence in weakly collisional plasmas

The description of micro-turbulence in a plasma requires a model solving self-consistently (i) Maxwell's equations for the dynamics of the electromagnetic fields, and (ii) the collective response of the plasma. For the latter, the most accurate model would be to write Newton's equation of motion for each particle in the plasma, including relativistic corrections for the most energetic particles. With this approach, one obtains six equations – for the three dimensions in space and in velocity – for each particle, and these equations are all coupled through Maxwell's equations. As tokamak plasmas have a density of approximately $10^{20}m^{-3}$, such a many-body problem is clearly not tractable numerically with the current computing resources, and will remain out of reach in the foreseeable future. Therefore, reasonable approximations must be made to obtain more accessible models. One specificity of fusion plasmas is the very large diversity of scales in the physics, as illustrated by Fig. 1.3. To study these scales, various levels of approximation can be adopted, leading to a hierarchy of models for the plasma response.

As it is not possible to model each particle individually, the next step is to use a statistical description. The information on the position and velocity of each individual particle is not necessary to describe plasma behavior and can be replaced by the *probability* of finding a particle at a given position and velocity. In this context, the important quantity becomes the probability distribution function $F_s(\mathbf{x}, \mathbf{v}, t)$ in six dimensions, for each species s. This description assumes an averaging – in space and time – of the behavior of individual charged particles. Thus kinetic theory allows one to model collective processes in fusion plasmas at scales larger than the Debye length (roughly $10^{-4}m$), which corresponds to the characteristic scale over which electric charges are shielded. The general form of the equation for the distribution function is the kinetic equation

$$\frac{dF_s}{dt} = \mathcal{C}(F_s) \tag{1.3}$$

where $\mathcal{C}$ is a collision operator which retains the statistically averaged effect of individual collisions. Eq. (1.3) is given different names – Boltzmann equation, Fokker-Planck equation – depending on the physics contained by the collision operator. When $\mathcal{C}(F_s) = 0$,

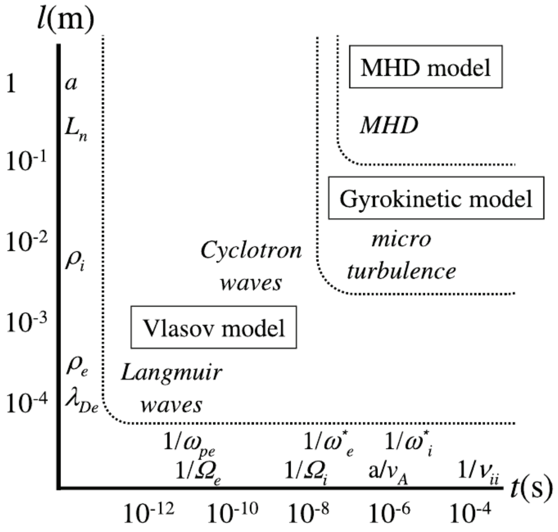

Figure 1.3: Diversity of scales in fusion plasmas, with the domains of applicability of Vlasov, gyrokinetic and MHD models. Here, ω_{ps} is the plasma oscillation frequency, Ω_s is the cyclotron frequency, ω_s^* is the diamagnetic rotation frequency, v_A is the Alfvén velocity, ν_{ii} is the ion-ion collision frequency, λ_{Ds} is the Debye length, ρ_s is the Larmor radius, L_n is the characteristic gradient length of the equilibrium density profile, a is the plasma size and s denotes the particle species. (figure from [GIVW10])

Eq. (1.3) is often referred to as the Vlasov equation and corresponds to the case of a collisionless plasma. Solving Eq. (1.3) and the Maxwell equations allows one to describe plasma phenomena in tokamaks at all relevant time and length scales. However, the numerical cost required to simulate such a model remains large, as the evolving quantity is a 6D distribution function. The kinetic model can be further simplified to 5 dimensions for the study of plasma turbulence in the presence of a strong magnetic field. This reduction, which leads to the so-called gyrokinetic model, will be the main topic of chapter 2.

Finally, the last family of models in the hierarchy of models for plasma response corresponds to the fluid approach. By integrating the kinetic equation over velocity space, one obtains equations for the so-called fluid moments, which are 3D quantities of the form $\int F_s \mathbf{v}^k d\mathbf{v}$ where k is an integer. The first moments correspond to well-known physical quantities: density, flow velocity, pressure. Importantly, the evolution equation for the moment of rank k contains the moment of rank $k+1$. In principle, this leads to an infinite set of moment equations, containing all the information from the kinetic equation (1.3). Thus, the major difficulty of the fluid approach is the *closure* problem, as an additional approximation must be made in the model to close the system and obtain a finite set of fluid equations.

The closure can be relatively easy and efficient for neutral fluids or plasmas close to thermodynamic equilibrium, where a Maxwellian distribution can be assumed for F_s, which can be described by its first moments. Then, one only has to solve for a finite – usually very small – number of unknowns in 3D space, which reduces greatly the numerical cost compared to kinetic simulations. However, tokamak plasmas are weakly collisional systems and can be expected to depart significantly from thermodynamic equilibrium. This can be understood by an estimate of the spatial scale of collisions, which can be obtained from the deviation angle of Coulomb collisions. This angle is a function of two characteristic lengths, namely the distance of closest approach and the impact parameter[5]. The distance of closest approach between two particles is the Landau distance, corresponding to the distance at which all of a particle's kinetic energy has been converted to potential energy, leading to

$$\lambda_L = \frac{q^2}{4\pi\epsilon_0 T} \tag{1.4}$$

where q is the species charge, ϵ_0 is the vacuum permittivity and T is the relative energy of the colliding nuclei. The value of the Landau distance λ_L for deuterium particles at an energy of $10keV$ is of the order of $10^{-12}m$. The deviation angle can be expressed as $\theta = \lambda_L/b$ where b is the impact parameter. The characteristic length scale of collisions is then obtained by integrating θ^2 over the impact parameter b, from λ_L to the maximal distance of interaction, which corresponds in plasmas to the Debye length, above which individual charges are screened by the plasma. From this calculation, a simple estimate of the characteristic collision length can be obtained as

$$L_{coll} \sim \frac{\lambda_l^3}{\lambda_L^2} \tag{1.5}$$

where $\lambda_l = n^{-1/3}$ is the mean distance between two particles, referred to as the Loschmidt distance. For the typical densities of magnetized fusion plasmas, $\lambda_l \sim 10^{-7}$. Thus, L_{coll} is of the order of the km, much larger than the largest spatial scale considered in tokamak plasmas, which corresponds to the size of the tokamak. To summarize, the various lengths can be ordered as follows

$$\lambda_L \ll \lambda_l \ll \lambda_D \ll L_{turb} \ll L_{coll} \tag{1.6}$$

where L_{turb} is the characteristic scale of micro-turbulence. As a consequence, collisions are expected to have very little impact and one cannot assume that the plasma will remain close to thermodynamic equilibrium. Indeed, no completely satisfactory closure has been found for tokamak plasmas, and the results from fluid simulations show strong discrepancies with kinetic simulations when dealing with micro-scale turbulence [DBB⁺00].

As a conclusion, it appears that while fluid models provide a convenient and numerically cheap solution to model the plasma response, kinetic modeling is mandatory for accurate simulations of collective behavior in weakly collisional tokamak plasmas. The gyrokinetic model, which will be presented in chapter 2, provides a reduced version of the general kinetic model, well-suited for the study of turbulence in strongly magnetized plasmas and compatible with the available computing resources.

1.4 Outline of this manuscript

The topic of this thesis is the investigation of toroidal momentum transport in tokamak plasmas through turbulent and collisional – referred to as *neoclassical* in the magnetic confinement fusion literature – processes. The gyrokinetic model used for this study is described in detail in the following chapter 2. The key underlying assumptions and the theoretical basis of the model are discussed. The numerical code GYSELA, based on the gyrokinetic model, is presented, with an emphasis on the modeling choices and a brief description of the numerical methods. An example of the general results obtained in a

---

[5] The impact parameter is defined as the hypothetical distance of closest approach between two particles if the particles did not interact.

Gysela simulation is also given. In order to validate the gyrokinetic model, both theoretically and numerically, local conservation laws are derived analytically in chapter 3 for charge density, energy and toroidal angular momentum. The latter equation is also useful in order to identify the different fluxes governing toroidal momentum transport. The local conservation of toroidal momentum is tested numerically with the gyrokinetic code Gysela, along with the force balance equation, demonstrating that the gyrokinetic model achieves an accurate description of mean flows in tokamaks. The transport of momentum and generation of *intrinsic* rotation by electrostatic turbulence is investigated in chapter 4 by performing simulations from a vanishing initial profile of toroidal rotation and with no external momentum source. The characteristics of turbulent momentum transport, and the relation with heat transport, which both exhibit large-scale avalanche-like events, are analyzed through a statistical description in steady-state simulations. The non-local properties of turbulent transport are discussed in chapter 5. Despite the observation of large-scale transport events and the strong poloidal asymmetry of turbulence, the conventional gyro-Bohm scaling can be recovered for both heat and momentum transport. The impact on toroidal rotation of edge flows, critical because of the local conservation of toroidal momentum in the core plasma, is also investigated. Finally, neoclassical momentum transport, in the presence of a non-axisymmetric magnetic field, is presented in chapter 6. This breaking of toroidal symmetry leads to a friction on the toroidal velocity, which can be predicted theoretically in a number of limit cases. Simulations with the Gysela code achieve a self-consistent study of both turbulence and neoclassical momentum transport, allowing for a qualitative comparison with both theory and experimental results.

Chapter 2

The gyrokinetic model for plasma turbulence

> Earl Ferrers – *My Lords, what kind of thermometer reads a temperature of 140 million degrees centigrade without melting?*
> Viscount Davidson – *My Lords, I should think a rather large one.*
>
> ---
>
> Debate on the JET Nuclear Fusion Project,
> United Kingdom House of Lords, March 3, 1987

This chapter is devoted to the presentation of the main tools, both theoretical and numerical, used for the study of micro-turbulence in tokamak plasmas. The first part of this chapter, section 2.1, is dedicated to a brief description of the magnetic configuration of the tokamak, including the system of coordinates used throughout the manuscript, and of the particle trajectories in this configuration. Next, the gyrokinetic model is detailed in section 2.2, with an emphasis on the different approximations made in order to reduce the complete kinetic model to a more tractable system of equations, adapted to the study of electrostatic turbulence in fusion plasmas. The gyrokinetic code GYSELA, used for the simulation results included in the present manuscript, is presented in section 2.3. The important modeling choices are discussed, the collision operator and gyro-averaging operator implemented in the code are described in detail, and the numerical methods used are briefly introduced. Finally, to illustrate the numerical results which can be obtained by gyrokinetic simulations, a GYSELA simulation is described in section 2.4.

2.1 Magnetic configuration and particle trajectories

2.1.1 Magnetic configuration

As outlined in section 1.1.3, a tokamak plasma is contained in an axisymmetric toroidal vessel and confined by a helical magnetic field. The general form of the magnetic field in an axisymmetric tokamak is

$$\mathbf{B} = I(\chi)\nabla\varphi + \nabla\varphi \times \nabla\chi \tag{2.1}$$

where χ is the opposite of the poloidal magnetic flux [DHCS91], which is a label of magnetic flux surfaces, φ is the geometric angle in the (axisymmetric) toroidal direction and I is

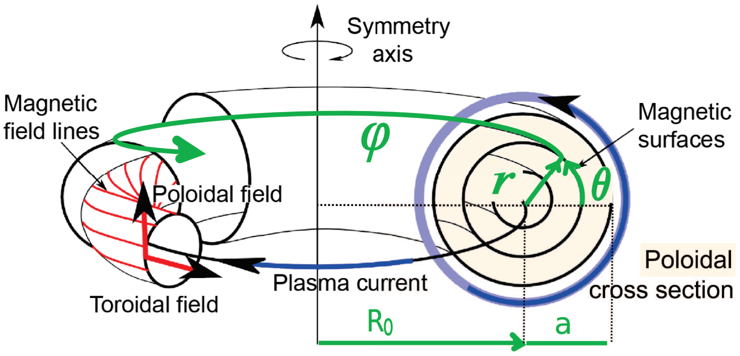

Figure 2.1: The tokamak magnetic configuration and the toroidal coordinate system (r, θ, φ). The geometry of the torus can be described by its minor radius a and major radius R_0 (at the magnetic axis)

a flux function. We can define a poloidal angle θ such that the safety factor q is only a function of χ:

$$q(\chi) \equiv \frac{\mathbf{B} \cdot \nabla\varphi}{\mathbf{B} \cdot \nabla\theta} \tag{2.2}$$

The safety factor q describes the pitch of the magnetic field lines, and can be understood as the number of toroidal revolutions performed for one poloidal revolution following a magnetic field line.

An adequate system of toroidal coordinates in tokamak geometry can then be defined by (χ, θ, φ). Note that the poloidal angle obtained here is not the geometric poloidal angle and depends on the structure of the magnetic field. This corresponds to so-called *flux coordinates*, designed for the magnetic field lines to be straight on a given flux-surface. More details on this system of coordinates can be found in appendix A. The Jacobian of the metric obtained with this coordinate system is $\mathcal{J}_s = 1/(\mathbf{B} \cdot \nabla\theta)$, where s stands for space, as opposed to the Jacobian in velocity space $\mathcal{J}_v$ (see section 2.2). As manipulating a flux as a variable is not always practical, the coordinate χ can be replaced by a radial coordinate r, also a label of flux surfaces, such that χ is a function of r only. This system of toroidal coordinates is represented in Fig. 2.1.

In the following, a simplified magnetic geometry will be adopted, with the poloidal cross-sections of the magnetic surfaces (see Fig. 2.1) taken as circular and concentric.

2.1.2 Particle trajectories

As tokamak plasmas are weakly collisional, with a very large mean free path between collisions, particle trajectories are governed by the electromagnetic field. In a *uniform* magnetic field, the motion of a particle can be described by

- a free streaming motion in the direction parallel to the magnetic field lines, at an unperturbed velocity $v_\parallel$
- a rapid cyclotron rotation around the magnetic field. All particles of a given species s will perform this rotation at the same *gyrofrequency* (or cyclotron frequency) $\Omega_s = e_s B/m_s$, where B is the intensity of the magnetic field, e_s and m_s are the species mass and charge. The radius of the cyclotron motion is the *Larmor radius* $\rho_c = m_s v_\perp/(e_s B)$ where $v_\perp$ is the velocity of the particle in the direction perpendicular to the magnetic field.

The presence of non-uniform or time-varying electromagnetic fields leads to additional *drift* velocities. In the most general case, the derivation of these drifts is not tractable analytically. One specific case where the drifts can indeed be derived is the context of *adiabatic theory*, which assumes slow variations (in space and time) of the electromagnetic fields, compared to the gyromotion of the particle. In terms of time variations, this corresponds to the conditions

$$\left|\frac{\partial \log B}{\partial t}\right| \ll \Omega_s \quad ; \quad \left|\frac{\partial \log E}{\partial t}\right| \ll \Omega_s$$

The spatial variations of the magnetic field must also occur on scales larger than the Larmor radius

$$\rho_c \left|\frac{\nabla B}{B}\right| \ll 1$$

These limits, which are relevant for tokamak plasmas, will be assumed in the following. With such assumptions, a separation of scales appears and the motion of particles can be obtained as the *sum* of the (fast) gyromotion and the (slow) drift of the particle's *guiding-center* (i.e. the center of the Larmor radius).

The derivation of the guiding-center drifts will not be detailed here but can be found in many plasma physics textbooks, for instance [HM92]. However, it is important to note that, in the adiabatic limit and when the electromagnetic fields are constant in time, the particle motion is characterized by three independent motion invariants, namely

- the total energy $H_{eq} = mv^2/2 + e_s\phi$, where v is the total velocity and ϕ is the electric potential;
- the magnetic moment $\mu = m_s v_\perp^2/(2B)$ where B is evaluated at the guiding-center position
- the toroidal kinetic momentum $p_\varphi = -e\chi + mRv_\varphi$ where R is the major radius and v_φ is the toroidal velocity of the particle.

The total energy is an exact invariant, while the magnetic moment is often referred to as the *adiabatic invariant* as it is conserved only in the adiabatic limit. The toroidal kinetic momentum reflects the axisymmetry of the tokamak configuration.

2.2 Introduction to gyrokinetic theory

2.2.1 The gyrokinetic ordering

As outlined in section 1.3, describing plasma turbulence in tokamaks requires a kinetic description of collective dynamics, with a six dimensional equation for the distribution of particles. Although this model is already a statistical reduction of the complete many-body problem, it still involves a large diversity of scales, down to cyclotron waves and Langmuir waves. For the study of micro-turbulence in tokamak plasmas, the interest is on characteristic frequencies smaller than the cyclotron frequency, i.e. $\omega < \Omega_s$ where $\Omega_s = e_s B/m_s$ is the cyclotron frequency (see Fig. 1.3). By restricting the problem to such frequencies, the gyrokinetic model allows one to simulate plasma turbulence with a reasonable computational cost.

As presented in section 2.1.2, the equilibrium motion of particles in a tokamak magnetic configuration can be decomposed into a fast motion around the magnetic field, a parallel drift along the magnetic field line and slower drifts in the perpendicular plane. As the characteristic turbulent frequencies we are focusing on are slower than the cyclotron frequency of the particles considered, the 6D model can be reduced to a 5D model by averaging over the cyclotron motion, provided that certain orderings are respected. These orderings, deduced from experimental observations of tokamak micro-turbulence, form the basis of gyrokinetic theory. The gyrokinetic ordering for the microscopic fluctuations can be summarized as

$$\frac{\omega}{\Omega_s} \sim \frac{k_\parallel}{k_\perp} \sim \frac{e_s\phi}{T} \sim \frac{\delta n_s}{n_0} \sim \frac{\delta B}{B_0} \sim \frac{\rho_c}{L_n} \sim \mathcal{O}\left(\rho_{*s}\right) \tag{2.3}$$

The key dimensionless parameter is ρ_{*s}, which corresponds to the thermal Larmor radius normalized to the tokamak minor radius, i.e. $\rho_{*s} = m_s v_\perp/(e_s B a)$. In the case of tokamaks, for electrons $\rho_{*e} < 10^{-4}$ and for ions $\rho_{*i} < 10^{-2}$. Let us review these orderings in more detail:

- the characteristic frequency of micro-turbulence (ω) is much slower than the cyclotron frequency of the species (Ω_s),
- the parallel component of the wave vector ($k_\parallel = \mathbf{k}\cdot\mathbf{b}$ where $\mathbf{b} = \mathbf{B_0}/B_0$) is much smaller than the perpendicular component ($k_\perp = |\mathbf{k}\times\mathbf{b}|$). This reflects the fact that the rapid motion of particles along the magnetic field leads to large gradient lengths in the parallel direction,
- the *microscopic* potential energy ($e_s\phi$) is much smaller than the kinetic energy (or temperature T)[1],
- the density perturbations (δn_s) are much smaller than the equilibrium density (n_0),
- the perturbed magnetic field (δB) is much smaller than the equilibrium magnetic field (B_0),
- the Larmor radius (ρ_c) is much smaller than the characteristic length of the equilibrium density gradient ($L_n = |\nabla \ln n_0|^{-1}$).

Using this ordering, the gyrokinetic model was originally obtained by gyro-averaging the Vlasov equation with a recursive method [FC82]. This model served as the basis for the first kinetic simulations of plasma micro-turbulence [Lee83]. However, an important drawback of the recursive method is that it does not preserve the key mathematical properties of the Vlasov equation, namely its symmetry and conservation properties. The modern derivation of gyrokinetic theory [Hah88, BH07] is based on the Hamiltonian representation using Lie perturbation theory, which retains the symmetry and conservation properties of the coupled Vlasov and Maxwell equations. In particular, the conservation properties are essential to correctly describe the physics in nonlinear simulations and will be presented in section 3. The detailed derivation of the modern gyrokinetic model was reviewed in [BH07], and its key results will be presented in the following section in two asymptotic limits for the Maxwell equations. First of all, we consider the electrostatic limit, i.e. a constant magnetic field and $\mathbf{E} = -\nabla\phi$ where ϕ is the electrostatic potential. Furthermore, we also assume the low β approximation, where β is the ratio of kinetic energy to magnetic energy [2].

---

[1] For macroscopic fields with radial extents comparable to the gradient lengths, $e_s\phi/T \sim 1$ is possible.

[2] In tokamak plasmas, β is usually of the order of a few percents.

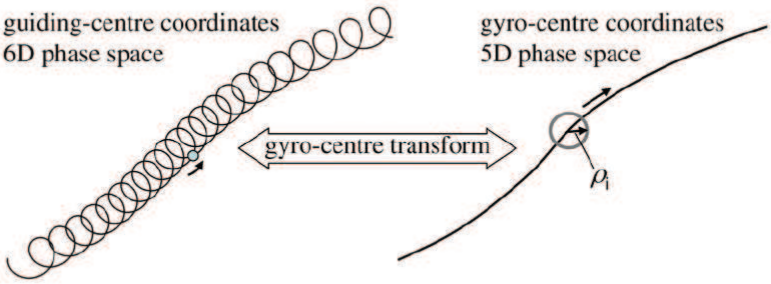

Figure 2.2: Reduction of phase-space from 6D to 5D in gyro-center coordinates by the gyro-center transform (figure from [GIVW10])

2.2.2 The gyrokinetic equation

The first step is a change of coordinates in 6D phase-space from the particle coordinates to the guiding-center coordinates. With the orderings in (2.3), the low frequency perturbations affect only the slow motion of the guiding center while the magnetic moment $\mu = m_s v_{G\perp}^2/2B$ becomes an adiabatic invariant (see section 2.1.2). To obtain the gyrokinetic equation, we use the coordinates of the guiding-center, $\mathbf{z} = (\mathbf{x}_G, v_{G\|}, \mu, \alpha)$ where $\mathbf{x}_G$ is the guiding-center position,$v_{G\|} = \mathbf{v}_G \cdot \mathbf{b}$ is the guiding-center parallel velocity and α is the gyro-angle, i.e. the angle describing $\mathbf{v}_{G\perp}$ in the plane perpendicular to the magnetic field. It is important to underline here that the guiding-center position $\mathbf{x_G}$ depends on the particle position *and* velocity. Therefore, there is no direct coordinate transformation between particle and guiding-center position, or between particle and guiding-center velocity, but rather a complete coordinate transformation in 6D phase-space, *mixing* position and velocity coordinates.

The Lie transformation provides the gyrokinetic equation at an arbitrary order in ρ_{*s} while keeping the Hamiltonian structure of the Vlasov equation. In practice, only the first order is kept in the perturbed Hamiltonian, which can be written as

$$H_s = \frac{1}{2} m_s {v_{G\|}}^2 + \mu B + e_s \phi + \mathcal{O}({\rho_*}_s^2) \tag{2.4}$$

At this stage, the Hamiltonian still depends on the six phase-space coordinates. The second step is to remove the dependence of the perturbed Hamiltonian H_s on the gyro-angle α by integrating over the cyclotron motion. After this so-called gyro-center transform, the gyro-angle α becomes an ignorable variable in the system while the magnetic moment μ becomes an *exact* invariant rather than an adiabatic invariant. The result of this transformation is represented schematically in Fig. 2.2. We stress here that gyro-averaging does not simply average out the cyclotron motion of the particle, and in particular the procedure retains the information on the variation of the fields at the scale of the Larmor radius. One can thus understand the gyro-center as a current ring of the size of the Larmor radius, rather than the classical picture of a pseudo-particle traveling at the center of the particle's orbit.

In principle, a distinction should be made between the coordinate system $\mathbf{z}$ previously used and the one resulting from the gyro-center transformation. In order to simplify notations, this distinction will not be made here. The Hamiltonian $\bar{H}_s$, which is now independent of the gyro-angle α, reads

$$\bar{H}_s = \frac{1}{2} m_s {v_{G\|}}^2 + \mu B + e_s J \cdot \phi \tag{2.5}$$

where the gyro-averaging operator J is defined as $J \cdot \phi \equiv \oint \phi \, \mathrm{d}\alpha/2\pi$.

The result is a reduced kinetic equation for the evolution of the (5D) gyro-center distribution function $\bar{F}_s(\mathbf{x}_G, v_{G\|}, \mu)$ which can be expressed in the Hamiltonian formalism as

$$\frac{\mathrm{d}\bar{F}_s}{\mathrm{d}t} \equiv \frac{\partial \bar{F}_s}{\partial t} + \left[\bar{F}_s, \bar{H}_s\right] = \mathcal{C}(\bar{F}_s) \tag{2.6}$$

where $[\cdot,\cdot]$ is the Poisson bracket in the gyro-center coordinate [BH07], which is defined for two given fields G and H as

$$\begin{aligned} [G,H] &= \frac{\Omega_s}{B}\left(\frac{\partial G}{\partial \alpha}\frac{\partial H}{\partial \mu} - \frac{\partial G}{\partial \mu}\frac{\partial H}{\partial \alpha}\right) \\ &\quad - \frac{1}{eB^*_{\|}}\mathbf{b}\cdot\{\nabla G \times \nabla H\} + \frac{1}{B^*_{\|}}\mathbf{B}^*\cdot\left\{\nabla G \partial_{mv_{G\|}} H - \partial_{mv_{G\|}} G \nabla H\right\} \end{aligned} \tag{2.7}$$

where where $\mathbf{b}$ is the unit vector in the direction in the direction of $\mathbf{B}$, $\mathbf{B}^* = \mathbf{B} + (mv_{G\|}/e)\nabla \times \mathbf{b}$ and $B^*_{\|} = \mathbf{b}\cdot\mathbf{B}^*$ is the volume element in guiding-center velocity space. Note that the first term in (2.7) contains derivatives with respect to the gyro-angle α which will be trivially vanishing as the gyro-angle dependence of all the quantities considered have been removed by the gyro-center transformation. The term $\mathcal{C}(\bar{F}_s)$ on the right-hand side of (2.6) is a gyro-averaged collision operator in guiding-center phase-space, which will be discussed in section 2.3.2.

In order to close the gyrokinetic system, the electric potential, which appears in the Hamiltonian, must be computed. This is the object of the following section.

2.2.3 The gyrokinetic quasi-neutrality equation

In the general electrostatic case, the electric potential can be obtained from the Poisson equation

$$\nabla^2 \phi = -\frac{1}{\epsilon_0} \sum_{species} n_s e_s \tag{2.8}$$

where ϵ_0 is the vacuum permittivity and n_s is the density of species s. This can be expressed using the electron Debye length $\lambda_{D,e} = (\epsilon_0 T_e / n_0 e^2)^{1/2}$, which leads to

$$\lambda^2_{D,e} \nabla^2 \left(\frac{e\phi}{T_e}\right) = -\frac{1}{n_0} \sum_{species} n_s e_s \tag{2.9}$$

In fusion plasmas, the electron Debye length is orders of magnitude smaller than the ion Larmor radius. Such sub-Larmor scales cannot be treated by the gyrokinetic model due to the approximations previously considered, and the term in $\lambda^2_{D,e}\nabla^2$ is therefore negligible in the Poisson equation. As a result, at the scales considered in the gyrokinetic model, the plasma can be considered *quasi-neutral*, which is consistent with the conventional interpretation of the Debye length as corresponding to the characteristic length at which individual charges are shielded. Thus, the left-hand side of Eq. (2.9) can be neglected and the Poisson equation is then replaced by a quasi-neutrality condition

$$\sum_{species} n_s e_s = 0 \tag{2.10}$$

where n_s is the density of species s. It is important to realize here that the densities appearing in Maxwell's equations are the densities of particles, rather than the densities of gyro-centers, which correspond to the first moment of the distribution functions evolved by the gyrokinetic Vlasov equation. Thus, the density of *particles* for each species n_s must be computed from the *gyro-center* distribution $\bar{F}_s$. The latter distribution is related to the particle distribution F_s by the following expression

$$F_s = \bar{F}_s + \frac{e_s}{B} \left\{ \phi - \bar{\phi} \right\} \partial_\mu \bar{F}_{s,eq} \tag{2.11}$$

where $\bar{F}_{s,eq}$ is the equilibrium distribution of gyro-centers and $\bar{\phi} = J \cdot \phi$ is the gyro-averaged electric potential. More generally, an overbar indicates a gyro-averaged quantity. This result arises from the canonical transformation relating the particle and gyro-center coordinates, a detailed proof can be found in [GS]. This leads to $n_s = n_{G,s} + n_{pol,s}$ where $n_{G,s}$ is an integral in gyro-center phase-space and the polarization density $n_{pol,s}$ is a function of the electric potential ϕ. The detailed calculations of these two terms is presented in appendix B and, in the large wavelength limit ($k_\perp \rho_c \ll 1$) for the polarization density, lead to

$$n_{G,s} = \int \mathcal{J}_v \mathrm{d}\mu \mathrm{d}v_{G\|} J \cdot \bar{F}_s \tag{2.12}$$

$$n_{pol,s} = \nabla \cdot \left\{ \frac{n_{eq,s} m_s}{e_s B^2} \nabla_\perp \phi \right\} \tag{2.13}$$

where $\mathcal{J}_v = 2\pi B_\|^* / m_s$ is the Jacobian in gyro-center velocity-space. We recall that J is the gyro-averaging operator. Injecting equations (2.12) and (2.13) in the quasi-neutrality equation (2.10) leads to an equation which can be solved to obtain the electric potential ϕ for a given distribution function $\bar{F}_s$:

$$\sum_{species} -\nabla \cdot \left\{ \frac{n_{eq,s} m_s}{B^2} \nabla_\perp \phi \right\} = \sum_{species} e_s \int 2\pi B_\|^* \mathrm{d}\mu \mathrm{d}v_{G\|} J \cdot \bar{F}_s \tag{2.14}$$

where J is the gyro-averaging operator, and $n_{eq,s}$ is the equilibrium density of species s. Note that, if we consider that the electron mass is negligible compared to the ion mass, only the polarization contribution of ions need to be accounted for on the left-hand side of the equation.

2.2.4 A reduced gyrokinetic model for electrostatic ion turbulence

The model described in the previous sections is well-suited for the description of electrostatic turbulence in tokamaks, which can be generated by a number of underlying mechanisms corresponding to electron or ion-driven instabilities (see [CW94] for a review). However, the numerical cost of simulating electron turbulence in global simulations is extremely demanding in terms of numerical resources, because the characteristic lengths and scales are many orders of magnitude smaller than the relevant time-scales for confinement studies, i.e. the tokamak size and the confinement time. In order to perform global simulations using dimensionless parameters relevant for ITER, including only ion turbulence, one already needs to apply state-of-the-art techniques in terms of High Performance Computing, using the maximum numerical resources available today. For an equivalent simulation including electron turbulence, the radial and poloidal resolution should be increased by one order of magnitude, and the characteristic time-step reduced approximately by the square root of the mass ratio. Roughly speaking, the cost of a simulation of electron rather than ion turbulence is three to four orders of magnitude greater.

Global nonlinear gyrokinetic simulations including electro turbulence have become accessible due to the rapid progress of numerical resources [GLB+11, BVS+11], but for larger values of ρ_*. In the present work, we focus only on ion micro-turbulence, which allows us to reach dimensionless parameters relevant for ITER. With this choice, the only source of energy for turbulence is from the ion temperature gradient, corresponding to the so-called *Ion Temperature Gradient* (ITG) instability [CRS67]. These modes are sometimes referred to as η_i modes, as the instability is characterized by the parameter $\eta_i = \mathrm{d}\log T_i / \mathrm{d}\log n_i$.

Quasi-neutrality equation

For the study of ion turbulence only, we can consider the asymptotic limit $m_e \to 0$, which is consistent with the ρ_{*i} approximation since $m_e/m_i < \rho_{*i}$. In this limit, at the time scales considered in the model, one can assume that the *parallel* electron motion is fast enough for the electrons to have reached a Boltzmann equilibrium, and they do not need to be treated kinetically. With this approximation, the fluid equation for parallel electron dynamics simply reads $en_e\nabla_\parallel\phi - \nabla_\parallel p_e = 0$ where $\nabla_\parallel$ is the gradient in the direction of the magnetic field line, i.e. $\nabla_\parallel = \mathbf{b}\cdot\nabla$. In the isothermal limit, this leads to $\nabla_\parallel n_e = (en_e/T_e)\nabla_\parallel\phi$. The solution of this equation is $n_e = n_0 \exp\left(e\phi/T_e\right)$ for $k_\parallel \neq 0$. Thus, the perturbed electron density in the quasi-neutrality equation reads

$$\delta n_e = -n_{eq}\frac{\delta\phi}{T_e} \tag{2.15}$$

where δn_e (respectively $\delta\phi$) is the non-zonal component of the electron density (respectively of the electric potential). This approximation of the electron dynamics is often referred to as *adiabatic electron response*.

Moreover, only one ion species is considered in the following. Therefore, only one species will be treated kinetically and the species subscript s will be left out wherever no ambiguity is possible. Assuming that an equilibrium solution is known, corresponding to a vanishing electric potential, the gyrokinetic quasi-neutrality equation (2.14) then reads

$$-\nabla\cdot\left\{\frac{n_{eq}m}{B^2}\nabla_\perp\phi\right\} + \frac{n_{eq}e}{T}\left(\phi - \langle\phi\rangle_{F.S.}\right) = e\int 2\pi B^*_\parallel \mathrm{d}\mu\mathrm{d}v_{G\parallel} J\cdot(\bar{F} - \bar{F}_{eq}) \tag{2.16}$$

where $\bar{F}_{eq}$ is the equilibrium gyrocenter distribution function, associated with a vanishing electric potential and $\langle\cdot\rangle_{F.S.}$ is the flux-surface averaged electric potential defined for a given field g as

$$\langle g\rangle_{F.S.} = \frac{\int g\,\mathcal{J}_s \mathrm{d}\theta\mathrm{d}\varphi}{\int \mathcal{J}_s\mathrm{d}\theta\mathrm{d}\varphi} \tag{2.17}$$

where $\mathcal{J}_s = 1/(\mathbf{B}\cdot\nabla\theta)$ is the jacobian in real space (see section 2.1.1). Interestingly, Eq. (2.16) takes the form of a Poisson equation where the vacuum permittivity ϵ_0 is replaced by $n_{eq}m/B^2$ (in the perpendicular direction only).

Gyrokinetic equation

From the expression of the gyrokinetic equation in its general Hamiltonian form Eq. (2.6), it is useful to expand the Poisson bracket and obtain the following equivalent expression

$$\partial_t\bar{F} + \frac{1}{B^*_\parallel}\nabla_{\mathbf{z}}\cdot\left(\dot{\mathbf{z}}B^*_\parallel\bar{F}\right) = \mathcal{C}(\bar{F}) \tag{2.18}$$

where $\mathbf{z} = (\chi, \theta, \varphi, v_{G\|}, \mu)$ and $\dot{\mathbf{z}} = d_t\mathbf{z}$. $B^*_{\|} = B + (mv_{G\|}/e)\mathbf{b} \cdot (\nabla \times \mathbf{b})$ is the jacobian of the gyrocenter transformation, where $\mathbf{b}$ is the unit vector in the direction of $\mathbf{B}$; m and e are the species mass and charge. Eq. (2.18) is valid at order one in the small parameter $\rho_* = \rho_i/a \ll 1$ where ρ_i is the ion thermal gyroradius and a is the minor radius of the plasma. The equations of motion are

$$\begin{aligned} B^*_{\|} d_t\mathbf{x}_G &= v_{G\|}\mathbf{B}^* + \frac{1}{e}\mathbf{b} \times \nabla\Lambda & (2.19) \\ B^*_{\|} m d_t v_{G\|} &= -\mathbf{B}^* \cdot \nabla\Lambda & (2.20) \end{aligned}$$

where $\mathbf{x}_G$ is the gyrocenter position. We define $\mathbf{B}^* = \mathbf{B} + (mv_{G\|}/e)\nabla \times \mathbf{b}$ and $\Lambda = e\bar{\phi} + \mu B$, where $\bar{\phi}$ is the gyro-averaged electric potential. As can be observed in Eq. (2.20), the parallel motion along the magnetic field is not a free-streaming motion, as electromagnetic perturbations and the gradient of the magnetic force lead to acceleration forces. In order to highlight the physics content, Eq. (2.19) can be recast as

$$\frac{B^*_{\|}}{B} d_t\mathbf{x}_G = v_{G\|}\frac{\mathbf{B}}{B} + \frac{m{v_{G\|}}^2}{eB^2}\mu_0\mathbf{j} + \mathbf{v}_D + \mathbf{v}_E \qquad (2.21)$$

where $\mathbf{j}$ is the plasma current and

$$\begin{aligned} \mathbf{v}_D &= \frac{m{v_{G\|}}^2 + \mu B}{e}\frac{\mathbf{B}}{B^2} \times \frac{\nabla B}{B} & (2.22) \\ \mathbf{v}_E &= \frac{\mathbf{B}}{B^2} \times \nabla\bar{\phi} & (2.23) \end{aligned}$$

The velocity $\mathbf{v}_D$, called the curvature drift velocity, corresponds to the drift of guiding-centers due to the inhomogeneity of the magnetic field. Note that, at a given position in guiding-center phase-space, this drift is constant in time and does not depend on the distribution or on the electric potential. The second drift velocity, $\mathbf{v}_E$, corresponding to the $E \times B$ drift, contains the nonlinear physics as the electric potential, via the quasi-neutrality equations, is derived from the gyro-center distribution function.

These expressions, obtained here by expanding the Poisson brackets, can be easily recovered (up to small terms proportional to the parallel current $j_{\|}$) from the gyroaverage of Newton's equation of motion in the adiabatic limit [GS]. The gyrokinetic equation (2.18), coupled with the quasi-neutrality equation (2.16) provide a self-consistent description of electrostatic ion micro-turbulence in tokamak plasmas.

2.3 GYSELA: a global gyrokinetic code

The GYSELA code has been developed to solve the gyrokinetic model presented in the previous section. In the following, we present the modeling choices which have been made. Section 2.3.1 presents the key physics aspects of the code, while sections 2.3.2 and 2.3.3 focus respectively on the collision operator and gyro-averaging operator implemented in GYSELA. The semi-Lagrangian numerical scheme adopted in the development of the code is briefly reviewed in section 2.3.4.

2.3.1 Physical assumptions

First of all, let us summarize the key approximations which have already been made to obtain the model:

a) The gyrokinetic ordering (2.3) forms the basis of the model,

b) Simplified magnetic geometry (see section 2.1.1): we consider circular concentric magnetic surfaces, with the magnetic field given by its analytical expression Eq. (2.1),

c) Low plasma β limit (i.e. the ratio of the kinetic energy to the magnetic energy is small): this leads to a simplified expression for the curvature drift (see Eq. (2.22)),

d) Electrostatic approximation: time variations of the magnetic field are ignored. From the Maxwell-Faraday equation, this leads to $\mathbf{E} = -\nabla\phi$ and to the expression of the $E \times B$ velocity given by Eq. (2.23),

e) Adiabatic electron response: at the frequencies considered ($\omega \ll \Omega_i$), the electrons follow a Boltzmann response to the perturbations in the direction of the magnetic field.

Global, full-f gyrokinetic simulations

Historically, a number of gyrokinetic codes have chosen to separate the distribution function into a time independent equilibrium part and a fluctuating perturbation. This is the so-called "δf method" [DK95], where $\bar{F}(t) = \bar{F}_{eq} + \delta\bar{F}(t)$, with $\bar{F}_{eq}$ constant in time and with the assumption that $\delta\bar{F} \ll \bar{F}_{eq}$. However, this assumption has serious implications in terms of physics, as it does not allow for any back-reaction of the small scales on the background equilibrium, which will remain close to its initial state. Therefore, so called full-f codes have been developed, which solve the full distribution function, with no scale separation between equilibrium and perturbations. Note that an equivalent possibility is to allow for a self-consistent time evolution of $\bar{F}_{eq}$ in a δf algorithm. Although this method is more demanding numerically, it may give access to additional physics, namely the relaxation of the equilibrium profiles due to small-scale turbulence. Thus the equilibrium is not fixed at its initial value and may evolve to a very different state. Removing the constraint of $\delta\bar{F} \ll \bar{F}_{eq}$ means that events such as bifurcations or relaxations can occur. In particular, this allows for a self-consistent modeling of the so-called *zonal and mean flows* [DIIH05] – large-scale axisymmetric and poloidally symmetric shear flows with low or zero frequency – which play an essential role in the regulation of turbulent transport [LHL+98] (see section 2.4).

Another important modeling choice to make for gyrokinetic codes is how to account for the toroidal geometry, and whether or not global geometric effects should be included. One possibility is to take advantage of the strong anisotropy of the physics, and in particular the much smaller wavelengths in the perpendicular direction ($k_\parallel \ll k_\perp$ in the gyrokinetic ordering (2.3)). In this context, using coordinates aligned with the magnetic field, one can perform simulations in spatial regions which remain close to a magnetic field line. This choice gives rise to so-called "flux-tube" codes [DJKR00, CW03a]. On the one hand, the reduction in numerical cost achieved by the flux-tube approach allows one, for identical numerical resources, to include additional physics in the model, for instance including electron dynamics. On the other hand, the main drawback of this type of modeling is the implicit scale separation between mean profiles and fluctuations. Flux-tube codes assume periodic fluctuations in the radial direction and constant-in-time mean gradients of the background profiles. To avoid this approximation, so-called "global" gyrokinetic codes have been developed, taking into account the geometry of the whole plasma – or at least a large radial domain in the tokamak. Obviously, this approach leads to more costly numerical simulations, and the issue of the radial boundary conditions must be addressed.

A number of global, full-f, gyrokinetic codes have been developed in recent years [GBB+06, KCA+06, JBA+07, WHL+07, HJKO08, IUAT09, GLB+11] (see [GIVW10] for a general review) without assuming any scale separation between equilibrium and fluctuations. The question of radial boundary conditions is critical and can impact the physics in these codes. For global codes, including GYSELA, three types of simulation can be distinguished.

Flux driven simulations

Most global gyrokinetic codes have been developed to simulate the core plasma, inside the last closed flux-surface – usually up to a normalized radius $\rho = r/a$ ranging from 0.8 to 0.9. Moreover, because of numerical difficulties, the region near the magnetic axis ($\rho = 0$) is rarely included in the simulation domain, which usually has a minimum normalized radius between 0.1 and 0.2. The choice of the inner and outer radial boundary conditions for temperature profiles is an important issue for plasma turbulence simulations, as identified previously in fluid simulations [GSB+99], and should also be addressed in detail for global gyrokinetic simulations[3].

The first gyrokinetic simulations were performed with so-called *thermal baths* boundary conditions. In such simulations, the ion temperature was fixed to its initial value at both radial boundaries of the simulation domain. Several serious limitations to this type of simulation have been identified. First of all, it was found [GSA+07] that strong gradients may appear near the boundaries of the simulation domain, due to the relaxation of the temperature profiles, as can be anticipated from a simple picture such as Fig. 2.3. More importantly, the drawback of such simulations is that, far from the radial boundaries of the simulation, the gradients in the system will systematically relax towards the state of marginal stability. Thus, it is not possible, using thermal baths as boundary conditions, to drive the system towards a different state, further from the non-linear stability threshold. This represents a serious limit as it is not evident that experimental plasmas are indeed systematically near this state of marginal stability.

Another type of gyrokinetic simulations is obtained by forcing the mean temperature gradient to remain near its initial profile. This type of simulation is referred to, for obvious reasons, as *gradient driven*. One of the motivations for this choice is that experimental profiles can then be enforced in global simulations, allowing one to perform comparisons between simulations and experiments, for example in [GLB+11]. These simulations imply the use of an *ad hoc* heat source to maintain the mean gradient. Several strategies are possible to perform this, but the most common solution is to use a Krook operator [MJT+09]. While gradient driven simulations allow for long times to be reached, with a statistical steady-state and adequate statistics, the obvious limitation is that the heat source must depend on the distribution function. Thus, the input power to the system will vary in time and will depend on the dynamics of the turbulence, while one would rather expect turbulence to adapt to the input power. The heat source acts to counter the effects of turbulence *locally* – both spatially and in time. In fact, one might describe this heating scheme as an infinity of independent, localized sources. Moreover, although gradient driven simulations do not necessarily imply a scale separation in the form of a

---

[3] Boundary conditions for toroidal rotation are also a critical open issue when studying momentum transport, and will be discussed in sections 4.1.1 and 5.3.

$\delta\bar{F} \ll \bar{F}_{eq}$, one expects the mean profiles to remain close to their initial values, as the heat source forces the distribution function in the direction of the initial (generally Maxwellian) distribution, preventing or at least hindering significant excursions from the initial state of the system. Thus, even though the global geometry effects may be taken into account, such simulations appear to have much in common with flux-tube simulations, as the mean gradient remains constant throughout the duration of the simulation.

The third possibility for gyrokinetic simulations, which is the one adopted in GYSELA, is to prescribe the heat source in the system. The turbulence then becomes *flux driven*, as the mean energy flux is imposed by the source. The importance of flux driven simulations has been demonstrated by fluid simulations [CNLD96, SG98], and the impact on the resulting turbulent transport of the choice between gradient driven and flux driven simulations is well documented in this context [GSB+99]. Heat sources have recently been implemented in several gyrokinetic codes [IUAT09, SGA+10, GLB+11], together with boundary conditions such as presented in Fig. 2.3. At the outer radial boundary, the temperature remains fixed at its initial value, acting as a heat sink for the system. On the other hand, the system is driven by a heat source localized near the inner boundary, and a vanishing temperature gradient is imposed at this boundary, corresponding to the symmetry condition which would be enforced at $\rho = 0$.

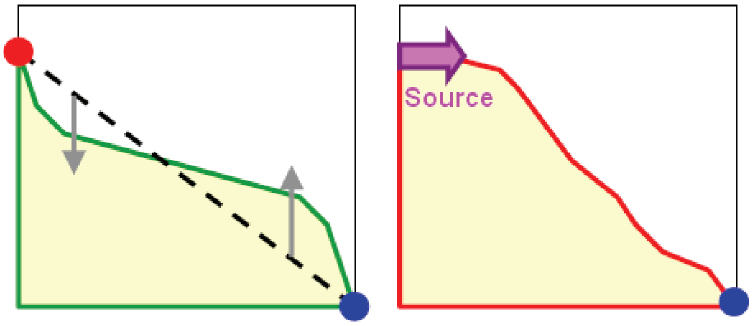

Figure 2.3: Sketch of the difference between simulations with fixed boundaries (left) or fixed flux (right)

Prescribing a heat source in a 5-dimensional gyrokinetic simulation, at a reasonable numerical cost, is a non-trivial problem. In GYSELA, a versatile source has been implemented by projecting the velocity-dependent part of the source on the orthogonal basis of Hermite and Laguerre polynomials. Thus the general form of the source is

$$S(r,\theta,\varphi,v_{G\parallel},\mu) = \sum_{l=0}^{+\infty}\sum_{h=0}^{+\infty} c_{hl}(r,\theta) H_h(\hat{v}_\parallel) L_l(\hat{\mu}) e^{-\hat{v}_\parallel^2-\hat{\mu}} \tag{2.24}$$

where H_h (respectively L_l) represent the Hermite (respectively Laguerre) polynomials. The normalized parallel velocity is $\hat{v}_\parallel = v_{G\parallel}/\sqrt{2T_s/m_s}$ and the normalized magnetic moment is $\hat{\mu} = \mu B/T_s$. With a careful choice of the coefficients c_{hl}, one can decide which fluid moments will be affected by this source [SGA+11]. For instance, if only the second moment of the source is non-vanishing, one can construct a heat source which does not inject any particle or parallel momentum. Likewise, another choice of coefficients can provide a source of momentum without additional heating.

Finally, when performing flux driven simulations, an *ad hoc* diffusion term is added to the gyrokinetic equation (2.18) near the radial boundaries of the simulation. It takes the form of a spatial diffusion, $\frac{1}{r}\partial_r\left\{D(r)\partial_r\bar{F}\right\}$ where $D(r)$ vanishes outside narrow radial regions localized near the edges of the simulation domain. Additionally, a similar diffusion term in the poloidal direction can be added. Near the inner edge, this term helps preventing the occurrence of negative values of the distribution function in the region of localization of the heat source[4]. More importantly, at the outer edge, this diffusion ensures the coupling of the plasma to the fixed temperature outside the domain. In this sense, radial diffusion acts as the heat sink in the system.

2.3.2 A model collision operator for Coulomb interactions

The right-hand side of the gyrokinetic equation (2.18) contains a collision operator $\mathcal{C}(\bar{F})$ for binary interactions. As we only consider one kinetic species in the present work, this operator should account for ion-ion Coulomb collisions. As explained in section 1.3, tokamak plasmas are weakly collisional, with mean free paths of the order of the km, and transport is dominated by turbulence. However, even in the presence of turbulence, collisional effects play an essential role in determining the mean flows on times longer than the characteristic turbulent times. Second, the issue of the interplay between turbulent and collisional (also known as "neoclassical") transport, has yet to be resolved [LHL+99, DPGS+09]. Moreover, it was shown that the damping of zonal flows is modified when taking into account collisions, as they are damped to a non-vanishing residual value in the absence of collisions [RH98]. As a final motivation, we recall that collisions may help limit the development of small-scale structures in velocity space, thus improving the accuracy of gyrokinetic codes.

A compact integral expression for grazing Coulomb collisions was originally derived by Landau [Lan36], in the approximation of weak, elastic collisions. For a single species plasma, the collision operator can be expressed as

$$\mathcal{C}(F) = w\,\frac{\partial}{\partial \mathbf{v}} \cdot \int \mathbf{U} \cdot \left(F(\mathbf{v}')\frac{\partial F}{\partial \mathbf{v}} - F(\mathbf{v})\frac{\partial F}{\partial \mathbf{v}'} \right) \mathrm{d}^3\mathbf{v}' \tag{2.25}$$

where $w = 2\pi e_s^4 \ln\Lambda/\epsilon_0^2 m_s^2$. The Coulomb logarithm is $\ln\Lambda = \ln(\lambda_D/\lambda_L)$ where λ_D is the Debye length, corresponding to the maximum distance of interaction between two particles because of Debye shielding, and λ_L is the minimal impact parameter between two ions, usually referred to as Landau length. In tokamak plasmas, $\ln\Lambda \simeq 17$. Note that although the exact value of Λ may not be known, since only its logarithm appears in the collision operator, an approximate value is acceptable as an error in the value of Λ would not significantly impact $\ln\Lambda$.

The tensor $\mathbf{U}$ depends on the relative velocity $\mathbf{u} = \mathbf{v} - \mathbf{v}'$, and reads

$$U_{ij} = \frac{u^2\delta_{ij} - u_i u_j}{u^3} \tag{2.26}$$

The fact that this tensor depends only on the relative velocity reflects the symmetry properties of binary Coulomb collisions. In terms of the collision operator, this should lead to a property of Galilean invariance through a momentum-conserving operator.

In the context of gyrokinetics, a linearized gyro-averaged version of this operator was derived [XR91], assuming that the distribution function remains close to a refer-

---

[4] Because the source is designed to inject a fixed quantity of energy in a localized phase-space domain, regardless of the distribution function, it may lead to important local modifications of the distribution (and possibly even to negative values) which can be smoothed out by radial diffusion and collisions.

ence Maxwellian. This type of operator, well-suited for δf codes, is challenging numerically for full distribution gyrokinetics. It was nevertheless successfully implemented recently [IUAT09]. In order to avoid such costly development and simulations, simplified collision operators have been derived for full-f codes. The objective is to find a simpler form for the collision operator, compatible with the numerical scheme and implying limited numerical costs, while verifying a number of basic properties:

- particle, momentum and energy conservation;
- relaxation toward a Maxwellian distribution function (Boltzmann's H theorem);
- correct description of the neoclassical equilibrium [HH76].

One such operator, which retains the conservation properties but has a simpler form than the complete operator [XR91] is the Lenard–Bernstein collision operator [LB58], which can be expressed in momentum variables $p_\parallel$ and $p_\perp$ as

$$\mathcal{C}(F) = \frac{1}{p_\perp}\partial_{p_\perp}\left\{p_\perp D_{p_\perp} F_M \partial_{p_\perp}\left(\frac{F}{F_M}\right)\right\} + \partial_{p_\parallel}\left\{D_{p\parallel} F_M \partial_{p_\parallel}\left(\frac{F}{F_M}\right)\right\} \tag{2.27}$$

where F_M is a reference Maxwellian distribution. $D_{p_\perp}$ and $D_{p_\parallel}$ are velocity diffusion coefficients. Assuming F_M to depend only on gyro-center variables, gyro-averaging expression (2.27) leads to [GDPN$^+$09]

$$\begin{aligned}\mathcal{C}(\bar{F}) =& \frac{1}{B_\parallel^*}\partial_\mu\left\{B_\parallel^* D_\perp \frac{F_M}{B^2}\partial_\mu\left(\frac{\bar{F}}{F_M}\right)\right\}\\ &+ \frac{1}{B_\parallel^*}\partial_{v_{G\parallel}}\left\{B_\parallel^* D_\parallel F_M \partial_{v_{G\parallel}}\left(\frac{\bar{F}}{F_M}\right)\right\}\\ &+ \frac{1}{B_\parallel^*}\nabla_\perp\cdot\left\{B_\parallel^* D_{cl} F_M \nabla_\perp\left(\frac{\bar{F}}{F_M}\right)\right\}\end{aligned} \tag{2.28}$$

where $D_\perp = D_{p_\perp} p_\perp^2/m^2$, $D_\parallel = D_{p_\parallel}/m^2$ and $D_{cl} = D_{p_\perp}/e^2 B_\parallel^{*2}$. Interestingly, the third term in (2.28) is a spatial diffusion term, of the form $\nabla_\perp^2$. Mathematically speaking, this term is a direct result of the gyro-averaging procedure. One can understand this as a consequence of the "mixing" of position and velocity coordinates by the guiding-center transformation. The immediate drawback – in terms of numerical simulations – is that the momentum and energy conservation of the collision operator, which is local in position for the *particle* collision operator, is no longer verified at a given position in guiding-center space, but rather appears as a nonlocal effect. In other words, it takes the form of a compensation between the position and velocity terms of Eq. (2.28) in guiding-center phase space. In GYSELA, this small spatial diffusion term D_{cl} has not been implemented at the moment and a local (in space) momentum and energy conservation property for the collision operator is therefore possible.

Because the magnetic moment μ is an exact invariant of the collisionless gyrokinetic model, it serves as a parameter in the numerical model, and gyrokinetic codes such as GYSELA are parallelized in the μ direction. As a result, the numerical cost of collisions in perpendicular velocity space would be substantial, as large amounts of communication between processors, each representing a single μ value, would be required to compute the collision operator. It has been demonstrated analytically that collisions in parallel velocity space only are sufficient to recover the basic properties expected of the collision operator [GDPN$^+$09], including the predictions of neoclassical theory. This corresponds to the present status in GYSELA, i.e. $D_\perp = 0$ and $D_{cl} = 0$, leading to the following expression for the collision operator

$$\mathcal{C}(\bar{F}) = \frac{1}{B_\parallel^*}\partial_{v_{G\parallel}}\left\{B_\parallel^* D_\parallel F_M \partial_{v_{G\parallel}}\left(\frac{\bar{F}}{F_M}\right)\right\} \tag{2.29}$$

The Maxwellian F_M is chosen to be a local Maxwellian, characterized by a density n, a mean velocity $V_{\parallel coll}$ in the parallel direction and a temperature T_{coll} identical in the parallel and perpendicular directions. The following Maxwellian distribution is a solution of $\mathcal{C}(F_M) = 0$:

$$F_M = n\left(\frac{m}{2\pi T_{coll}}\right)^{3/2} \exp\left\{-\frac{m\left(v_{G\parallel} - V_{\parallel coll}\right)^2}{T_{coll}} - \frac{\mu B}{T_{coll}}\right\} \tag{2.30}$$

where T_{coll} and $V_{\parallel coll}$ need to be determined according to the required conservation properties of the operator. The collision operator (2.29) trivially conserves the number of particles. In addition, the conservation of parallel momentum and energy read

$$\int \frac{B_\parallel^*}{m}\mathrm{d}\mu\mathrm{d}v_{G\parallel}\, m v_{G\parallel}\mathcal{C}(\bar{F}) = 0 \tag{2.31}$$

$$\int \frac{B_\parallel^*}{m}\mathrm{d}\mu\mathrm{d}v_{G\parallel}\left(\frac{1}{2}m{v_{G\parallel}}^2 + \mu B\right)\mathcal{C}(\bar{F}) = 0 \tag{2.32}$$

These two constraints provide two linear equations in T_{coll} and $V_{\parallel coll}$, and are therefore verified if the temperature and velocity of the reference Maxwellian are defined as

$$\begin{aligned} mPV_{\parallel coll} &= \left\langle \frac{m}{B_\parallel^*}\partial_{v_{G\parallel}}(B_\parallel^* D_\parallel v_{G\parallel})\right\rangle \left\langle m D_\parallel v_{G\parallel}\right\rangle \\ &\quad - \left\langle m^2 D_\parallel {v_{G\parallel}}^2\right\rangle \left\langle \frac{1}{B_\parallel^*}\partial_{v_{G\parallel}}(B_\parallel^* D_\parallel)\right\rangle \qquad (2.33) \\ PT_{coll} &= \left\langle D_\parallel\right\rangle \left\langle m^2 D_\parallel {v_{G\parallel}}^2\right\rangle - \left\langle m D_\parallel v_{G\parallel}\right\rangle^2 \qquad (2.34) \end{aligned}$$

where

$$P = \left\langle D_\parallel\right\rangle \left\langle \frac{m}{B_\parallel^*}\partial_{v_{G\parallel}}(B_\parallel^* D_\parallel v_{G\parallel})\right\rangle - \left\langle D_\parallel v_{G\parallel}\right\rangle \left\langle \frac{m}{B_\parallel^*}\partial_{v_{G\parallel}}(B_\parallel^* D_\parallel)\right\rangle \tag{2.35}$$

Details of the calculation are presented in appendix C, including the more general case $D_\perp \neq 0$. The velocity-space average is defined as

$$\langle ... \rangle = \int \frac{B_\parallel^*}{m}\mathrm{d}\mu\mathrm{d}v_{G\parallel} F ... \tag{2.36}$$

For full-f simulations such as those performed with the GYSELA code, the temperature and velocity of the reference Maxwellian may evolve significantly and must therefore be updated regularly throughout the simulation.

As computed in [GDPN$^+$09], the velocity diffusion coefficient in (2.29) is

$$D_\parallel(r, v_{G\parallel}) = 3\frac{\sqrt{\pi}}{2}\frac{v_T^3 (r/R)^{3/2}}{qR_0}\nu^* \frac{\Phi(v) - G(v)}{2v} \tag{2.37}$$

where the collisionality parameter ν^* is a function of the ion-ion collision frequency ν_{ii}

$$\nu^* = \frac{qR_0\nu_{ii}}{v_T(r/R)^{3/2}} \tag{2.38}$$

$$\nu_{ii} = \frac{4\sqrt{\pi}}{3}\frac{ne^4\ln\Lambda}{(4\pi\epsilon_0)^2m^2v_T^3} \tag{2.39}$$

Eq. (2.37) makes use of the error function Φ and Chandrasekhar function G

$$\Phi(v) = \frac{2}{\sqrt{\pi}}\int_0^v e^{-x^2}\mathrm{d}x \tag{2.40}$$

$$G(v) = \frac{\Phi(v) - v\Phi'(v)}{2v^2} \tag{2.41}$$

The simplified operator (2.29), taking into account collisions in parallel velocity space only, was extensively studied in [DPDG+11]. The key results of neoclassical theory, in particular concerning heat transport and poloidal rotation, are well reproduced using this operator, including their aspect ratio and collisionality dependence.

2.3.3 Padé approximation of the gyro-average operator

In order to compute the gyro-center trajectories in the gyrokinetic equation (2.18), the electric potential must be gyro-averaged to obtain $\bar{\phi} = J\cdot\phi$. The gyro-averaging operator J is also applied to the gyro-center distribution function $\bar{F}_s$ in the quasi-neutrality equation (2.16). This operator corresponds to an average around a Larmor circle, which lies in the plane perpendicular to the magnetic field with a radius defined by the magnetic moment μ. The general expression of the gyro-average of a given field G is

$$\begin{aligned} J\cdot G &= \oint_0^{2\pi}\frac{\mathrm{d}\alpha}{2\pi}G \\ &= \left\{\oint_0^{2\pi}\frac{\mathrm{d}\alpha}{2\pi}\exp\left(\boldsymbol{\rho}_c\cdot\nabla\right)\right\}G \end{aligned} \tag{2.42}$$

where $\boldsymbol{\rho}_c$ is the Larmor radius. Note that, even if G depends only on the spatial coordinate, $J\cdot G$ will depend on the spatial coordinate and the magnetic moment μ. Eq. (2.42) can be explicited using a Fourier decomposition of G into its components $\hat{G}_{\mathbf{k}}$

$$\begin{aligned} J\cdot G &= \int_0^{2\pi}\frac{\mathrm{d}\alpha}{2\pi}\int_{-\infty}^{+\infty}\frac{\mathrm{d}^3\mathbf{k}}{(2\pi)^2}\hat{G}_{\mathbf{k}}\exp\left\{i\mathbf{k}\cdot(\mathbf{x}+\boldsymbol{\rho}_c)\right\} \\ &= \int_{-\infty}^{+\infty}\frac{\mathrm{d}^3\mathbf{k}}{(2\pi)^2}\left[\int_0^{2\pi}\frac{\mathrm{d}\alpha}{2\pi}e^{i\mathbf{k}\cdot\boldsymbol{\rho}_c}\right]\hat{G}_{\mathbf{k}}e^{i\mathbf{k}\cdot\mathbf{x}} \\ &= \int_{-\infty}^{+\infty}\frac{\mathrm{d}^3\mathbf{k}}{(2\pi)^2}J_0(k_\perp\rho_c)\hat{G}_{\mathbf{k}}e^{i\mathbf{k}\cdot\mathbf{x}} \end{aligned} \tag{2.43}$$

where J_0 is the Bessel function of first order, and $k_\perp$ is the norm of the perpendicular component $k_\perp = \mathbf{k} - (\mathbf{k}\cdot\mathbf{b})\mathbf{b}$ of the wave vector. This expression in Fourier space is practical when dealing with periodic geometry, and when the radial dependence of the Larmor radius is not accounted for. Thus, the exact expression (2.43) is mainly well-suited for the local gyrokinetic codes mentioned in section 2.3.1.

In the context of global gyrokinetic codes, Fourier decomposition is not practical, and other solutions must be sought. A method which has been adopted in several gyrokinetic codes, including GYSELA, is to use an approximation of the Bessel function which has a tractable expression in real space. The most common approximation is the Padé expansion [SGF+05] of the Bessel function

$$J_0(k_\perp \rho_c) \simeq \frac{1}{1+(k_\perp \rho_c)^2/4} \tag{2.44}$$

This approximation allows one to recover the limit of the Bessel function for large wavelengths, i.e., $k_\perp \rho_c \ll 1$, but overdamps smaller scales, as can be seen for the example in Fig. 2.4. In real space, the Padé approximation corresponds to an implicit equation where a Laplacian must be inverted

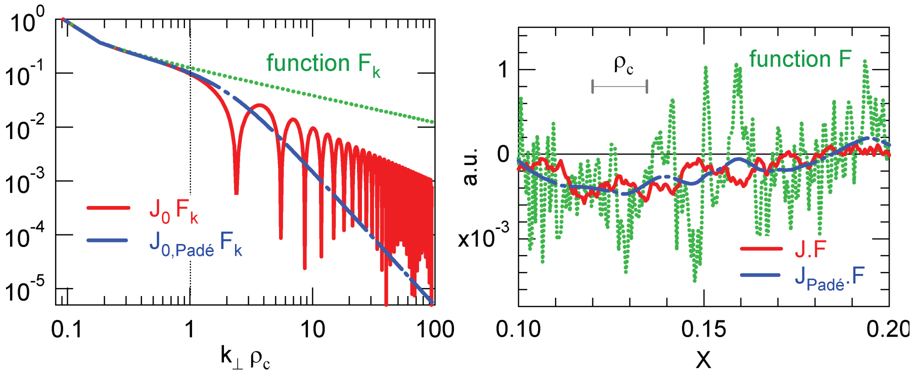

(a) (b)

Figure 2.4: Exact and Padé approximated gyro-average operators applied on an arbitrary funcion F exhibiting a broad Fourier spectrum ranging from low to large wavelengths as compared with the Larmor radius ρ_c: (a) Representation in Fourier space, (b) Representation in real space (figures from [SGF+05]).

$$\left(1-\frac{\rho_c^2}{4}\nabla_\perp^2\right) J\cdot G = G \tag{2.45}$$

where we recall the general expression of the Larmor radius $\rho_c^2 = 2m\mu/\left[e^2 B(r,\theta)\right]$. This expression does not verify the Hermitian property of the gyro-average operator, which is of importance for the symmetry and conservation properties of the gyrokinetic model (see section 3). Therefore, in GYSELA, the gyroaverage of a function G is actually obtained by solving

$$\left[1-\nabla_\perp\left(\frac{m\mu}{2e^2B_0}\nabla_\perp\right)\right] J\cdot G = G \tag{2.46}$$

where B_0 is constant. This additional approximation is consistent with the gyrokinetic ordering and recovers the Hermitian property of the exact gyro-average operator.

Since the Padé approximation is known to overdamp small scales, other approaches have been considered for the gyro-average operator in global simulations [CMS10]. One possibility is to approximate the integral over the Larmor circle by a sum over a finite number of points on this circle. By increasing the number of points, a good accuracy can be obtained even for large Larmor radii, which is not the case with the Padé approximation. Another promising alternative lies in direct integration of the gyro-average operator [CMS10].

2.3.4 The semi-Lagrangian numerical method

The gyrokinetic model considered in the present work, obtained by coupling a gyrokinetic equation (2.18) with a quasi-neutrality equation (2.16), belongs to the class of models generically referred to as Vlasov–Poisson models. Historically, three general types of numerical schemes have been developed to solve this class of problems. A detailed review of the numerical methods used to solve the gyrokinetic model can be found in [GS].

On the one hand, *Lagrangian* – also known as Particle-in-Cell (PIC) – methods [BL85] use a discrete description of velocity space as a finite number of macro-particles. These macro-particles then follow the characteristics of the Vlasov equation, using the fundamental property that the distribution function is exactly conserved along these characteristics. The only grid used is in real space, where the macro-particle distribution is deposited in order to solve the quasi-neutrality equation. The numerical cost of Lagrangian method depends on the number of macro-particles, which can be chosen depending on the expected accuracy. Moreover, parallelization of such algorithms is fairly straightforward and can be efficient for a very large number of processors. The main drawback of Lagrangian methods is that the sampling of the distribution function can lead to large numerical noise, which needs to be treated by efficient – but complex and computationally heavy – noise reduction method [JBA$^+$07].

On the other hand, *Eulerian* methods use a fixed grid in all directions of phase-space. The operators in the Vlasov equation can then be discretized using finite volumes, finite differences or spectral methods. The numerical scheme may be more expensive computationally than in the Lagrangian approach, but the essential advantage is that this method is not subject to noise issues. However, the discretization of the operators can lead to numerical dissipation.

The *semi-Lagrangian* method, which is the one chosen for GYSELA, is a compromise between the two classical Eulerian and Lagrangian methods. This approach was first developed for meteorological studies (see [SC91] for a review) before being adapted to plasma simulations [SRBG99]. The (Eulerian) fixed grid is adopted in order to avoid numerical noise due to sampling of the distribution function. In the spirit of Lagrangian simulations, the characteristics of the Vlasov equation are used for the time evolution of the distribution function, using its conservation along the characteristics. Thus, numerical dissipation due to the discretized operators is avoided.

The basic algorithm for the backward semi-Lagrangian numerical scheme implemented in GYSELA [GBB$^+$06, GS] is described in Fig. 2.5. At a given time iteration, for each grid point, the characteristic of the Vlasov equation is integrated backward in time. The foot of the characteristic which is then obtained is not, in general, on the simulation grid. Therefore, an interpolation must be performed to compute the value of the distribution function for that characteristic. A good accuracy during this interpolation step is essential to the overall results of the semi-Lagrangian scheme. It has been shown [FSB01, BM08] that cubic spline interpolation provides a good compromise between accuracy (i.e., low diffusivity) and numerical cost.

In the case of a complex geometry rather than circular magnetic surfaces, a new approach to the semi-Lagrangian method has been investigated, using Non Rational Uniform B-Splines (NURBS)[5]. This approach was implemented and validated in a two dimensional (1D in space, 1D in velocity) Vlasov–Poisson simulation [ALG$^+$11], but at the moment is not sufficiently mature to be adapted to the five dimensional model considered here.

---

[5] NURBS are a mathematical tool commonly used in the computer-aided design (CAD) community, which can describe complex geometries with a relatively low numerical cost.

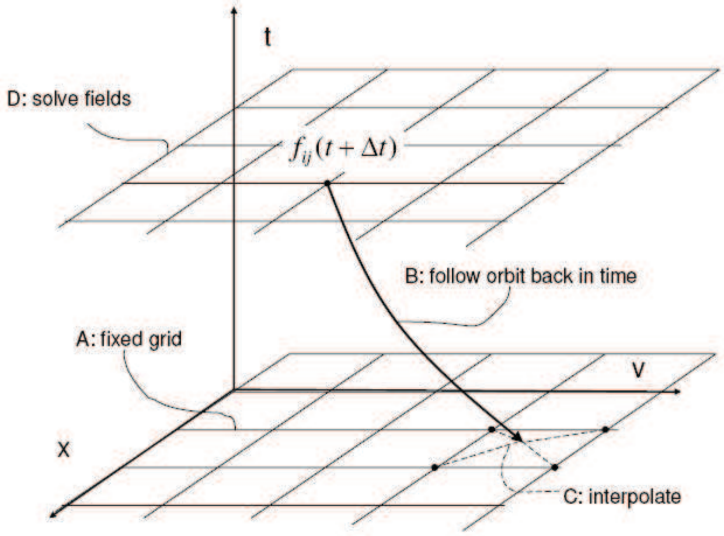

Figure 2.5: Interpolation scheme for the semi-Lagrangian method: (a) on a fixed phase-space grid, (b) follow trajectories back in time to compute $F_{ij}(t+\Delta t)$, (c) interpolate the value from the known values of $F(t)$, (d) solve the field equations. (figure from [GIVW10])

2.4 General presentation of a GYSELA simulation

As a complement to the presentation of the gyrokinetic model and its implementation in GYSELA, we describe in this section general results from a GYSELA simulation, setting the framework for the numerical results presented in later sections.

We consider a reference simulation where the normalized gyroradius is $\rho_* = 1/512$ at mid-radius, roughly corresponding to the expected value for ITER. The dimensionless collisionality, as defined in Eq.(2.38), approximately constant throughout the simulation domain, is $\nu^* = 0.1$. The 5D phase-space grid necessary for this simulation was $(N_r, N_\theta, N_\varphi, N_{v_{G\parallel}}, N_\mu) = (1024, 1024, 128, 128, 16)$, leading to approximately 3.10^{11} grid points. This simulation ran for one month on 8192 processors[6] on the *Jade* supercomputer of the Centre Informatique National de l'Enseignement Supérieur (CINES) in Montpellier, France.

The safety factor (see Eq. (2.2)) profile is chosen as $q(r) = 1 + 2.78\,(r/a)^{2.8}$ while the aspect ratio is $R/a = 3.2$. The temperature and density profiles are initialized with constant logarithmic gradients, except at the radial boundaries of the domain where the gradients are vanishing. The initial parameters are $-d_r \log n = R_0/L_n = 2$ and $-d_r \log T = R_0/L_T = 12$ where L_n and L_T are respectively the ion density and temperature gradient lengths, and R_0 is the major radius at the magnetic axis. These profiles place the plasma significantly above the linear threshold for the ITG instability. Since the adiabatic electron response impedes particle transport, the particle density profile remains constant throughout the simulation[7]. A heat source is prescribed in the plasma core, in order to operate in the flux driven regime. Note that the heat source used in the simulation does not inject any momentum or vorticity, as presented in section 2.3.1. Thus, the ion temperature is fixed only at the outer radial boundary, and evolves freely elsewhere.

---

[6] This corresponds to approximately 6.10^6 total hours, in other words nearly seven centuries of computation time!

[7] Variations of the *gyro-center* density are possible due to polarization but remain small.

In the statistical steady-state reached by the simulation, a mean ion temperature profile is obtained with $R_0/L_T \simeq 11.5$ The mean density and temperature profiles obtained are shown in Fig. 2.6.

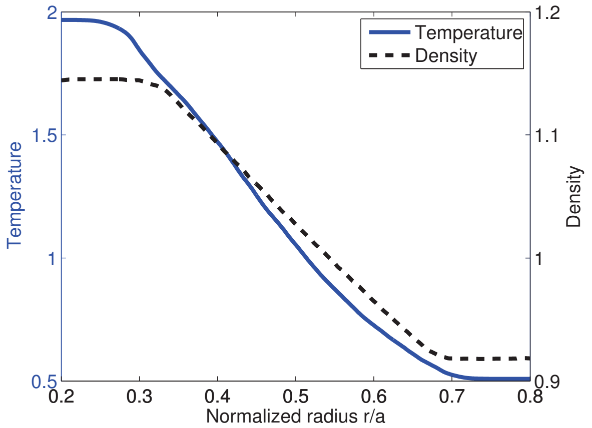

Figure 2.6: Initial density and temperature profiles for a GYSELA simulation.

In the initial distribution function, a small perturbation is present, covering a wide spectrum of poloidal and toroidal Fourier modes. From this initial state, stable modes will be rapidly damped while unstable modes will grow exponentially. The unstable modes then saturate and transfer energy to the zonal flows, eventually leading to a statistical steady-state resulting mainly from the competition between unstable modes and zonal flows (see the review [DIIH05] and references therein). Schematically, the unstable modes drive zonal flows by transferring energy through nonlinear interactions, more specifically three-wave coupling between two micro-scale modes and the zonal flow. Zonal flows can only be driven by such interactions and cannot directly grow from the free energy source (i.e., the temperature gradient). Thus the generation of zonal flows necessarily leads to a reduction of turbulence and transport. One can picture this as a predator-prey system, where the predator (zonal flows) feeds on the prey (unstable turbulent modes) but needs the prey to thrive in order to develop.

The condition of resonance for ITG modes leads to a vanishing wavenumber in the parallel direction, i.e. $k_\parallel = (n + m/q)/R = 0$. Thus, the unstable modes correspond to $m/n = -q$. This is apparent when computing the 2D Fast Fourier Transform (FFT) of the electric potential – which governs turbulent transport in *electrostatic* simulations – in the poloidal and toroidal directions, as represented in Fig. 2.7. The dominant modes are all localized near the $n = -m/q$ line.[8]

In real space, the electric potential is characterized by vortex-like structures. As these vortices are stretched in the direction of the magnetic field line, they can best be visualized by taking a poloidal cross-section of the electric potential fluctuations, as presented in Fig. 2.8 for the same time in the simulation as the previous representation in Fourier space (Fig. 2.7). The radial dimension of the structures in Fig. 2.8 is of the order of 10 Larmor radii, as will be discussed in chapter 5.

Because the fundamental goal of turbulence studies in tokamaks is to predict the

---

[8] We note that, although non-resonant modes have a very small amplitude (as can be observed in Fig. 2.7), they may play an important role through non-linear coupling with resonant modes and zonal flows. The important role of non-resonant modes was clearly identified in [SSDP+10]

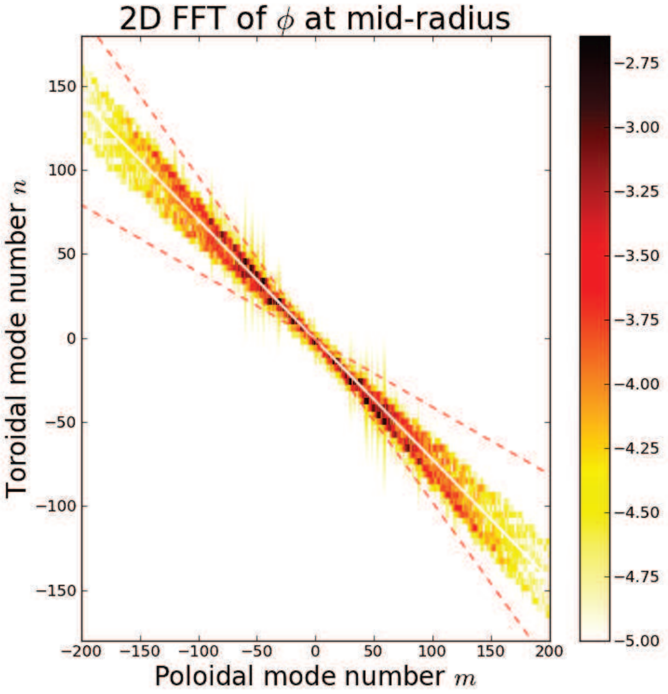

Figure 2.7: Two-dimensional Fast Fourier Transform (FFT) of the electric potential at mid-radius. The colors represent the logarithm of the amplitude for each (m, n) mode. The white line corresponds to the local resonance $m/n = -q$, while the dashed red lines correspond to the resonance computed from the minimum and maximum values of q in the simulation domain.

confinement time (see section 1.1), an important quantity to consider is the radial heat flux. We analyze here the dynamics of the flux-surface averaged turbulent heat flux, i.e.

$$Q_{turb} = \left\langle \int d^3v\, v_{Er} \left(\frac{1}{2} m {v_{G\parallel}}^2 + \mu B \right) \bar{F} \right\rangle_{F.S.} \tag{2.47}$$

where v_{Er} is the radial component of the $E \times B$ velocity (Eq. (2.23)) and $\langle\, . \,\rangle_{F.S.}$ is the flux-surface average defined in Eq. (2.17). Fig. 2.9 shows the radial and time evolution of Q_{turb}, normalized to gyro-Bohm units (see section 5.2). Several phases can be identified in this figure. At first, as the system is initialized without turbulence, no transport is observed. At approximately $\omega_c t = 3.10^4$, a large outward propagating front is observed, which corresponds to the linear regime of the instability. Finally, turbulent transport reaches a regime of statistical steady-state. This regime is dominated by large-scale avalanche-like events, with fronts propagating both inward and outward (although the heat flux remains outward), recovering the basic properties of self-organized criticality (SOC) models [SGA+10]. The detailed dynamics of this transport dominated by avalanches will be analyzed in depth in chapter 4.

Finally, to illustrate the kinetic aspects of the simulation, an example of the time evolution of the guiding-center distribution function is given in Fig. 2.10a, as a function of the parallel velocity for fixed values of all the other coordinates. Structures appear in velocity space, suggesting non-Maxwellian features of the distribution function. This is

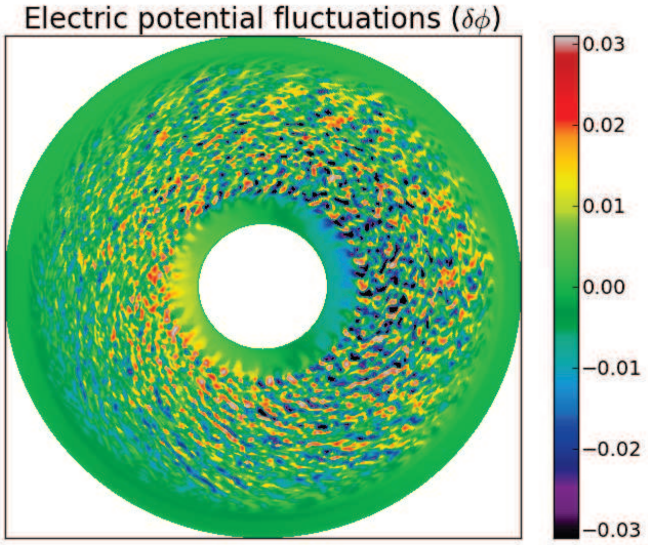

Figure 2.8: Poloidal cross-section of the electric potential perturbations

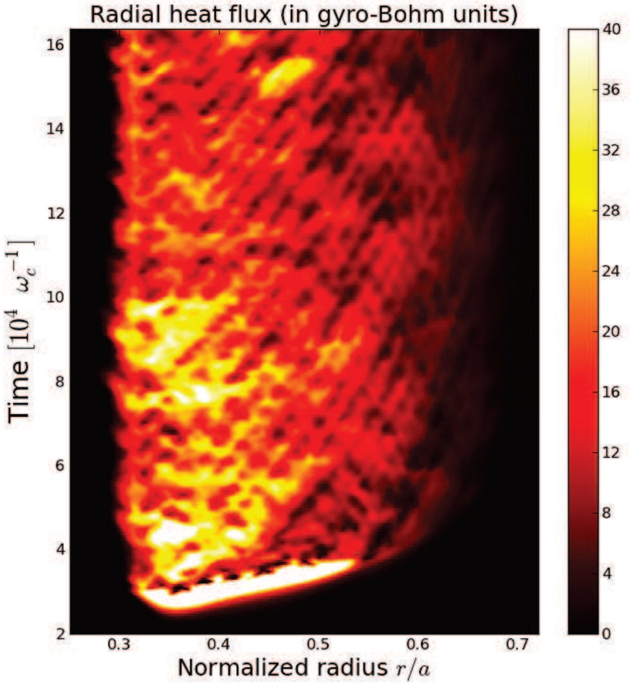

Figure 2.9: Two-dimensional (in radius and time) representation of the – flux-surface averaged – turbulent heat flux.

confirmed in Fig. 2.10b, where examples of clearly non-Maxwellian distribution functions in the simulation are given. It is interesting to note that non-Maxwellian features are not only identified in the tails of the distribution, where the number of particles is small, but

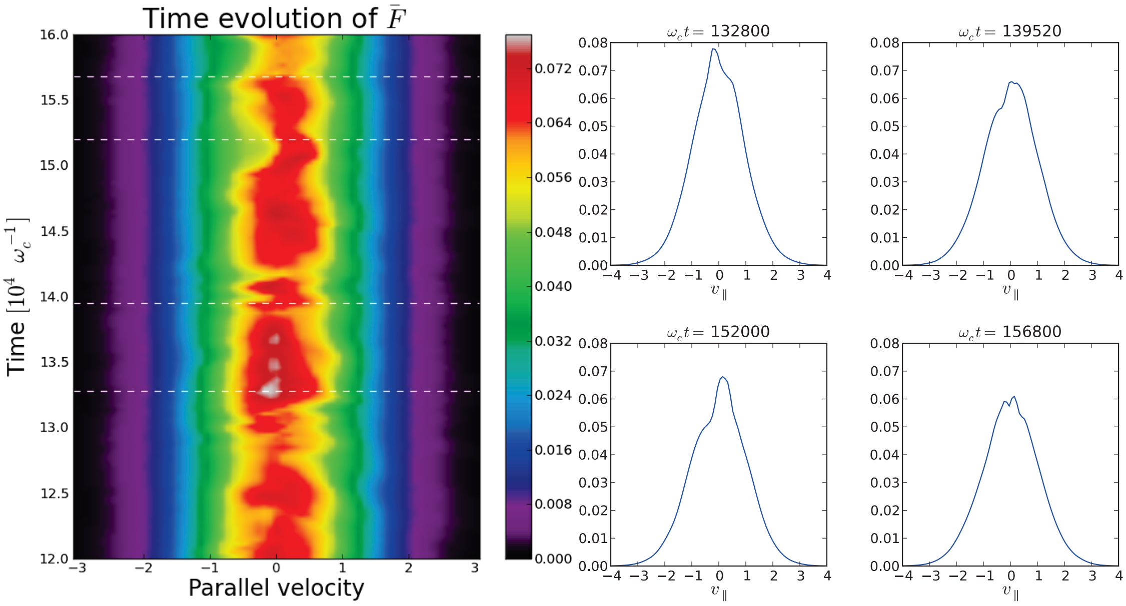

(a) (b)

Figure 2.10: (a) Time evolution of the guiding-center distribution function ($\bar{F}$) as a function of parallel velocity, for $r/a = 0.5$, $\mu = 0$ and $\theta = \varphi = 0$ and (b) Four examples of $\bar{F}(v_{G\parallel})$ for various times, corresponding to the dashed white lines in (a).

rather in the bulk of thermal particles, at velocities smaller than – or of the order of – the thermal velocity. The contribution of these structures to fluid moments is likely to be significant. The appearance of such structures in phase-space, possible because the characteristic collision time is much longer than the turbulent time scale, can explain why fluid simulations – which assume thermodynamic equilibrium – do not correctly reproduce the transport due to electrostatic turbulence in tokamak plasmas.

Chapter 3

Conservation equations and calculation of mean flows in gyrokinetics

> I presented the main theorems of Frl. Noether at the July 26 meeting (...) The main theorem given in section 2 above is a special case of the following far-reaching theorem of Frl. Noether: *If an integral I is invariant under a continuous group G_ρ with ρ parameters, then ρ linearly independent combinations of the Lagrangian expressions are divergences.*
>
> Felix Klein, 1918

The issue of the conservation properties of the gyrokinetic model, especially with respect to toroidal momentum, has emerged as a controversial subject in recent years. As a result, the suitability of gyrokinetic codes for the description of toroidal momentum transport has been questioned [PC08, PC10]. Indeed, verifying adequate conservation laws is an essential step to provide a correct description of mean flows. Using Noether's theorem [Noe18], Brizard [Bri10] derived a conservation equation in the context of a reduced gyrofluid model based on orderings consistent with gyrokinetic theory. The same method was also applied to the gyrokinetic variational principle [BT11]. Through a different approach, using the tools of gyrokinetic field theory, Scott and Smirnov [SS10] derived local conservation equations for energy and toroidal momentum.

In the following section 3.1, we derive local conservation equations for density, energy and toroidal momentum from the gyrokinetic model described in section 2.2.4, which corresponds to the equations implemented in full-f gyrokinetic codes [GIVW10]. These equations are *exact* insofar as they are obtained directly from the gyrokinetic model and require no further assumption or approximation. The local conservation of toroidal angular momentum is verified numerically in section 3.2, along with the radial force balance equation, confirming that gyrokinetic codes provide a self-consistent description of mean flows and radial electric field, that holds within the gyrokinetic framework and that can be computed with the precision of the code [AGG+11].

3.1 Local conservation laws for gyrokinetics

From the conservative form of the gyrokinetic equation (2.18), local conservation equations can be derived analytically. In the following, we consider the general case where several species are treated kinetically, but the subscript s will be left out for simplicity where there are no ambiguities. Details of the collision operator used in the model are not essential, as long as number of particles, momentum and energy are conserved, which is indeed the case for the reduced operator implemented in Gysela (see section 2.3.2).

3.1.1 Charge density

To obtain local conservation equations, we perform integrations of the conservative form of the gyrokinetic equation (2.18) over all variables other than the radial coordinate χ, i.e. over $\mathrm{d}\tau^* \equiv \mathcal{J}_s \mathrm{d}\theta \mathrm{d}\varphi \mathcal{J}_v \mathrm{d}v_{G\|} \mathrm{d}\mu$. We recall that $\mathcal{J}_s = 1/(\mathbf{B}\cdot\nabla\theta)$ is the Jacobian in real space and $\mathcal{J}_v = 2\pi B_{\|}^*/m_s$ is the Jacobian in gyro-center velocity-space.

We integrate Eq. (2.18) in a small phase-space volume between two surfaces χ and $\chi + \delta\chi$ and apply a divergence theorem. Summing over all species, this leads directly to the usual expression for local transport of charge density

$$\partial_t \bar{\rho} + \partial_\chi \mathcal{J}^\chi = 0 \tag{3.1}$$

where $\bar{\rho}$ is the charge density and $\mathcal{J}^\chi$ is the radial current of gyrocenters:

$$\bar{\rho} = \sum_{species} e_s \int \mathrm{d}\tau^* \bar{F} \tag{3.2}$$

$$\mathcal{J}^\chi = \sum_{species} e_s \int \mathrm{d}\tau^* (\dot{\mathbf{z}}\cdot\nabla\chi)\bar{F} \tag{3.3}$$

In the case of electrostatic simulations with adiabatic electron response (see section 2.2.4), boundary conditions impose a vanishing radial current at the edges of the simulation domain. Therefore the radial current $\mathcal{J}^\chi$ is expected to be small in such simulations.

3.1.2 Energy

Similarly, a conservation equation for the total energy can be derived by multiplying the gyrokinetic equation (2.18) by the gyrocenter Hamiltonian (2.5), which reads

$$\bar{H} = \frac{1}{2} m {v_{G\|}}^2 + \mu B + e\bar{\phi} \tag{3.4}$$

Integrating over $\mathrm{d}\tau^*$ yields

$$\partial_t \int \mathrm{d}\tau^* \left(\frac{1}{2} m {v_{G\|}}^2 + \mu B\right) \bar{F} + \int \mathrm{d}\tau^* e\bar{\phi}\partial_t \bar{F} + \int \mathrm{d}\tau^* \bar{H} \frac{1}{B_{\|}^*} \nabla_{\mathbf{z}} \cdot \left(\dot{\mathbf{z}} B_{\|}^* \bar{F}\right) = 0 \tag{3.5}$$

Note that additional terms may appear if the collision operator does not conserve the total Hamiltonian. The first term in Eq. (3.5) is the kinetic energy of the gyrocenters for the species considered, noted E_K in the following. To compute the third term, we integrate again over a phase-space volume between χ and $\chi + \delta\chi$. Because $\dot{\mathbf{z}}\cdot\nabla_{\mathbf{z}}\bar{H} = 0$, this leads to

$$\int \mathrm{d}\tau^* \bar{H} \frac{1}{B_{\|}^*} \nabla_{\mathbf{z}} \cdot \left(\dot{\mathbf{z}} B_{\|}^* \bar{F}\right) = \partial_\chi \int \mathrm{d}\tau^* \bar{H} \left(\dot{\mathbf{z}}\cdot\nabla\chi\right) \bar{F} \tag{3.6}$$

This term yields the radial flux of energy Q defined as

$$Q = \int \mathrm{d}\tau^* \bar{H} \left(\dot{\mathbf{z}} \cdot \nabla\chi\right) \bar{F} \tag{3.7}$$

For each species, we find an equation for the radial energy transport as

$$\partial_t E_K + \partial_\chi Q = W \tag{3.8}$$

where the right-hand side appears as an energy source $W = -e \int \mathrm{d}\tau^* \bar{\phi} \partial_t \bar{F}$. This term corresponds to an exchange of energy between a given species and the turbulence, and is generally referred to as turbulent heating [MOT77, WSD$^+$97, HW06, WS08], and corresponds to a transfer of energy between particles and the electromagnetic field (i.e., photons).

To obtain a local conservation equation with no source term, one should consider the total energy. We decompose W as

$$e \int \mathrm{d}\tau^* \bar{\phi} \partial_t \bar{F} = e \int \mathrm{d}\tau^* \phi \left(J \cdot \partial_t \bar{F}\right) + e \int \mathrm{d}\tau^* \left\{ \left(J \cdot \phi\right) \partial_t \bar{F} - \phi \left(J \cdot \partial_t \bar{F}\right) \right\} \tag{3.9}$$

Summing over species and using the quasi-neutrality equation (2.14), the first term in Eq. (3.9) can be identified as the potential energy

$$\begin{aligned} \sum_{species} e \int \mathrm{d}\tau^* \phi \left(J \cdot \partial_t \bar{F}\right) &= - \sum_{species} \int \frac{\mathrm{d}\theta \mathrm{d}\varphi}{\mathbf{B} \cdot \nabla\theta} \phi \nabla \cdot \left\{ \frac{n_{eq} m}{B^2} \nabla_\perp \partial_t \phi \right\} \\ &= -\frac{1}{2} \partial_t \int \frac{\mathrm{d}\theta \mathrm{d}\varphi}{\mathbf{B} \cdot \nabla\theta} \phi \nabla \cdot \left\{ \frac{n_{eq} m}{B^2} \nabla_\perp \phi \right\} \\ &= \partial_t \sum_{species} \frac{1}{2} e \int \mathrm{d}\tau^* \phi \left(J \cdot \bar{F}\right) \equiv \partial_t E_p \end{aligned} \tag{3.10}$$

Finally, the second term in Eq. (3.9) corresponds to a polarization term, due to the difference between particle and gyro-center densities. This term vanishes when integrating over the complete phase-space volume. Therefore, it is indeed the divergence of a flux in the local conservation equation. One possible approach to express this term explicitly as a flux contribution is to use the low wavenumber approximation, which is consistent with the gyrokinetic ordering, of the gyro-average operator

$$J \simeq 1 + \frac{1}{2} \nabla \cdot \left(\frac{m\mu}{e^2 B} \nabla_\perp \right) \tag{3.11}$$

At leading order in ρ_*, this expression allows one to recover the gyroaverage operator for low wavenumbers, i.e. $k_\perp \rho_i \ll 1$ where $k_\perp$ is the norm of the transverse component of the wave vector. Using this approximation, we find for each species

$$\begin{aligned} \mathcal{I}_E &= e \int \mathrm{d}\tau^* \left\{ \left(J \cdot \phi\right) \partial_t \bar{F} - \phi \left(J \cdot \partial_t \bar{F}\right) \right\} \\ &= \frac{m}{2e} \int \mathrm{d}\tau^* \left\{ \partial_t \bar{F} \, \nabla \cdot \left(\frac{\mu}{B} \nabla_\perp \phi \right) - \phi \, \nabla \cdot \left(\frac{\mu}{B} \nabla_\perp \partial_t \bar{F} \right) \right\} \end{aligned} \tag{3.12}$$

Integrating these terms by parts (see appendix D.1 for details) leads to

$$\begin{aligned} \mathcal{I}_E = {} & \frac{m}{2e} \partial_\chi \int \mathrm{d}\tau^* \partial_t \bar{F} \frac{\mu}{B} \nabla\phi \cdot \nabla\chi \quad - \frac{m}{2e} \int \mathrm{d}\tau^* \frac{\mu}{B} (\nabla_\perp \partial_t \bar{F}) \cdot (\nabla_\perp \phi) \\ & - \frac{m}{2e} \partial_\chi \int \mathrm{d}\tau^* \phi \frac{\mu}{B} \nabla(\partial_t \bar{F}) \cdot \nabla\chi + \frac{m}{2e} \int \mathrm{d}\tau^* \frac{\mu}{B} (\nabla_\perp \phi) \cdot (\nabla_\perp \partial_t \bar{F}) \end{aligned} \tag{3.13}$$

The second and fourth terms cancel each other out. The remaining terms can be expressed in a more compact form using the gyrocenter perpendicular pressure $\bar{P}_\perp = \int \mathrm{d}^3v\bar{F}\mu B$. This leads to the following conservation equation summed over all species

$$\partial_t E_K + \partial_t E_p + \partial_\chi Q + \partial_\chi Q_{pol} = 0 \tag{3.14}$$

where

$$E_K = \sum_{species} \int \mathrm{d}\tau^* \left(\frac{1}{2}m{v_{G\|}}^2 + \mu B\right)\bar{F} \tag{3.15}$$

$$E_p = \sum_{species} \frac{1}{2}\int \mathrm{d}\tau^* e\phi J\cdot\bar{F} \tag{3.16}$$

$$Q = \sum_{species} \int \mathrm{d}\tau^* \bar{H}(\dot{\mathbf{z}}\cdot\nabla\chi)\bar{F} \tag{3.17}$$

$$Q_{pol} = \sum_{species} \frac{m}{2e}\int \frac{\mathrm{d}\theta\mathrm{d}\varphi}{\mathbf{B}\cdot\nabla\theta}\frac{1}{B^2}\Big\{-\phi\nabla(\partial_t\bar{P}_\perp)\cdot\nabla\chi + \partial_t\bar{P}_\perp\nabla\phi\cdot\nabla\chi\Big\} \tag{3.18}$$

We recall that, although the polarization term is necessarily the divergence of a flux term, the expression for Q_{pol} given here is not exact as it relies on an approximation of the gyroaverage operator.

3.1.3 Toroidal momentum

Formally, the derivation of a conservation law for toroidal angular momentum is very similar to what was done for energy in the previous section. The general idea is to multiply the conservative gyrokinetic equation (2.18) by an invariant of motion. For the energy, this invariant was the gyro-center Hamiltonian $\bar{H}$ given by Eq. (2.5). In a tokamak geometry such as described in section 2.1.1, the equilibrium motion of particles (in the adiabatic approximation) is characterized by three motion invariants: the magnetic moment μ, the energy $H_{eq} = mv_\|^2/2 + \mu B + \phi_{eq}$ and the toroidal canonical momentum which reads

$$p_\varphi = -e\chi + mR^2\,\dot{\mathbf{z}}\cdot\nabla\varphi \tag{3.19}$$

This third motion invariant is a direct consequence of the axisymmetry of the unperturbed problem. Thus, the following derivation can be understood as an application of Noether's theorem [Noe18]. p_φ is an invariant of the *unperturbed particle motion*, i.e. related to the Hamiltonian $H_{eq} = \frac{1}{2}mv_\|^2 + \mu B + \phi_{eq}$ where the equilibrium electric potential ϕ_{eq} does not depend on the toroidal angle.

In the context of gyrokinetic theory, the motion of gyrocenters – rather than particles – should be considered. The unperturbed motion of gyrocenters also exhibits three motion invariants, including the gyrocenter toroidal canonical momentum P_φ defined as

$$P_\varphi = mu_\varphi - e\chi \tag{3.20}$$

with the notation $u_\varphi = (I/B)v_{G\|}$. P_φ is an exact invariant of the *unperturbed gyrocenter motion* described by the Hamiltonian $\bar{H}_{eq} = \frac{1}{2}m{v_{G\|}}^2 + \mu B + \bar{\phi}_{eq}$, which corresponds to collisionless motion in a fully axisymmetric system. When axisymmetry is broken, which can occur for instance due to turbulence (see chapter 4) or magnetic field ripple (chapter 6), P_φ is no longer a motion invariant. In particular, when the electric potential becomes non-axisymmetric, the evolution of P_φ is governed by the equation $\mathrm{d}_t P_\varphi = -e\partial\varphi\bar{\phi}$. This result can be obtained from the expression of the gyrokinetic Poisson brackets Eq. (2.7). Details of the calculation are presented in appendix E.

It is important to note that P_φ is different from the particle canonical momentum, which should be expected as the equations for particle motion and for gyro-center motion are not identical. Formally, both can be derived as $\partial \mathrm{L}/\partial\dot{\varphi}$ where L is a Lagrangian, but for different dynamical systems and therefore different Lagrangians. However, the difference between the two canonical momenta is of order $\mathcal{O}(\rho_*^2)$ [BH07]. From the definition of P_φ given by Eq. (3.20), we define the local toroidal angular momentum as

$$\mathcal{L}_\varphi = \sum_{species} m \int \mathrm{d}\tau^* u_\varphi \bar{F} \tag{3.21}$$

Note that $\mathcal{L}_\varphi$ is the momentum for *gyrocenter*, which differs from the particle momentum by terms of order $\mathcal{O}(\rho_*^2)$. In order to derive a local conservation equation for $\mathcal{L}_\varphi$, we multiply the conservative gyrokinetic equation (2.18) by P_φ and integrate over all variables other than χ, leading to

$$m\partial_t \int \mathrm{d}\tau^* u_\varphi \bar{F} - e\int \mathrm{d}\tau^* \chi \partial_t \bar{F} + e\int \mathrm{d}\tau^* \bar{F} \partial_\varphi \bar{\phi} + \partial_\chi \int \mathrm{d}\tau^* (\dot{\mathbf{z}}\cdot\nabla\chi)\bar{F}\,(m u_\varphi - e\chi) = 0 \tag{3.22}$$

where we have used the fact that $\mathrm{d}_t P_\varphi = -e\partial\varphi\bar{\phi}$. Using the local conservation of number of particles Eq. (3.1), the second term can be written as $\chi\partial_\chi \mathcal{J}^\chi$. We also identify the last term as $-\partial_\chi(\chi\mathcal{J}^\chi)$. Summing over all species this leads to

$$\partial_t \mathcal{L}_\varphi + \partial_\chi \Pi_\varphi^\chi + \partial_\chi T_\varphi^\chi = \mathcal{J}^\chi \tag{3.23}$$

where

$$\Pi_\varphi^\chi = \sum_{species} m \int \mathrm{d}\tau^* \bar{F} u_\varphi v_G^\chi \tag{3.24}$$

$$T_\varphi^\chi = \sum_{species} e \int^\chi \mathrm{d}\chi \int \mathrm{d}\tau^* \bar{F} \partial_\varphi \bar{\phi} \tag{3.25}$$

$$\mathcal{J}^\chi = \sum_{species} e \int \mathrm{d}\tau^* v_G^\chi \bar{F} \tag{3.26}$$

Equation (3.23) is an *exact* equation for the transport of gyrocenter toroidal momentum, in the sense that it was obtained directly from the gyrokinetic model, with no additional assumptions of orderings. Note that this equation can be linked to the result derived in [PC10] by using a different approach for the derivation and applying additional approximations, as described in appendix F.

The fact that the third term in equation (3.23), $\partial_\chi T_\varphi^\chi$, can be expressed as the divergence of a flux is not trivial and requires further discussion. This can be shown by multiplying the gyrokinetic equation (2.18) by P_φ (instead of only u_φ) and integrating over the complete phase-space, i.e. using $\mathrm{d}\tau = \mathrm{d}\chi \mathrm{d}\tau^*$. This leads to

$$\partial_t \int \mathrm{d}\tau P_\varphi \bar{F} + e\int \mathrm{d}\tau \bar{F} \partial_\varphi \bar{\phi} + \int \mathrm{d}\tau \frac{1}{B_\|^*} \nabla_{\mathbf{z}} \cdot \left(\dot{\mathbf{z}} B_\|^* P_\varphi \bar{F}\right) = 0 \tag{3.27}$$

The canonical momentum P_φ is an invariant of the equilibrium motion. Moreover, in an isolated system, the only perturbations are internal to the system. More precisely, the perturbation considered in the gyrokinetic model used here is the electric potential, which is computed self-consistently from the distribution function using the quasi-neutrality equation. Therefore, $\int \mathrm{d}\tau P_\varphi \bar{F}$ is an invariant of the isolated system, and the first term in Eq. (3.27) vanishes. The third term also vanishes up to surface terms. Therefore, for an isolated system, $\int \mathrm{d}\tau \bar{F} \partial_\varphi \bar{\phi} = 0$, which implies that $\int \mathrm{d}\tau^* \bar{F} \partial_\varphi \bar{\phi}$ is the divergence of a flux term, and justifies the fact that it was expressed as $\partial_\chi T_\varphi^\chi$ in the local conservation equation (3.21). Note that in the case of a non-isolated system, momentum can be exchanged at the boundaries of the system due to the two divergence terms in Eq. (3.27).

The result that the term $e \int \mathrm{d}\tau^* \bar{F} \partial_\varphi \bar{\phi}$ in the local conservation equation (3.23) corresponds to the divergence of a flux is very general. In particular, it does not depend on details of the quasi-neutrality equation. This result can be further ensured through the symmetry properties of the gyroaverage operator, which verifies

$$\sum_{species} \int \mathrm{d}\tau \bar{F} \partial_\varphi \bar{\phi} = \sum_{species} \int \mathrm{d}\tau J \cdot \bar{F} \partial_\varphi \phi \tag{3.28}$$

Using the quasi-neutrality equation (2.14) it is straightforward to show that the right-hand side of Eq. (3.28) is exactly zero with appropriate boundary conditions. When the gyroaverage operator is replaced by a simplified expression, as is often the case in numerical simulations, it is important for the conservation properties of the system to verify that the reduced operator still verifies Eq. (3.28) [SS10]. One way to guarantee this condition is to choose a Hermitian gyroaverage operator. This is the case for instance of the Padé approximation (see section 2.3.3) as it is used in the Gysela code, i.e. Eq. (2.46).

Physical interpretation of the toroidal momentum fluxes

The first flux in the local conservation equation for toroidal angular momentum (3.23), Π_φ^χ, corresponds to the off-diagonal $(\varphi\chi)$ component of the Reynolds stress. This term, and specifically the contribution related to a non-axisymmetric $E \times B$ velocity, describes the generation of large-scale flows from small-scale turbulence. The role of the Reynolds stress in generating toroidal rotation will be analyzed more precisely in section 4.

The second flux, T_φ^χ, can be interpreted as the polarization flux of momentum, i.e. the equivalent of the polarization flux of energy Q_{pol} defined in equation (3.18). To obtain an explicit expression of T_φ^χ, we can use the low wavenumber approximation of the gyroaverage operator already presented, Eq. (3.11). As mentioned previously, this expression is equivalent to the exact operator for low wavenumbers at leading order in ρ_*. Moreover, this reduced operator verifies the symmetry property Eq. (3.28) of the exact operator, which is necessary in order to preserve the conservative nature of the gyrokinetic model. Using this approximation and following the calculations in appendix G, one can express the polarization flux of momentum as

$$T_\varphi^\chi = -\int \frac{\mathrm{d}\theta \mathrm{d}\varphi}{\mathbf{B} \cdot \nabla\theta} \left\{ \frac{n_{eq} m}{B^2} E^\chi E_\varphi + \sum_{species} \frac{1}{2} \frac{m}{eB^2} \left(E^\chi \mathcal{G}_\varphi + \mathcal{G}^\chi E_\varphi \right) \right\} \tag{3.29}$$

up to higher order terms in $k_\perp \rho_i$. Conventional covariant notations are used for the components of the electric field $\mathbf{E} = -\nabla\phi$ and $\mathcal{G} \equiv -\nabla \bar{P}_\perp$, where we recall that $\bar{P}_\perp = \int \mathrm{d}^3 v \bar{F} \mu B$ is the gyrocenter perpendicular pressure.

The result is consistent with previous work by McDevitt *et al.* [MDGH09b] for parallel momentum generation. Assuming $\bar{P}_\perp = 0$, T_φ^χ takes the form of the off-diagonal component of a Maxwell stress linked to polarization effects. More precisely, it is simply the usual vacuum Maxwell stress, but replacing the vacuum permittivity ϵ_0 by $n_{eq}m/B^2$. This corresponds to the classical Minkowski expression of the Maxwell stress tensor [Jac75]. One can relate this result to the fact that, as previously noted in section 2.2.4, the quasi-neutrality condition used in the gyrokinetic model, Eq. (2.16), takes the form of a Poisson equation with the same substitution. The additional terms, proportional to derivatives of the perpendicular pressure $\bar{P}_\perp$, correspond to Finite Larmor Radius (FLR) effects. They can be interpreted as a generalization of the Maxwell stress in the case of hot plasmas.

Finally, the term on the right-hand side of the local conservation equation (3.23), $\mathcal{J}^\chi$, is the radial current of gyrocenters. This term appears formally as a local source of toroidal angular momentum, and it is expected to be small in electrostatic simulations assuming adiabatic electron response. We will show in the following that this term can actually be interpreted as an exchange of momentum between the gyrocenters and the electric field.

3.1.4 Poloidal momentum: vorticity equation

Let us recall the equation previously derived in section 3.1.1 for the local conservation of charge density

$$\partial_t \bar{\rho} + \partial_\chi \mathcal{J}^\chi = 0 \tag{3.30}$$

where the charge density $\bar{\rho}$ is defined in Eq. (3.2) and the radial current of gyrocenters $\mathcal{J}^\chi$ is given by Eq. (3.3). Interestingly, the conservation equation for density can also be interpreted as a vorticity equation, by expressing the charge density $\bar{\rho}$ as a function of the electric potential ϕ. The idea is to rewrite the distribution function as $\bar{F} = J\cdot\bar{F} + (\bar{F} - J\cdot\bar{F})$, using the quasi-neutrality equation (2.16) to express the first term and the low wavenumber approximation Eq. (3.11) of the gyroaverage operator to compute the second. Up to higher order terms in $k_\perp \rho_i$, this leads directly to

$$\bar{\rho} = -\int \frac{\mathrm{d}\theta \mathrm{d}\varphi}{\mathbf{B}\cdot\nabla\theta} \nabla\cdot\left(\frac{n_{eq}m}{B^2}\nabla_\perp\phi + \sum_{species} \frac{1}{2}\frac{m}{eB^2}\nabla_\perp \bar{P}_\perp\right) \tag{3.31}$$

where the gyrocenter density is the sum of the fluid vorticity ($\sim \nabla^2\phi$) and a perpendicular pressure term, interpreted as a FLR correction leading to a *generalized vorticity*. Integrating the vorticity equation (3.30) once leads to

$$\partial_t \sigma = -\mathcal{J}^\chi \tag{3.32}$$

where we define the generalized polarization σ as

$$\sigma = \int \frac{\mathrm{d}\theta \mathrm{d}\varphi}{\mathbf{B}\cdot\nabla\theta}\left(\frac{n_{eq}m}{B^2}E^\chi + \sum_{species}\frac{1}{2}\frac{m}{eB^2}\mathcal{G}^\chi\right) \tag{3.33}$$

This appears as the χ component of the polarization vector [BH07], plus an additional term corresponding to FLR corrections. Up to these FLR effects, σ is proportional to the poloidal component of the $E \times B$ drift velocity. Thus the evolution equation for the polarization, Eq. (3.32), governs the radial electric field, which contributes to the poloidal flow.

The radial current $\mathcal{J}^\chi$ can be decomposed into two components coming respectively from the curvature and $E \times B$ drifts. Expressions of both components of the radial current are presented in appendix H. The curvature term appears as the neoclassical viscous damping term, describing the relaxation of the poloidal velocity to its neoclassical value [KDG91]. The $E \times B$ contribution corresponds to the (off-diagonal) perpendicular component of the Reynolds stress. A relation between the flux of vorticity and the Reynolds stress is thus obtained, as expected from Taylor's theorem [Tay15].

3.1.5 Total momentum conservation and steady-state

In the previous sections, we have derived two local conservation equations for momentum. The first equation describes the evolution of gyrocenter toroidal angular momentum

$$\partial_t \mathcal{L}_\varphi + \partial_\chi \Pi_\varphi^\chi + \partial_\chi T_\varphi^\chi = \mathcal{J}^\chi \tag{3.34}$$

The second, obtained by integrating the generalized vorticity equation, is a conservation equation for polarization, which is directly linked to poloidal momentum

$$\partial_t \sigma = -\mathcal{J}^\chi \tag{3.35}$$

Notice that the source terms on the right-hand side of equations (3.34) and (3.35) are exactly opposite. Therefore a conservation equation without any source term can be obtained by summing these two equations:

$$\partial_t \left(\mathcal{L}_\varphi + \sigma\right) + \partial_\chi \left(\Pi_\varphi^\chi + T_\varphi^\chi\right) = 0 \tag{3.36}$$

This equation can be understood as a local conservation of *total* toroidal momentum, with σ corresponding to the toroidal momentum carried by the field. In the Minkowski formulation, the field momentum density is proportional to the Poynting vector, and reads $\mathbf{g} = \mathbf{D} \times \mathbf{B}$, where $\mathbf{D} = \epsilon_0 \mathbf{E} + \mathbf{P} = -(n_{eq} m/B^2)\nabla_\perp \phi$. Taking the toroidal component of $\mathbf{g}$, i.e. $g_\varphi = R^2 \mathbf{g} \cdot \nabla\varphi$, one finds the radial component of the polarization vector, $(n_{eq} m/B^2)E^\chi$. Neglecting FLR corrections, this corresponds to the definition of the generalized polarization σ given by Eq. (3.33). Thus, Eq. (3.36) describes the local conservation of *total* toroidal momentum, with $\mathcal{L}_\varphi$ accounting for gyrocenter momentum and σ corresponding to field momentum. This formulation is consistent with results obtained in both gyrokinetic [SS10] and fluid [Bri10] approaches, with similar expressions for the toroidal momentum carried by the field.

The equations obtained for momentum conservation are particularly useful to describe the time-independent mean flows in tokamaks. In the steady-state regime and in the absence of momentum sources, one has

$$\mathcal{J}^\chi = 0 \tag{3.37}$$

$$\partial_\chi \Pi_\varphi^\chi + \partial_\chi T_\varphi^\chi = 0 \tag{3.38}$$

In the first equation, the radial current $\mathcal{J}^\chi$ is the sum of two contributions. The first contribution (see appendix H.1) comes from the curvature drift, and corresponds to neoclassical viscous damping, which forces the poloidal velocity to relax to its neoclassical value. This friction competes with the turbulence driven radial current, which appears as the transverse component of the Reynolds stress (see appendix H.2). Therefore, the equation $\mathcal{J}^\chi = 0$ describes the competition between neoclassical damping and turbulent generation of poloidal flows. The competition between these two effects, still largely a debated issue, was recently investigated in gyrokinetic simulations [DPGS$^+$09, VBV$^+$12].

In the second equation, Π_φ^χ is the off-diagonal $(\varphi\chi)$ component of the Reynolds stress, while T_φ^χ is the corresponding component of the Maxwell stress obtained from the polarization field. In the fully axisymmetric problem, the solutions to this equation exhibit a degeneracy, which can be alleviated by taking into account a breaking of the axisymmetry, for instance by turbulence (section 4) or magnetic field ripple (section 6).

3.2 Numerical test of the momentum conservation

In this section, we verify numerically the conservation properties of the gyrokinetic model necessary to describe the mean flows and radial electric field. As previously mentioned, the equations implemented in Gysela correspond to the model which was used for the analytical derivation, in the specific case of adiabatic electrons and a single kinetic ion species. We recall in particular that the Padé approximation chosen for the gyroaverage operator, although it overdamps small scales (see section 2.3.3), verifies the symmetry property Eq. (3.28) necessary to preserve the conservation properties of the gyrokinetic model. Also, the collision operator implemented in Gysela locally conserves density, momentum and energy, as detailed in section 2.3.2.

3.2.1 Radial force balance

In the fluid description, the radial electric field and the flows are related via the force balance equation [HH76]. It is important to ensure that this relation holds also in gyrokinetics [GDPN+09]. The radial force balance can be recovered analytically from the gyrokinetic description, as shown in appendix I, yielding the standard fluid expression

$$\partial_\chi \phi_{eq} + \frac{\partial_\chi P_{eq}}{n_{eq} e} + \frac{B}{I} V_{\parallel eq} = q \frac{B^2 R^2}{I^2} \left(\mathbf{V} \cdot \nabla \theta \right) \tag{3.39}$$

where the equilibrium density n_{eq}, pressure P_{eq}, velocity $V_{\parallel eq}$ and potential ϕ_{eq} are functions of $-P_\varphi / e$ (which is approximately equal to χ at first order in ρ_*).

In order to check that the force balance equation is verified numerically, we compare the poloidal velocity directly computed in Gysela with the expected velocity from the force balance equation, i.e. the left-hand side of Eq. (3.39). This result was previously verified in Gysela simulations for a wide range of parameters such as temperature gradient, collisionality and normalized gyroradius ρ_* [DPGS+09, DPDG+11]. We present here the result from the simulation described in section 2.4, recalling the key dimensionless parameters of the simulation: the normalized gyro-radius $\rho_* = 1/512$ (at mid-radius) and collisionality $\nu^* = 0.1$. In the present simulation, the heat source injected mainly parallel energy, leading to a strongly anisotropic pressure. However, only the perpendicular component of the diagonal pressure tensor enters the force balance equation. As shown in Fig. 3.1, excellent agreement is obtained, with a precision of approximately 2%. Notice that the balance results mainly from a competition between radial electric field, which dominates the small-scale variations of the poloidal velocity, and perpendicular pressure.

This agreement is obtained very robustly, whether or not the quantities considered are time-averaged. This result is somewhat surprising considering the time scales involved in the problem. The pressure, which acts as a force in the balance equation, is generally considered as a consequence of collisions, and one might expect the force balance to be recovered on time scales of the order of the collision time. However, in turbulent simulations with very low collisionality – and $\nu_{ii} \ll \omega_{turb}$ – the radial force balance is at any given time in the simulation.

3.2.2 Toroidal angular momentum

A local conservation equation for toroidal angular momentum was derived in section 3.1.3. To test this conservation numerically, we compare in Fig. 3.2a the time derivative of the

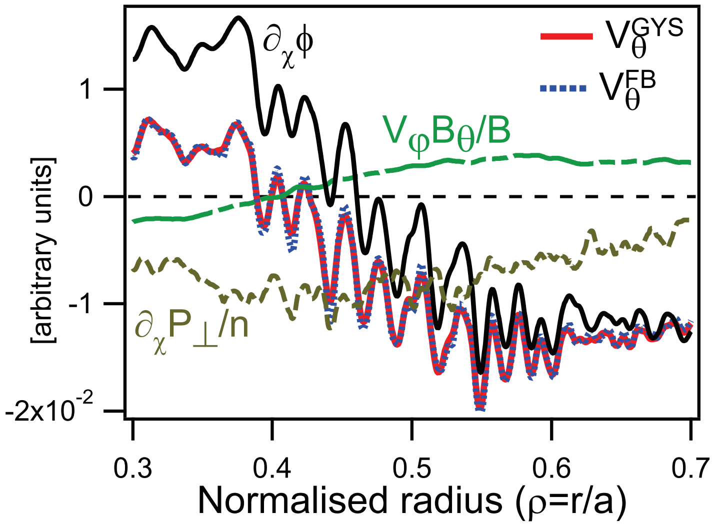

Figure 3.1: Numerical test of the radial force balance, comparing the poloidal velocity as computed directly in the code (v_θ^{GYS}) and as a sum of the other terms in the radial force balance equation (v_θ^{FB}).

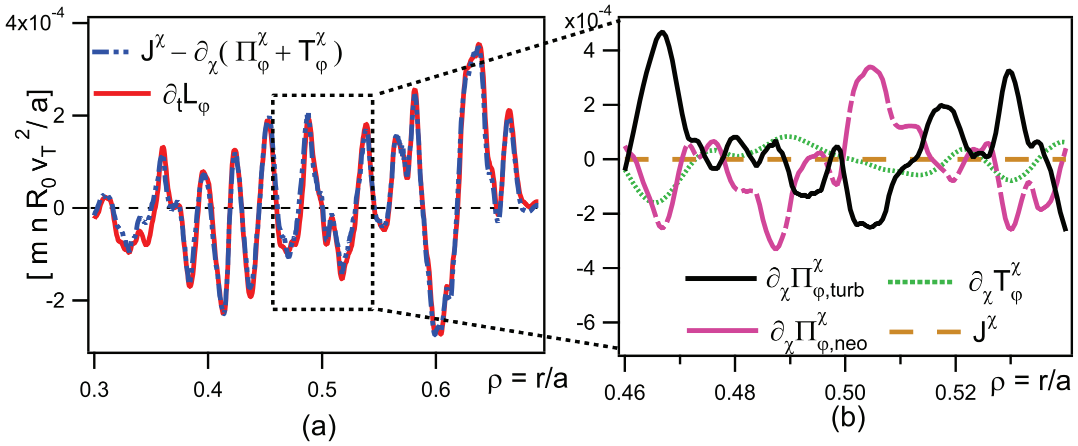

Figure 3.2: (a) Numerical test of the conservation of toroidal angular momentum, comparing the time derivative of angular momentum (i.e. $\partial_t \mathcal{L}_\varphi$) to the sum of the other terms in Eq. (3.23), (b) plotted separately for a smaller radial domain.

toroidal momentum $\mathcal{L}_\varphi$ with the sum of the other terms in Eq. (3.23), for the same simulation considered in the previous section, showing excellent agreement.

The quantities are averaged over a significant time interval in the non-linear statistical steady-state (approximately $10^4 \omega_c^{-1}$ where ω_c is the ion cyclotron frequency) and are normalized to $m_i n R_0 v_T^2/a$ where R_0 is the major radius at the magnetic axis, v_T is the thermal velocity and a is the minor radius. Note that the conservation is verified despite strong variations of the momentum flux both radially and in time. This result was robustly obtained in several nonlinear simulations using GYSELA with a wide range of parameters in the dimensionless numbers ρ_* and ν^*.

The contributions of the different terms in equation (3.23) are detailed in Fig. 3.2b, separating the Reynolds stress (Π_φ^χ) into its turbulent and neoclassical components, i.e. splitting v_G^χ in expression (3.24) into $E \times B$ and magnetic drifts. Note that the neoclassical stress, although it corresponds to momentum transport by the magnetic drifts, is present due to symmetry breaking by turbulence only, as magnetic field ripple (see section 6) is not included in this simulation. As expected, contributions from the radial currents of guiding-centers ($\mathcal{J}^\chi$) are negligible in the statistical steady-state regime (approximately 0.1% of the total magnitude, i.e. a factor ρ_* smaller than $\partial_t \mathcal{L}_\varphi$). The balance of toroidal angular momentum results mainly from a competition between turbulent and neoclassical stresses, with a significant contribution from the polarization stress.

3.3 Summary

In addition to standard conservation laws for charge density and energy, we have derived a local conservation equation for gyrocenter toroidal angular momentum in the context of gyrokinetics, Eq. (3.23). Within the gyrokinetic framework, this conservation equation is exact as it was obtained directly from the gyrokinetic model, with no additional assumptions of orderings. Moreover, the *gyrocenter* and *particle* toroidal momentum differ only by terms of order $\mathcal{O}(\rho_*^2)$. This local conservation was verified numerically with excellent precision in nonlinear gyrokinetic simulations using GYSELA

An evolution equation was also obtained for poloidal momentum, by reinterpreting the charge density conservation as a vorticity equation. The local conservations of toroidal and poloidal momentum, associated with the radial force balance equation, which was also verified numerically, provide a complete and accurate description of mean flows in gyrokinetics.

Chapter 4

Toroidal symmetry breaking by electrostatic turbulence

> Immanquablement, ces vents isolés se rencontrèrent, contrecarrant leurs puissances, les cumulant parfois, s'entredéviant et s'entrecalmant… Ainsi naquirent les premiers tourbillons, ainsi commença la lenteur. De ce chaos de matière alentie, brassée par l'hélice des vortex, émergea les volutes relatives du lentevent, ce cosmos des vitesses vivables, d'où nous provenons.
>
> ALAIN DAMASIO, *La Horde du Contrevent*, 2004

As demonstrated in section 3.1.3, the fact that the canonical toroidal momentum is an invariant of unperturbed guiding-center motion prevents the generation of toroidal rotation in an axisymmetric system. Thus, for intrinsic rotation to appear, a breaking of the axisymmetry is required. One important mechanism which can lead to toroidal symmetry breaking is plasma micro-turbulence, and in particular electrostatic ITG turbulence.

In order to describe in detail the generation of *intrinsic* toroidal rotation from turbulence, we consider only simulations with a vanishing initial profile for toroidal rotation and no extrinsic momentum source. In section 4.1, we present the different phases in the buildup of an intrinsic rotation profile in the simulation. The statistical properties of turbulent momentum transport are analyzed in section 4.2, emphasizing the strong link with heat transport. Different possible mechanisms leading to the turbulent generation of intrinsic toroidal rotation are considered in section 4.3, and their relative importance is investigated.

4.1 Intrinsic toroidal rotation generated by turbulence

We consider a GYSELA simulation with the normalized gyroradius $\rho_* = 1/512$ at mid-radius and collisionality $\nu^* = 0.1$. The parameters are those already detailed in section 2.4. We recall in particular that the density and temperature profiles were initialized with $d_r \log n = R_0/L_n = 2$ and $d_r \log T = R_0/L_T = 12$, constant in the simulation domain except near the radial boundaries. The density profile remains constant due to adiabatic electron response while the temperature gradient eventually stabilizes around $R_0/L_T \simeq 11.5$.

4.1.1 Rotation buildup

As explained in section 2.4, GYSELA simulations are initialized with a turbulent drive above the threshold for the ITG instability, but in a non-turbulent initial state. The simulation thus begins with a linear phase, where resonant modes grow exponentially. This linear growth phase is followed by a large relaxation event, propagating outward in the radial direction at a speed higher than the ion diamagnetic velocity. This relaxation is characterized by a strong front of positive (i.e. outward) heat flux[1].

From a vanishing initial profile of toroidal rotation, we observe the generation of significant intrinsic rotation during the initial relaxation event, as shown in Fig. 4.1, where both the turbulent heat flux and the generated toroidal momentum are plotted. The resulting flow structure is dipolar, which is consistent with the existence of a local conservation law for toroidal angular momentum, Eq. (3.23), with no source term as the radial current of gyrocenters is negligible. Indeed, the radial integral of the toroidal angular momentum resulting from this dipole is vanishing. The generation of intrinsic rotation clearly follows the outward propagation of the front of heat flux. In other words, the maxima of turbulent heat flux and momentum flux ($\partial_t \mathcal{L}_\varphi$) propagate together. This also coincides with a large turbulent Reynolds stress, which is the dominant contribution to the momentum flux during the relaxation, as is the case in the statistical steady-state (Fig. 3.2b).

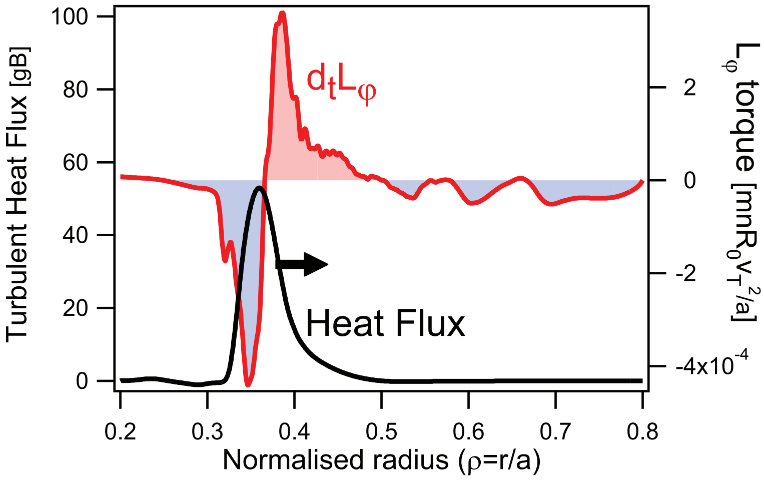

Figure 4.1: Propagation of a front of turbulent heat flux and generation of toroidal rotation. The turbulent heat flux is in gyro-Bohm units (see section 5.2).

Another way to visualize the front observed in Fig. 4.1 is to represent the momentum torque as a function of the heat flux, for all values of the radius, as shown in Fig. 4.2a.[2] As the dipolar structure of toroidal momentum generated here is mainly cause by the turbulent Reynolds stress, a clearer picture is obtained by representing the cycle in terms of the two turbulent fluxes: the heat flux and the Reynolds stress. The result is shown in Fig. 4.2b. With this representation, one can clearly identify a cycle, as both fluxes are vanishing at the inner and outer radial boundaries. An important result is that the largest value of the Reynolds stress appears to propagate ahead (i.e., is located further out

---

[1] Although they are identical here, note the important distinction between (i) the direction of propagation of the front and (ii) the direction of the flux.

[2] The cycle could also be analyzed through the time evolution of the quantities at a given radius. The choice of studying instead the radial evolution at a given time is motivated by the fact that the resolution of the diagnostics in the simulation is greater in the radial direction than in time.

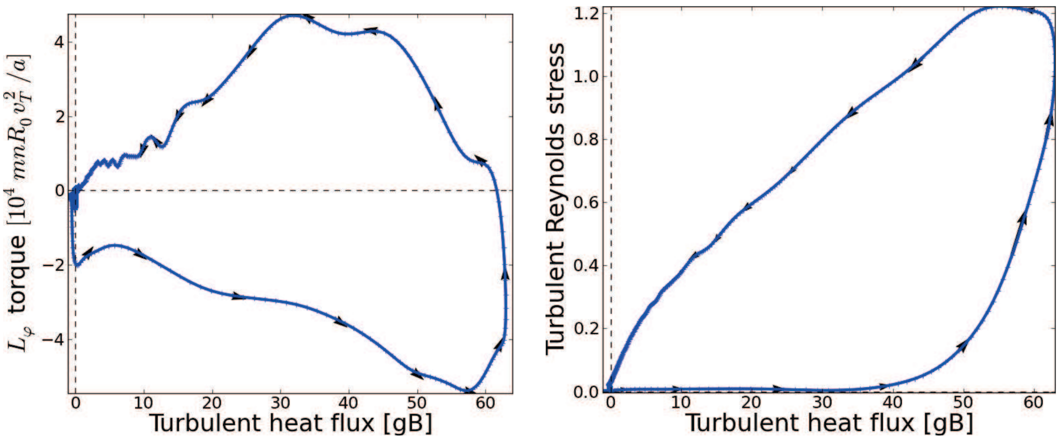

(a) (b)

Figure 4.2: Representation of the initial turbulent front (Fig. 4.1) as a cycle in heat flux and (a) momentum torque ($\partial_t \mathcal{L}_\varphi$) or (b) Reynolds stress. The cycles start and finish with both fluxes at zero, the arrows represent the direction of increasing radius.

radially) of the maximum heat flux. More precisely, the delay between the two maxima in Fig. 4.2b is of $5.7\,\rho_i$. The propagation velocity of the front can also be estimated by following the maximum of either flux, and is found to be of roughly five times the diamagnetic velocity, i.e. $V_{front} \simeq 5\rho_* v_T$ where v_T is the ion thermal velocity. Thus, one can compute the delay between the maxima of heat flux and Reynolds stress, leading to approximately $580\,\omega_c^{-1}$. The relation between heat and momentum transport will be explored further in section 4.2.

Formally, the Reynolds stress can be decomposed into diffusive, convective [PAS07, HDGR07] and so-called *residual* contributions [DMG+08, PSC+09] as follows

$$\Pi_\varphi^\chi = -\chi_\varphi \frac{\partial v_\varphi}{\partial r} + V v_\varphi + \Pi_\varphi^{\chi res} \tag{4.1}$$

where χ_φ is a diffusion coefficient and V is a momentum pinch velocity and $\Pi_\varphi^{\chi res}$ is the residual Reynolds stress. Because the simulation was initialized with very low initial toroidal rotation, the Reynolds stress generating toroidal rotation during the initial burst contains only the residual stress. However, in the following, for full-f simulations, as the Reynolds stress is computed self-consistently with an evolving equilibrium, the three contributions cannot be distinguished. Thus, the results concerning toroidal momentum transport are obtained from the *total* Reynolds stress, including residual stress contributions.

The conservation law for toroidal angular momentum, Eq. (3.23), in the absence of an extrinsic source, implies that momentum is globally conserved in the simulation domain. Thus, in the absence of momentum fluxes at the boundaries, one would only obtain dipolar-like structures, with no net generation of toroidal rotation [IUAT09], i.e. $\int \mathrm{d}\chi \mathcal{L}_\varphi$ would be constant. In GYSELA, so-called "no-slip" (i.e. $V_\parallel = 0$) boundary conditions are imposed at the edge of the simulation domain. With this type of boundary conditions, non-vanishing edge fluxes, and therefore a *net* generation of toroidal rotation, are possible. This occurs after the propagation of the initial turbulent front (Fig. 4.1), when turbulence has spread to the edge regions of the simulation domain, where spatial diffusion is applied (see page 21). During this phase of the simulation, a net profile of toroidal rotation builds up with a dominant contribution in the co-current direction, as shown in Fig. 4.3. Note that the

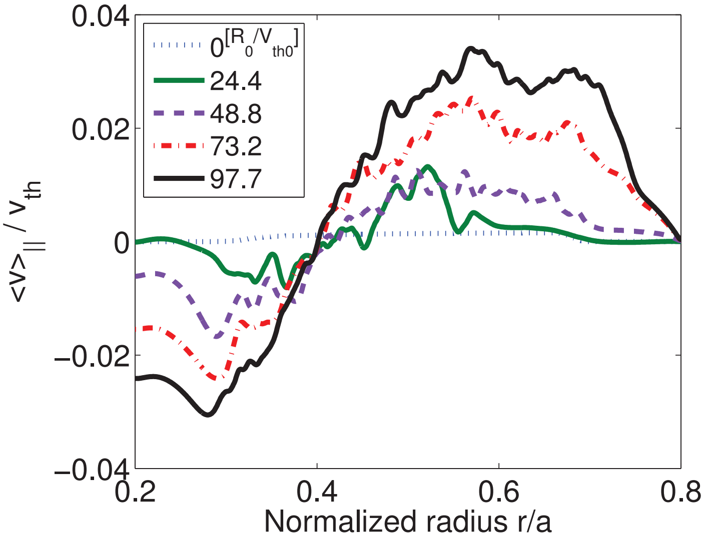

Figure 4.3: Time evolution of the radial profile of parallel flow. The velocity is normalized to the thermal velocity v_{th}, while time is normalized to R_0/v_{th} where R_0 is the major radius at the magnetic axis

initial distribution function was chosen as a canonical Maxwellian [ITK03, DPGS+08], leading to a small but finite initial toroidal flow.

Eventually, the peak of the co-current rotation profile reaches a parallel Mach number of a few percent, which is of the order of – though somewhat smaller than – typical experimental observations. We emphasize the fact that the toroidal rotation profile is still slowly evolving at the end of the simulation, due to limitations in the available computer resources. In order to obtain a steady-state of the flows, simulations on time scales of the order of the confinement time are necessary. For the ρ_* value considered here, such simulations are not accessible with the current resources. Reaching a statistical steady-state for turbulence occurs on shorter time scales, and the temperature profile is initialized close to an equilibrium with respect to the level chosen for the heat source, but the mean flows are still slowly evolving at the end of the simulation

4.1.2 Large-scale avalanches of toroidal momentum flux

Once turbulence has reached its statistical steady-state and the rotation profile is only slowly evolving, we can study the dynamics of toroidal momentum transport. Previously, turbulence studies of tokamak plasmas using gyrokinetic codes have focused primarily on the dynamics of heat transport. One important result of this work, especially in flux driven simulations, is the observation of avalanche-like events for the heat flux. The term “avalanche” is used to describe large-scale transport events characterized by a propagating front of large outward heat flux. These fronts propagate at fractions of the diamagnetic velocity, over distances larger than the typical correlation length of turbulence. Such avalanches have been well documented for GYSELA simulations [SGA+10, SGA+11] as well as with other global gyrokinetic codes [CW03b, IUAT09, MJT+09, GLB+11, JI12], regardless of details of the simulations. This intermittent transport has been found to recover the basic properties of models based on self-organized criticality (SOC) [BTW87, HK92, CNLD96], in particular the typical $1/f$ decay of the frequency Fourier spectrum [SGA+10, MJT+09].

Momentum transport is found to exhibit very similar avalanche-like structures. In Fig. 4.4, the space-time evolutions of the flux-surface averaged turbulent heat flux and Reynolds stress near mid-radius are plotted, from the simulation previously described in section 2.4 where the normalized gyroradius is $\rho_* = 1/512$. The time slice corresponds to the phase of the simulation where turbulence has reached a steady-state, while flows are still slowly evolving.

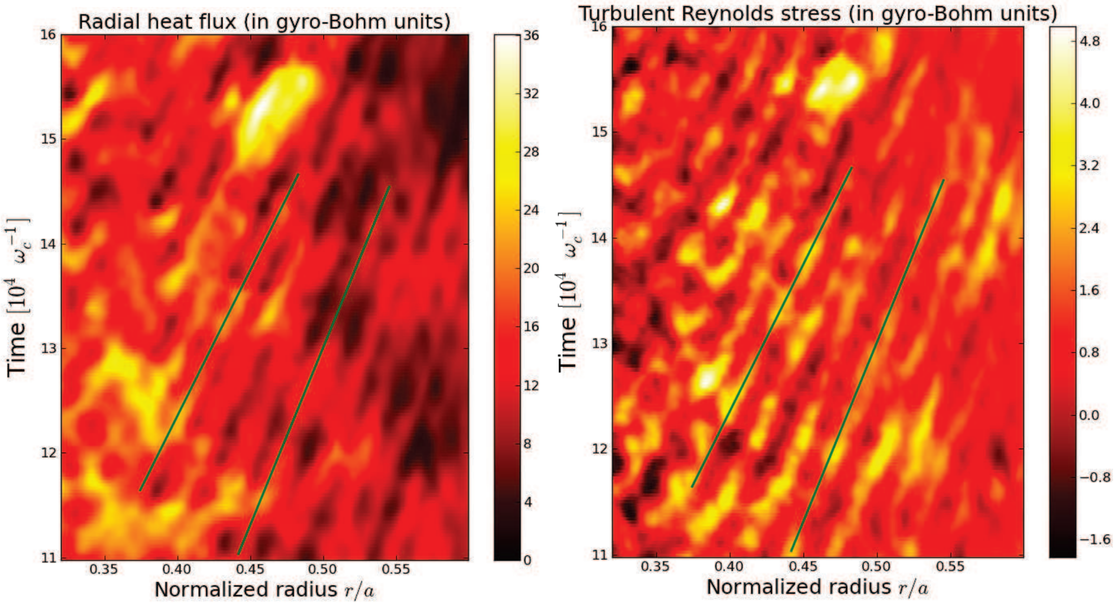

(a)

(b)

Figure 4.4: Space-time evolution of the turbulent heat flux (left) and turbulent Reynolds stress (right) for the same simulation with the normalized gyroradius $\rho_* = 1/512$. The horizontal axis corresponds to normalized radius r/a. The green straight lines are identical in both figures.

The two plots show important similarities. First of all, large-scale avalanches are clearly visible both for the heat flux and the momentum flux, despite the flux-surface average. Moreover, in both cases, fronts are propagating both inward and outward. Studying the figures in detail, it appears that the same avalanches transport both heat and momentum. To highlight this, two straight lines are represented on both plots at the same coordinates, following two outward propagating fronts. The two avalanches are well captured by this line on both graphs, suggesting that they are responsible for both heat and momentum transport. The propagation velocity of the two fronts are not identical, however both are propagating at velocities slightly lower than the diamagnetic velocity.

4.2 Statistical analysis of turbulent fluxes

In order to quantify more precisely the relation between heat and momentum transport, we perform a statistical analysis of these fluxes in the turbulent steady-state. As a first step, we can compute the two-dimensional – in radius and time – cross-correlation function of the

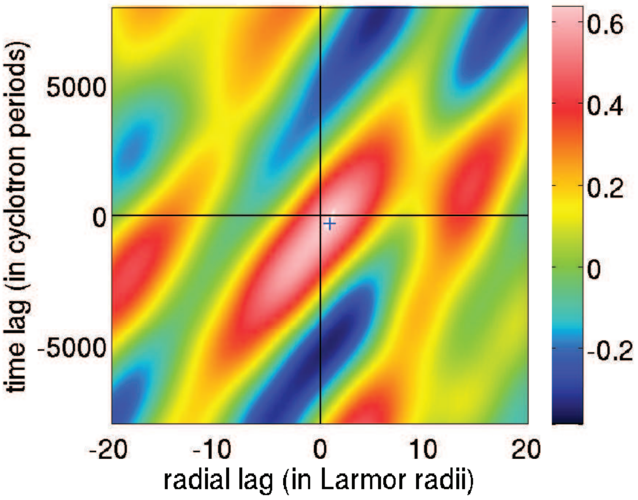

Figure 4.5: Two dimensional (in radius and time) cross-correlation function of turbulent heat flux and toroidal Reynolds stress

two fluxes, as shown in Fig. 4.5, where the momentum flux is represented by its dominant contribution, i.e. the turbulent Reynolds stress[3]. The key result that can be extracted from this figure is the maximum value of the cross-correlation, roughly 0.65, suggesting a strong correlation. This value is found to vary depending on the position where the analysis is performed and on the parameters of the simulation, but is systematically in the range from 0.5 to 0.8. This result, along with the elongated elliptical structures observed in the cross-correlations, confirm that the same avalanches transport both heat and momentum, as observed in Fig. 4.4. These observations have been compared with results from the gyrokinetic particle-in-cell code XGC1p [KCD09], showing good statistical agreement between the two codes [KAD+12].

The next step in the statistical analysis of the heat and momentum fluxes is to study their probability distribution functions (PDF). We compute the PDFs of the flux-surface averaged fluxes for a radial domain around mid-radius, after turbulence has reached a statistical steady-state in the simulation. Given the resolution of the simulation, the radial and temporal domain considered lead to roughly 75 000 points for the PDFs. Because the time average of the heat flux can vary slightly at different radial positions, we consider the PDF of $Q - \langle Q \rangle$ where $\langle Q \rangle$ is the time-averaged heat flux at a given radial position. The PDF of the heat flux, Fig. 4.6a, is clearly non-Gaussian, as it is strongly asymmetric and displays a heavy tail for large values of the flux. Note that if the heat flux is interpreted as the cross-correlation of two fluctuating fields with Gaussian statistics, one expects to find a non-Gaussian PDF for the flux [CHS+96], with detailed characteristics depending on the strength and sign of the correlation between the two fields. We perform the same statistical analysis for the turbulent Reynolds stress in Fig. 4.6b. The resulting PDF exhibits the same characteristic, with a strong asymmetry and a heavy tail for large values of the Reynolds stress. The PDFs of heat flux and Reynolds stress can be compared directly on a single plot by normalizing them to their respective mean values and standard deviations,

---

[3] In the following, only the off-diagonal ($\varphi\chi$) component of the Reynolds stress (Π_φ^χ in the notations of section 3.1.3) is considered as it is responsible for the radial transport of *toroidal* momentum.

as shown in Fig. 4.6c. Thus normalized, the two PDFs are remarkably similar, in particular in terms of the tails at large values of the fluxes. Finally, the asymmetry and intermittency observed in the PDFs can be quantified by computing the third and fourth moments of the distributions. The normalized third central moment, or *skewness*, measures the asymmetry of a distribution, and is defined for a given distribution f as

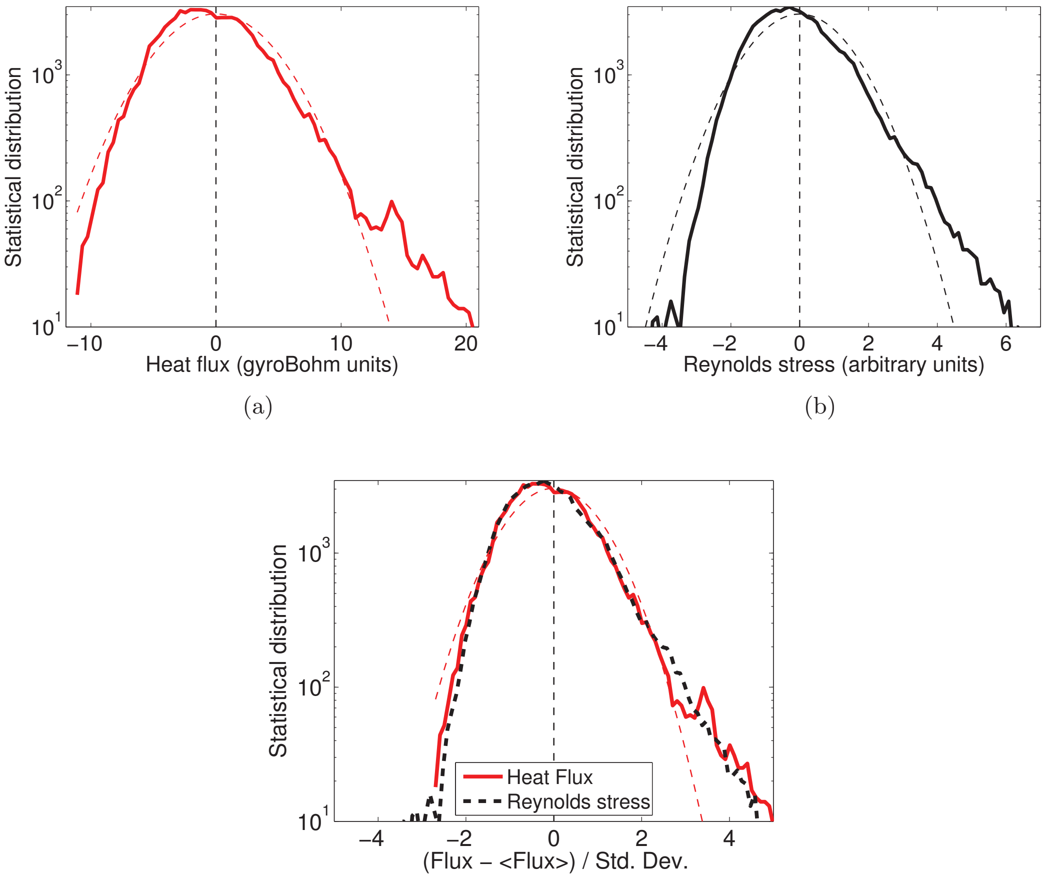

(a) (b)

(c)

Figure 4.6: Statistical distribution functions of the turbulent (a) heat flux and (b) Reynolds stress, around mid-radius r/a = 0.5. In both cases, a Gaussian fit is also plotted as a reference. (c) Both distributions are then normalized to their mean value and standard deviation for direct comparison.

$$Sk(f) = \frac{\langle (f-\bar{f})^3 \rangle}{\langle (f-\bar{f})^2 \rangle^{3/2}} \tag{4.2}$$

where $\bar{f} = \langle f \rangle$ is the mean value of f. The skewness of a Gaussian distribution – or any other symmetric distribution – is exactly zero, while positive skewness indicates a longer tail to the right of the mean value. For the PDFs in Fig. 4.6, we find a skewness of approximately 0.79 for both fluxes. The normalized fourth central moment, or *kurtosis*, measures the weight of the tails in the distribution. Kurtosis (sometimes referred to as

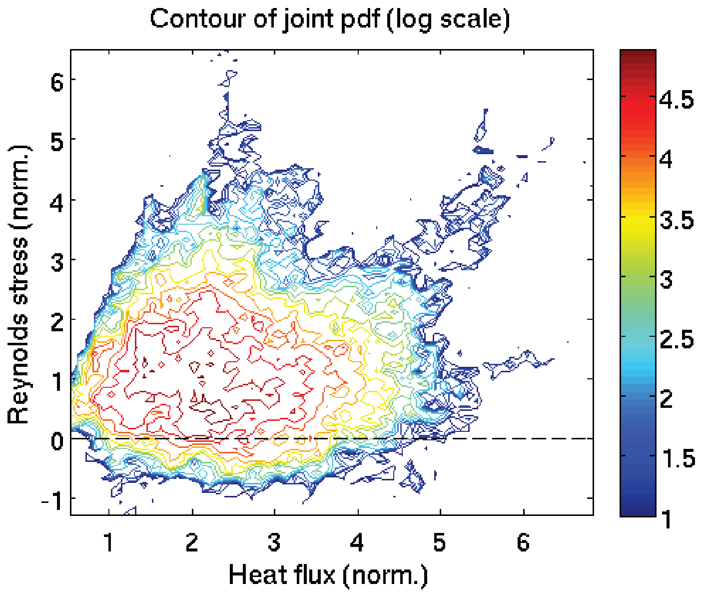

Figure 4.7: Logarithmic contour of the joint statistical distribution of turbulent heat flux and Reynolds stress. Both fluxes are normalized to their respective standard deviations.

excess kurtosis) is defined as

$$Ku(f) = \frac{\langle (f - \bar{f})^4 \rangle}{\langle (f - \bar{f})^2 \rangle^2} - 3 \tag{4.3}$$

so that the kurtosis of a Gaussian distribution is exactly zero. A positive kurtosis is indicative of flat distributions, i.e. with heavy tails. We obtain values of roughly 1.7 for the heat flux and 1.5 for the Reynolds stress, clearly departing from a Gaussian in both cases. Note that the fluxes used for the analysis are flux-surface averaged, and the intermittency would be more pronounced for the truly local (poloidally and toroidally) fluxes, as observed experimentally [NII$^+$11].

A useful tool when analyzing the correlation between two turbulent fluxes Γ_1 and Γ_2 is the technique of *joint PDF*, which represents the statistical distribution of the variable (Γ_1, Γ_2). Obviously, this technique requires larger datasets than standard PDFs, as the variable becomes two dimensional. Nevertheless, the 75 000 points previously used are sufficient to obtain a well-resolved joint PDF of turbulent heat flux and Reynolds stress, as shown in Fig. 4.7. A significant number of events with both large turbulent Reynolds stress and heat flux is clearly identified, which can be associated with the large-scale avalanches presented in section 4.1.2. Finally, a striking feature of the joint PDF is the two lines which can be drawn from the origin of the figure, one corresponding to the minimum value of the Reynolds stress and another for growing heat flux and Reynolds stress. These lines are reminiscent of the cycle observed during the initial front propagation of the simulation (Fig. 4.2b), suggesting that the mechanism associated with this initial front and the generation of a dipolar toroidal rotation profile is also at work during the statistical steady-state of the simulation.

As a final result in the statistical analysis of the turbulent fluxes, we present a striking observation of the difference between the dynamics of the Reynolds stress and of the time evolution of toroidal momentum. Although the latter is governed by the divergence of the

Reynolds stress, a statistical analysis by means of PDFs reveals that they exhibit very different dynamics. The PDF of $\partial_t \mathcal{L}_\varphi$ is shown in Fig. 4.8a, and is then normalized to its mean value and standard deviation for comparison with the turbulent Reynolds stress in Fig. 4.8b. We recall that, although momentum transport contains several terms as detailed in section 3.1.3, Eq. (3.23), the dominant term is the divergence of the turbulent toroidal Reynolds stress. The PDF for $\partial_t \mathcal{L}_\varphi$ is quite different from the PDF of the Reynolds stress obtained in Fig. 4.6b. The tails of the PDF, while still present, appear less important, as characterized by the kurtosis of the distribution of approximately 0.46, to be compared with 1.5 for the Reynolds stress. Also the PDF of $\partial_t \mathcal{L}_\varphi$ is much more symmetric, with a skewness of approximately 0.1, which is only marginally larger than the expected precision considering the number of points in the distribution. We recall that the PDFs of heat flux and Reynolds stress had a skewness of approximately 0.79.

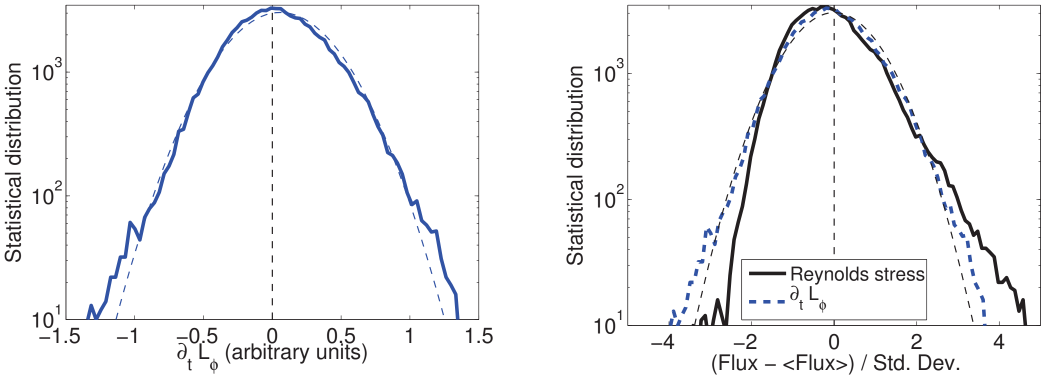

(a)

(b)

Figure 4.8: (a) Statistical distribution functions of the time derivative of the toroidal angular momentum ($\partial_t \mathcal{L}_\varphi$), around mid-radius r/a = 0.5, with a Gaussian fit is also plotted as a reference. (c) The distribution is normalized to its mean value and standard deviation for direct comparison with the distribution of the turbulent Reynolds stress.

This result, with a PDF for $\partial_t \mathcal{L}_\varphi$ closer to a Gaussian than the PDF of the Reynolds stress, highlights the fact that the turbulent Reynolds stress and its divergence exhibit significantly different dynamics. A possible interpretation of this observation is that the events of largest Reynolds stress, for instance corresponding to the large-scale avalanches observed in section 4.1.2, are also characterized by a larger radial extent, leading to less significant intermittency in the divergence of the Reynolds stress than in the Reynolds stress itself.

4.3 Possible mechanisms for intrinsic rotation

As evident from the derivation of the equation for local conservation of toroidal momentum, momentum transport, and therefore the generation of intrinsic rotation, requires a breaking of the symmetry along the magnetic field lines [PAA05]. Several mechanisms have been put forward to explain how ITG turbulence can perform this symmetry breaking, including radial electric field shear [GDHS07], the Coriolis effect [HDGR07, PAS07] which acts as a momentum pinch in a toroidally rotating plasma, polarization drift [MDGH09b, MDGH09a], up-down asymmetry of the magnetic equilibrium [CPA+09, CBD+10], turbulence intensity gradient [GDH+10], profile shearing [CIJP11, WSS11] and density gradient at finite ρ_* [SSK+12]. We focus here on two mechanisms expected to dominate in electrostatic ITG turbulence when the equilibrium magnetic field is up-down symmetric, namely electric field shear and turbulence intensity gradient.

Historically, the radial electric field has been identified as a key player in turbulent momentum flux [DS93, D+94, GSG+02]. Recent theoretical work [GDHS07] demonstrated that radial electric field shear, by generating sheared poloidal $E \times B$ flows, could break the symmetry in the parallel wave number (i.e. $k_\parallel$) spectrum, thus generating intrinsic rotation via the turbulent Reynolds tress. This effect was then observed in nonlinear gyrokinetic simulations [CPC+09, WHE+09]. Similarly, both theoretical work [DMG+08, GDH+10] and numerical simulations [KYR+12] found that a gradient in turbulence intensity can lead to breaking of the $k_\parallel$ symmetry, and therefore to intrinsic toroidal rotation. For both mechanisms, the process can be understood as that of an engine, converting the free energy stored in the mean gradients of the system into mean toroidal flows [KDG10].

In order to investigate the role of the different possible symmetry breaking mechanisms, we consider in Fig. 4.9a the correlations with the Reynolds stress of the radial electric field shear, expressed in terms of shear $E \times B$ flow, and turbulence intensity gradient. The turbulence intensity I is defined as

$$I(r) = \frac{1}{(2\pi)^2} \int \mathrm{d}\theta \mathrm{d}\varphi \left(\phi - \langle \phi \rangle_{F.S.}\right)^2$$

where $\langle \phi \rangle_{F.S.}$ is the flux-surface averaged electric potential. Since the momentum transport is actually controlled by the *divergence* of the Reynolds stress, we also show its correlation with the symmetry breakers in Fig. 4.9b. We focus only on the magnitude (i.e., the strength) of the correlation, regardless of whether it corresponds to positive or negative correlation. The results were obtained from a simulation with normalized gyroradius $\rho_* = 1/256$, over several $10^4 \omega_c^{-1}$. The other parameters are similar to those described in detail in section 2.4.

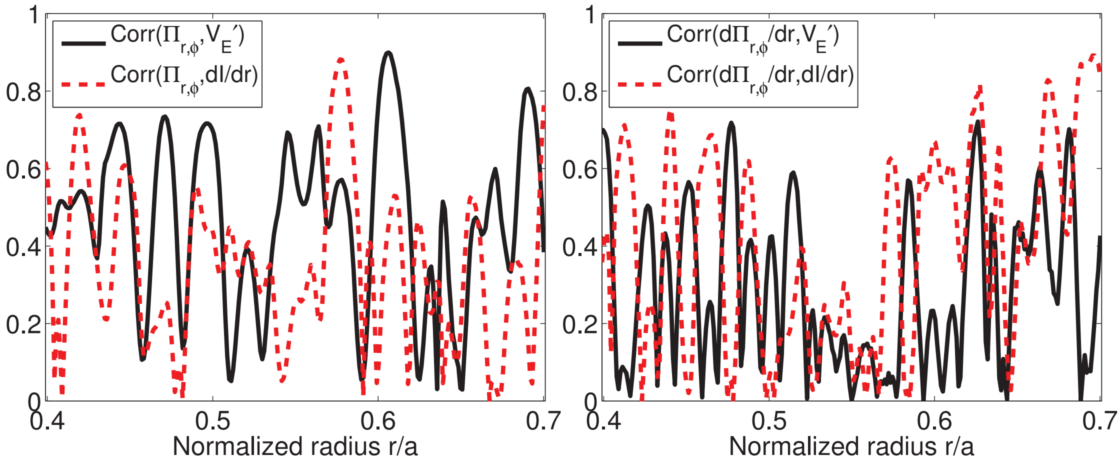

(a)

(b)

Figure 4.9: Radial profile of the correlations between the symmetry breaking mechanisms ($E \times B$ flow shear V_E' and turbulence intensity gradient dI/dr) and (a) the Reynolds stress; (b) the divergence of the Reynolds stress.

Both for the Reynolds stress and its divergence, values of the correlation above 0.5 are obtained at various radial positions, both with radial electric field shear and turbulence intensity gradient. This suggests that both proposed mechanisms can act as *local* symmetry breakers driving toroidal rotation. However, the present results are inconclusive as to the relative importance of the mechanisms considered here. Indeed, in global full-f gyrokinetic simulations, both effects are necessarily present and therefore difficult to isolate. Similar results have been obtained with the XGC1p [KAD+12] and gKPSP [KYR+12] gyrokinetic codes.

4.4 Summary

In this chapter, electrostatic micro-turbulence was considered as a means of breaking the axisymmetry in tokamaks, which was identified in chapter 3 as a necessary condition for the generation of toroidal rotation. In a simulation with a vanishing initial rotation profile, turbulence was found to generate intrinsic rotation. This rotation initially exhibits a dipolar profile, eventually the no-slip boundary conditions lead to the generation of *net* toroidal rotation. Large-scale avalanches are observed in the simulations, which are found to transport both heat and momentum. A detailed analysis during the statistical steady-state of the simulation reveals that the turbulent heat flux and Reynolds stress are strongly correlated, and characterized by very similar statistical dynamics. In both cases, the statistical distribution of the fluxes exhibit non-Gaussian properties. Finally, electric field shear and turbulence intensity gradient are identified as possible symmetry breaking mechanisms for the generation of toroidal rotation by electrostatic turbulence.

Chapter 5

Non-local properties of turbulent transport

Turbulent transport is often analyzed in terms of a purely local description, often assuming diffusive or diffusive-convective transport. In this chapter, we investigate non-local properties of turbulent transport, showing how the description of turbulence depends on the scales considered or, in other words, on the averages performed. The influence of boundary conditions on toroidal momentum transport also reveals the limitations of a local description of turbulent transport.

In chapters 3 and 4, as in most studies of turbulence in tokamak plasmas, the quantities considered were systematically flux-surface averaged. However, there is no reason to expect the avalanche dominated transport observed in section 4.1.2 to be homogeneous over a flux-surface, and in particular in the poloidal direction. In section 5.1, we describe the poloidal asymmetry of turbulent transport, and the impact of flux-surface averaging on the description of turbulence on tokamaks.

When trying to extrapolate present experimental observations to future devices, a convenient method is to estimate turbulent transport in terms of a diffusion coefficient, and consider the scaling of this coefficient with machine size, expressed in terms of normalized gyroradius ρ_*. In section 5.2, we review the main results regarding the ρ_* scaling of turbulent heat transport and extend it to momentum transport. In addition to flux-surface averaging, such a result requires averages over significant radial and temporal domains in the simulations, and does not retain the information on the large-scale intermittency of turbulent transport observed in the previous chapter.

For the case of momentum transport, another important non-local effect, the impact of boundary conditions on core rotation, is discussed in section 5.3. Because edge flows can vary significantly between different experiments and provide the only source of *net* intrinsic rotation in the core, their effect on core momentum transport must be carefully analyzed.

Finally, implications of the non-locality of turbulent heat and momentum transport in terms of transport modeling, where one seeks the simplest model to capture the basic properties of plasma confinement, are discussed in section 5.4.

5.1 Poloidal asymmetry of turbulent transport

Turbulent transport is often studied in terms of flux-surface averaged quantities, which was the framework adopted in the previous chapters. However, transport in tokamaks is known to be poloidally asymmetric. More precisely, turbulence is expected to be strongest in the low-field side (LFS) near $\theta = 0$, and very weak in the high-field side (HFS). This is due to the fact that interchange instabilities, such as the ITG mode studied in the present work, are unstable when the gradient of the magnetic field is aligned with the gradient driving the instability (in this case, the temperature gradient), which occurs on the low-field side, when both gradients are directed towards the core of the plasma. Indeed, such modes are locally stable in the high-field side region, where the magnetic field gradient points outward. This poloidal asymmetry is referred to as the *ballooning* structure of turbulence in toroidal devices, and has been observed experimentally, for example in Tore Supra [GBD+07, FGG+09] and Alcator C-MOD [LRH+04, SLP05]. In this section, we present detailed observations of turbulence ballooning in gyrokinetic simulations, and analyze the impact of flux-surface averaging on the measured intermittency of turbulent heat and momentum fluxes.

We consider here poloidally local fluxes, rather than the flux-surface averaged fluxes described in previous sections. The poloidal anisotropy of turbulent fluxes has previously been analyzed in fluid edge simulations of particle transport [TGT+09], and very similar results are obtained here in the case of a gyrokinetic simulation of core turbulent heat transport, with the parameters described in section 2.4. Comparing results from heat transport and particle transport is justified as both are a consequence of the convection of the distribution function by the $E \times B$ velocity. Particle transport is not included in the model used by GYSELA at the moment as electron response is assumed adiabatic, but one expects similar properties for heat and particle fluxes resulting from core ITG turbulence.

As a first observation, the minimum and maximum value of the heat flux on a given flux-surface are plotted as a function of radius in Fig. 5.1a, and compared with the mean (i.e., flux-surface averaged) quantity. One notices that the minimum value of the heat flux, which corresponds to positions near $\theta = \pi$, remains much smaller than the mean flux, and is in fact locally negative. Conversely, local maxima of the heat flux can be significantly greater than flux-surface averaged quantities. The large values of minimum and maximum

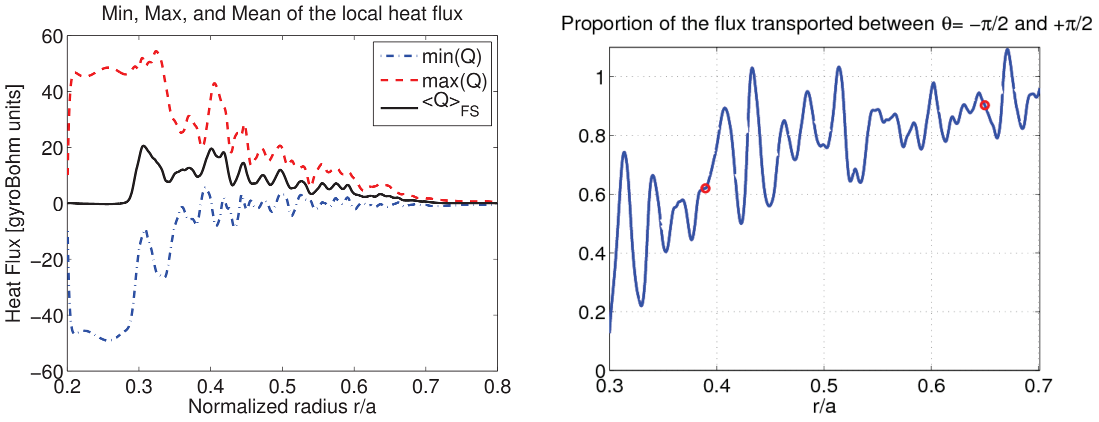
Min, Max, and Mean of the local heat flux

Proportion of the flux transported between θ= −π/2 and +π/2

(a)

(b)

Figure 5.1: Characterization of the ballooning of turbulent heat transport: (a) Radial profile of the maximum, minimum and mean value of the local (in θ) radial heat flux ; (b) Proportion of the heat flux transported between $\theta = -\pi/2$ and $\theta = +\pi/2$, as a function of the radius. The blue circles correspond to the radial positions considered in Fig. 5.2.

heat flux close to the inner radial boundary, where the mean flux is vanishing, appears to be a consequence of the properties of the heat source, which in this simulation injected mainly parallel energy. It has been shown that anisotropic heating such as this leads to the generation of a poloidal electric field [Tag93], which is indeed observed in the present simulation and corresponds to the large variations of the heat flux in the region of the source.

In Fig. 5.1b, the proportion of the flux transported between $-\pi/2$ and $+\pi/2$, i.e. on the low-field side, is given as a function of the radius. Throughout most of the radial domain, and especially far from the heat source, it appears that a large majority of the heat flux ($> 60\%$) is transported on the LFS. For $r/a \gtrsim 0.55$, this figure is above 80%. This is consistent with the poloidal distribution of the radial flux inferred from experiments on Tore Supra [FGG+11].

A more precise characterization of the poloidal structure of the heat flux can be obtained by considering the proportion of the radial heat flux transported in various poloidal sections of the torus, at a fixed radial location. As the flux is roughly symmetric around $\theta = 0$, one can consider sections between $-\theta$ and $+\theta$ for $\theta \in [0; \pi]$. The result is shown in Fig. 5.2 for two typical radial positions, one close to the heat source and another closer to the edge of the simulation domain. The results obtained are very similar to previous observations in fluid edge simulations [Tam07]. An important feature highlighted in both Fig. 5.1b and Fig. 5.2 is that the ballooning of turbulent transport appears to increase with the minor radius. Thus, one can expect a strongly ballooned source at the separatrix, which is consistent with experimental results on Tore Supra [FGG+11].

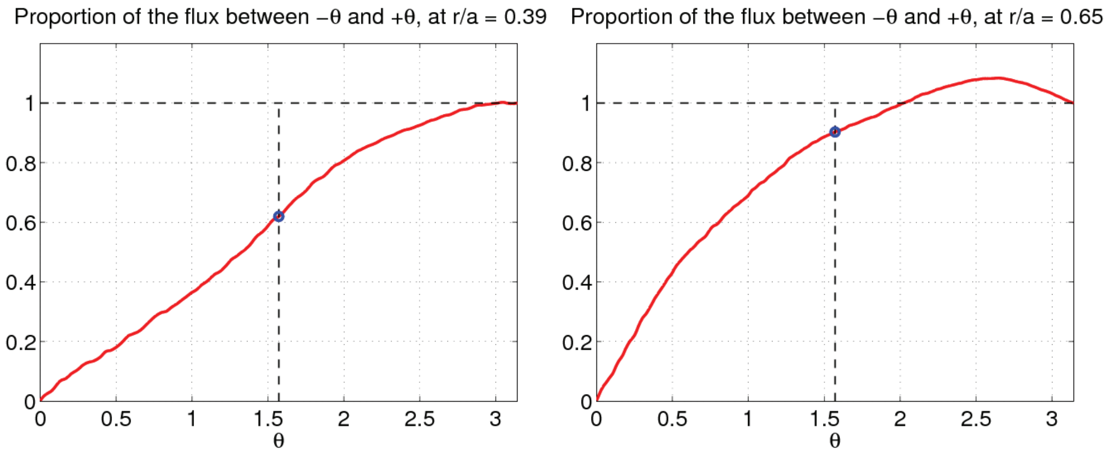

(a) (b)

Figure 5.2: Proportion of the heat flux transported between $-\theta$ and $+\theta$ for two different values of the radius, identified by red circles in Fig. 5.1b.

5.2 Gyro-Bohm scaling of turbulent heat and momentum transport

In terms of a purely local description of turbulent transport in tokamaks, an important issue is the scaling of the transport coefficients with machine size, which is important in order to extrapolate present experimental results to future machines. More precisely, this issue is usually addressed through the scaling with the dimensionless parameter ρ_*, which corresponds to the ion thermal gyroradius ρ_s normalized to the tokamak minor radius a.

In order to estimate the scaling of turbulent transport with machine size, one can begin by describing turbulence simply as a random walk process. With this very simple description, heat transport is completely described by a diffusion coefficient χ_i such that the heat flux is $Q = -\chi_i \nabla T$. The diffusivity is generally normalized to the so-called Bohm diffusion, $\chi_B = T/eB$.

From a theoretical point of view, one can estimate the heat flux simply from a dimensional analysis as

$$\chi_i \sim \frac{\lambda_c^2}{\tau_c} \tag{5.1}$$

where λ_c and τ_c are the correlation length and time of the turbulence. Clearly, this description of turbulence is very crude and must be dealt with accordingly. Importantly, an implicit assumption is for the turbulence to develop on scales much larger than its correlation length. Moreover, the description of heat transport as a simple random walk process treats temperature as a passive tracer in a turbulence field, whereas the actual transport results from a complex interplay between temperature gradients and fluxes. Keeping these important limitations in mind, one can still use the basic expression (5.1) to obtain a rough estimate of turbulent transport by measuring or estimating the correlation length and time.

Measurements of ion heat diffusivity in experiments have found either Bohm scaling, $\chi_i \sim \chi_B$, or the so-called *gyro-Bohm* scaling, $\chi_i \sim \rho_* \chi_B$. The latter result, which is more favorable when extrapolating to larger future devices, was mainly observed in improved confinement regimes [PLB+95]. Such results were obtained by measuring the mean gradients and fluxes, as detailed measurements of turbulence characteristics were not available. More recently, efforts have been made to measure the local fluctuations, in order to obtain scaling laws for correlation length and time. These studies, reviewed in [Hen06], obtained results consistent with a gyro-Bohm scaling:

- the correlation length scales with the ion Larmor radius,
- the correlation time scales with the transit time a/c_s
- which, according to Eq. (5.1), leads to $\chi_i \sim \rho_i^2 a/c_s = \rho_* \chi_B$.

These local measurements are consistent with predictions from fluid simulations (see for example [OBC+97]).

The first results from gyrokinetic simulations [LEHT02, WCR02] found a transition from Bohm scaling to gyro-Bohm scaling for decreasing ρ_*. A simple understanding of these results is that the gyro-Bohm prediction based on correlation time and length assumes a scale separation between the turbulent scales and the machine size. In fact, the assumptions leading to the estimate Eq. (5.1) basically correspond to the limit $\rho_* \to 0$. Thus, if the machine size – or simulation domain – is small, the turbulence may feel the size of the system, leading to Bohm (or worse) scaling.

For the specific case of ion heat transport, a major effort was undertaken recently to review the scaling with respect to ρ_* using global gyrokinetic simulations. Despite large fluctuations in both the temperature gradient and the heat flux in such simulations, a mean value of the diffusivity can be obtained by averaging over a large radial domain as well as over a significant time frame during the statistical steady-state of the simulation. These studies [MLB+10, VBB+10, SGA+11], using several different gyrokinetic codes, identified a transition from Bohm to gyro-Bohm scaling for $\rho_* \sim 1/300$, possibly linked to the dynamics of avalanches and zonal flows [SGA+11].

While the scaling of density and heat transport with ρ_* has been extensively studied, both experimentally and numerically, very little work has been done regarding the scaling of momentum transport. However, this issue is important if one is to predict the level of rotation in future tokamaks by extrapolating results from smaller, existing machines. Assuming gyro-Bohm characteristics for turbulence, symmetry arguments [PAA05] provide a prediction for the level of momentum transport from the Reynolds stress. The following scalings are expected for the Reynolds stress and its divergence:

$$\begin{aligned} \frac{\Pi_\varphi^\chi}{R v_T^2} &\propto \rho_*^2 \\ \frac{\partial_\chi \Pi_\varphi^\chi}{R v_T^2/a} &\propto \rho_* \end{aligned}$$

Several simulations were performed with the GYSELA code at various values of ρ_*, with all other parameters kept constant, in order to investigate the scaling of both heat and momentum transport. For heat transport, the mean diffusivity was estimated in these simulations, confirming the transition from Bohm to gyro-Bohm at small ρ_* [SGA+11]. Locally, the correlation time and length of turbulence corresponded to the gyro-Bohm ordering, i.e. $\lambda_c \sim \rho_i$ and $\tau_c \sim a/c_s$.

Because the turbulent Reynolds stress exhibits large variations radially and in time (see Fig. 3.2b), around a vanishing mean value, the scaling with ρ_* can be investigated by focusing on the fluctuations. Therefore, we consider the scaling with ρ_* of the root mean square (RMS) fluctuations of the divergence of the Reynolds stress, normalized to $mnR_0 v_T^2/a$, where m and n are the species mass and density, R_0 is the major radius at the magnetic axis, v_T is the thermal velocity and a is the minor radius. This choice of normalization is independent of ρ_* as the simulations are performed by varying only the tokamak size with all the other parameters constant, in particular the aspect ratio, i.e. R_0/a, remains the same. The temperature, density and magnetic field also remain constant between the simulations. One finds a roughly linear scaling [AGG+11], approximately $\rho_*^{0.7}$, as shown in Fig. 5.3. This result appears to indicate that the scaling of

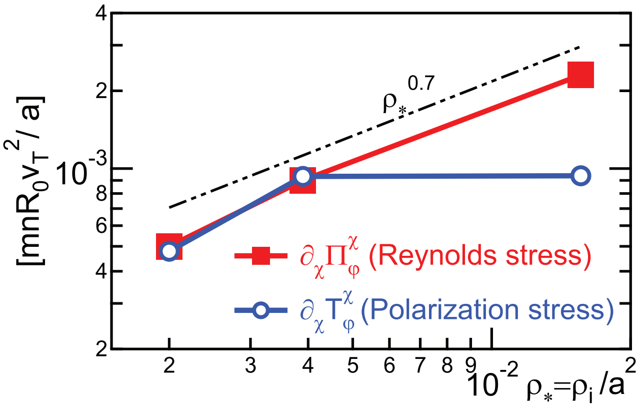

Figure 5.3: Scaling against ρ_* of the RMS fluctuations of the divergence of the Reynolds and polarization stresses. A logarithmic fit for the divergence of the Reynolds stress yields $\partial_\chi \Pi_\varphi^\chi \propto \rho_*^{0.7}$ (normalized to $mnR_0 v_T^2/a$)

momentum transport is gyro-Bohm, or slightly worse than gyro-Bohm. However, more data would be required, in particular using different gyrokinetic codes as in the study of heat transport, in order to confirm this result. In the different simulations considered, the characteristic spatial scale of the Reynolds stress remains roughly constant, of the order of several Larmor radii. Therefore, normalized to $mnR_0v_T^2$, the Reynolds stress scales roughly quadratically with ρ_*. We also note that the divergence of the polarization stress identified in section 3.1.3 is small at moderate values of ρ_*, but is of the same order as the divergence of the Reynolds stress at smaller values of ρ_* relevant for ITER.

One may regard the scalings obtained here as contradicting the observations of large-scale events in the dynamics of turbulent transport in chapter 4. Indeed, the predictions of a gyro-Bohm scaling, as recovered in the simulations, assume that turbulence remains purely local with a correlation length of the order of the Larmor radius. In fact, the auto-correlation function of the electric potential fluctuations in gyrokinetic simulations reveals that, despite the large-scale avalanches, the correlation length is of the order of several Larmor radii and is independent of the system size [SGA$^+$11][1]. This apparent contradiction could be explained by the existence of an intermediate scale between the Larmor radius and the system size, limiting the radial extent of the avalanches, as explored in [DPDG$^+$10]. As Bohm scaling is expected when the correlation length scales with ρ_*, this additional *meso-scale*, larger than the Larmor radius but scaling with ρ_i independently of the system size, could explain why turbulent heat and momentum transport, despite being dominated by avalanches, exhibit gyro-Bohm scaling.

5.3 Influence of scrape-off layer flows on core rotation

Throughout the manuscript, the role of boundary conditions in gyrokinetic simulations of momentum transport has emerged, at least implicitly, as a critical issue. Since a local conservation law for toroidal momentum is verified by the gyrokinetic model (chapter 3), the only *net* generation of toroidal rotation observed in the simulations must be linked to boundary conditions. We recall that *no-slip* conditions (i.e. vanishing rotation) were imposed at the outer radial boundary, with an *ad hoc* diffusion ensuring exchange of momentum between the plasma and the edge of the simulation domain. This modeling choice, although it should not presumably affect the statistical dynamics of turbulent momentum transport as described in chapter 4, may have an impact on the toroidal rotation profiles eventually reached by the simulations.

Most gyrokinetic simulations, including those described in the present manuscript, have assumed such boundary conditions – or alternatively a vanishing momentum flux at the edge – without evaluating their impact on the observed rotation profiles. One of the difficulties is that the role of the edge plasma with respect to rotation in the core is not well understood, as core and edge toroidal rotation have often been studied independently. There is experimental evidence that flows from the scrape-off layer (SOL) of the plasma may influence toroidal rotation in the outer core [LRH$^+$04, GBD$^+$07, HVF$^+$10], but this effect has yet to be confirmed by core turbulence simulations. Of course, using the edge as a boundary condition for the core constitutes a simplified view of the complex coupling between edge and core physics. In particular, the ballooning of turbulent transport described in section 5.1 is expected to significantly affect flows in the SOL .

---

[1] Note that, as can be expected from the ballooning of turbulence discussed in section 5.1, the correlation length is not poloidally homogeneous, and was found to vary by a factor of two from the LFS to the HFS of the tokamak [SGA$^+$11].

In the following, we investigate the effect on core toroidal rotation of modified boundary conditions in Gysela simulations. The basic theory of parallel scrape-off layer flows is recalled in section 5.3.1, and Gysela simulations are presented in section 5.3.2 with boundary conditions based on standard SOL flows. Note that the important issue of *how* the core plasma is coupled to the edge of the simulation domain (i.e. the diffusion in the buffer regions) and how details of this coupling may affect the resulting rotation profiles is not addressed here and would benefit from further investigation.

5.3.1 Simple model for scrape-off layer flows in tokamaks

In this section, we present a basic description of parallel flows in tokamak scrape-off layers, as described in more detail in standard textbooks [Sta00]. The most simple physics in the SOL can be described by a one-dimensional model for the evolution of ion density n and parallel flow $\Gamma = nu_\parallel$, assuming constant temperature, with the following equations

$$\begin{aligned} \partial_t n + \nabla_\parallel \Gamma &= S && (5.2a) \\ m_i \partial_t \Gamma + \nabla_\parallel \Pi &= 0 && (5.2b) \end{aligned}$$

where S is the particle source and Π is the total pressure, which can be expressed as $\Pi = p_e + p_i + m_i n u_\parallel^2$ where p_e and p_i are the electron and ion pressure. For simplicity, we do not consider any source of momentum. Note that here the parallel direction is along the magnetic field lines, which are open in the scrape-off layer. Considering only the steady-state solution, the system of equations (5.2) becomes simply $\nabla_\parallel \Gamma = S$ and $\nabla_\parallel \Pi = 0$. A convenient way of rewriting these equations is to consider the parallel Mach number, $M \equiv \Gamma/(nc_s)$, where $c_s = [(T_e + T_i)/m]^{1/2}$ is the isothermal ion acoustic speed. Combining both equations leads to

$$\nabla_\parallel M = \frac{S}{nc_s} \frac{1+M^2}{1-M^2} \tag{5.3}$$

In order to obtain the Mach number profile, one must describe the scrape-off layer in more detail. We consider here the case of a simple SOL in limiter geometry with a homogeneous particle source. Assuming the usual Bohm boundary conditions $M^2 = 1$ at both sides of the limiter, one obtains analytically the (solid blue) profile of Mach number shown in Fig. 5.4a. Notice that the Mach number goes to -1 and $+1$ at both ends, which correspond to the two sides of the limiter, with infinite derivatives along the magnetic field line. This basic profile can be modified when taking into account the asymmetry of the particle source or a different geometry. As an example, an output from the fluid code SOLEDGE-2D [ICC+10] in the case of a strongly ballooned source is given in Fig. 5.4a.

The next step is to estimate the resulting parallel velocity profile in the closed field-line region. An approximate result can be obtained by considering a *stationary* two-dimensional diffusive model for density n and parallel flow Γ in the closed-field line region near the last closed magnetic flux surface (LCFS). This simple model reads

$$\begin{aligned} -D\Delta_\perp n + \nabla_\parallel \Gamma &= 0 && (5.4a) \\ -m_i \nu \Delta_\perp \Gamma + \nabla_\parallel \Pi &= 0 && (5.4b) \end{aligned}$$

where D and ν are diffusion coefficients describing radial transport. In the limit where $M^2 \to 0$ (i.e. low flow) and in the isothermal approximation, $\nabla_\parallel \Pi = T \nabla_\parallel n$. Thus the system of equations (5.4) reduces to an equation for the parallel flow

$$\nabla_\parallel^2 \Gamma = \frac{D\nu}{c_s^2} \Delta_\perp^2 \Gamma \tag{5.5}$$

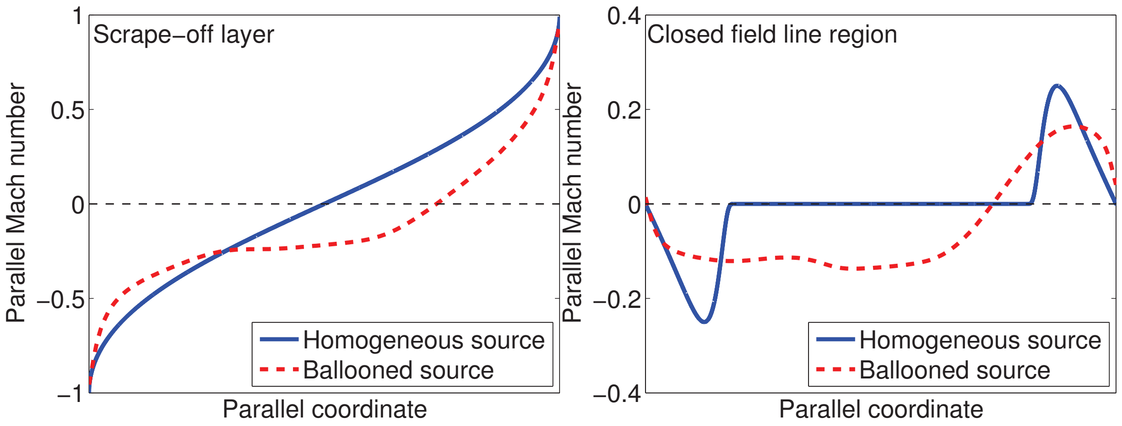

(a) (b)

Figure 5.4: Simple profiles for the parallel Mach number along the magnetic field line in (a) the scrape-off layer (open magnetic field lines) and (b) in the region of closed field lines near the last closed flux surface. The solid blue lines correspond to analytical profiles in the case of a symmetric source, while the dashed red lines are outputs from SOLEDGE-2D simulations with a strongly ballooned source.

In Fourier space, this reads

$$-k_{\parallel}^2 = \frac{D\nu}{c_s^2} k_{\perp}^4 \tag{5.6}$$

Although this precise result is dependent on the choice of reduced model made here, we can expect the profiles obtained in the open field line region (Fig. 5.4a) to be damped inside the LCFS, with the small $k_{\parallel}$ structures being damped more rapidly. In particular, the discontinuity between both sides of the limiter will not be observed inside the LCFS. Schematically, this leads to profiles such as Fig. 5.4b for the parallel Mach number. The solid blue line corresponds to the case of a symmetric source, while the dashed red line is the result of a SOLEDGE-2D simulation with a strongly ballooned source.

5.3.2 Modifying the boundary conditions in GYSELA

In the following, we explore the influence of scrape-off layer flows on core rotation by setting velocity profiles as boundary conditions in GYSELA, rather than the usual no-slip conditions. As a starting point, we consider a simulations at $\rho_* = 1/150$ and $\nu^* = 0.02$ which was run with conventional no-slip boundary conditions for approximately $3.10^5\,\omega_c^{-1}$. Given the input power and the pressure profile, this time is comparable to the confinement time, and the plasma appears to have reached a steady-state for the mean flows, as shown in Fig. 5.5a.

Limiter-like boundary conditions

From this steady-state, we impose as a boundary condition for parallel velocity a poloidally symmetric profile as shown in Fig. 5.4b, with the poloidal position corresponding to the limiter at $\theta = 0$. The maximum absolute value of the edge velocity is $V_{th} = 0.25\,v_{th0}$,[2]

---

[2] We recall that v_{th0} is the thermal velocity corresponding to the temperature at the center of the simulation domain. Thus, the corresponding local Mach number is in fact slightly larger.

for $\theta = \pm\pi/4$. As a result, the profile is rapidly modified near the edge, as can be observed in Fig. 5.5b, and a new steady-state is reached by the flows in the simulation. Inside $r/a \simeq 0.75$, the profile does not appear to be affected by the modification of the boundary conditions, even on a long time scale. This has been confirmed by continuing the simulation with no-slip boundary conditions and comparing the obtained profiles: the difference between the two remains smaller than the level of fluctuation of the profiles around their mean steady-state values.

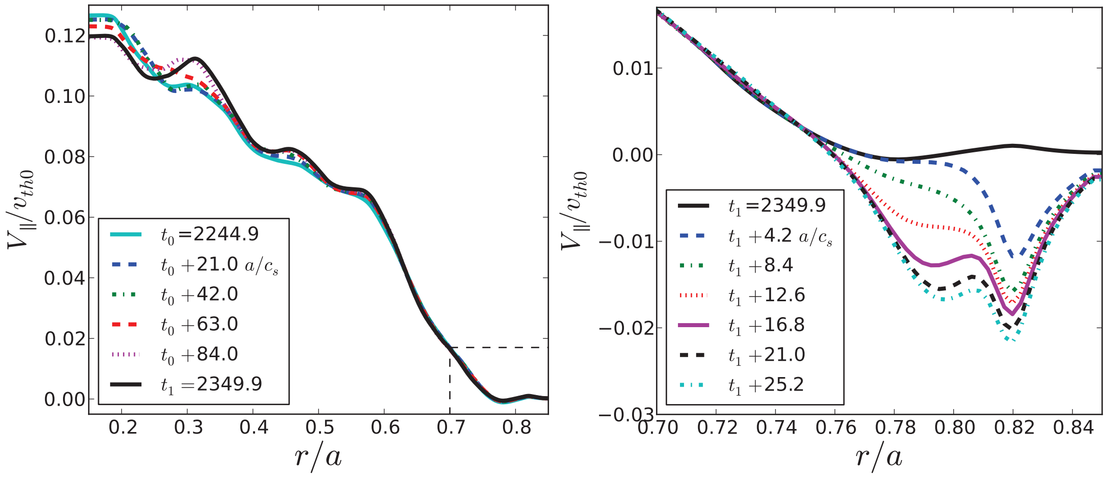

(a) (b)

Figure 5.5: Radial profiles of the parallel velocity at different simulation times (normalized to a/c_s) showing (a) the slow evolution around a mean profile in the steady-state regime (with $\Delta t = 21\,a/c_s$), and (b) the rapid modification of the profile (with $\Delta t = 4.2\,a/c_s$) near the edge after modifying the boundary condition for parallel velocity. The velocities are normalized to a reference (i.e., constant) thermal velocity.

Considering our choice of boundary condition, it is not sufficient to analyze its effect on the core plasma in terms of flux-surface averaged flows, which was the quantity of interest in the previous chapters. However, before we consider the effect of modified boundary conditions, it is useful to analyze the poloidal structure of the steady-state flows. Indeed, in the steady-state regime, the parallel velocity is *not* homogeneous in the poloidal direction, as can be observed in Fig. 5.6. Large variations of the velocity are present on a given flux-surface, essentially dominated by an $m = 1$ mode, which corresponds to Pfirsch-Schlüter rotation. Note that the amplitude of this variation is of the same order of magnitude – and in fact often larger – than the flux-surface averaged flow, and can lead to a reversal of the sign of the parallel flow on a given flux-surface (see the white $V_\parallel = 0$ contour in Fig. 5.6).

After the boundary conditions have been modified, the poloidal structure of parallel velocity is affected, but only in a small region between $r/a \simeq 0.75$ and the outer boundary of the simulation domain, $r/a = 0.85$. The resulting poloidal cross-section of the parallel velocity is shown in Fig. 5.7a. In order to highlight the result, the modification of the parallel velocity near the boundary, $\Delta V_\parallel = V_\parallel(\text{end}) - V_\parallel(\text{steady-state})$, is given in Fig. 5.7b. Interestingly, the effect on the poloidal structure is *not* localized near $\theta = 0$, where the boundary condition has been modified, but rather moves to the high-field side with decreasing minor radius.

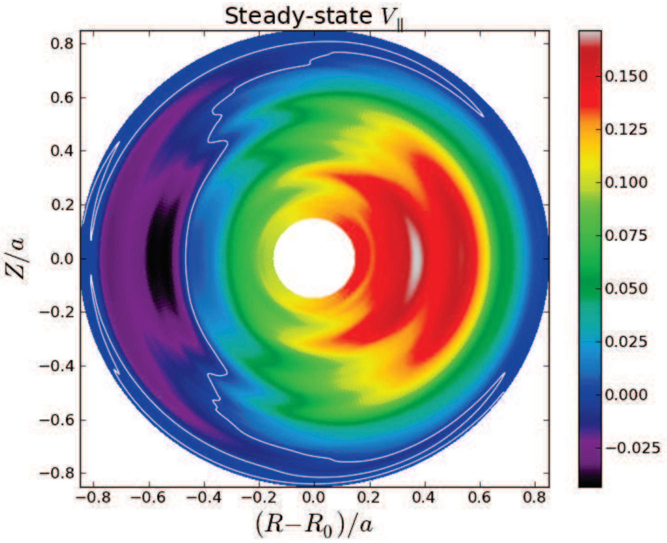

Figure 5.6: Poloidal cross-section (averaged over φ) of the parallel velocity – normalized to the thermal velocity – in the steady-state regime with no-slip boundary conditions. .The white line corresponds to the $V_\parallel = 0$ contour.

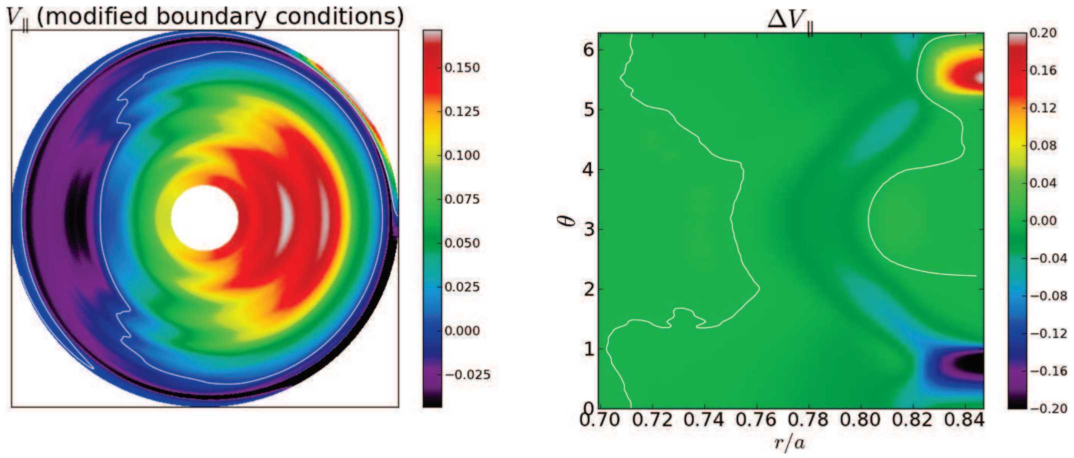

(a)

(b)

Figure 5.7: (a) Poloidal cross-section of the parallel velocity after modifying the boundary conditions (the white line corresponds to the $V_\parallel = 0$ contour) and (b) corresponding modification of the parallel velocity, i.e. $\Delta V_\parallel = V_\parallel(\text{end}) - V_\parallel(\text{steady-state})$, with a zoom near the outer radial boundary (the white lines correspond to $\Delta V_\parallel = 0$ contours).

In Fig. 5.8, we analyze the transition from the last point of the domain, where the boundary condition is imposed, to the core plasma, where the flows are not affected. First of all, in the region closest to the simulation edge, the radial diffusion term damps fluctuations and governs heat and momentum transport. We recall that this radial diffusion, of the form $\frac{1}{r}\partial_r \left\{D(r)\partial_r \bar{F}\right\}$, ensures the coupling of the plasma to the fixed temperature outside the domain and acts as a heat sink for the system in flux driven simulations. The radial profile of the diffusion term $D(r)$ is given in Fig. 5.8a, along with its effect on the poloidal structure of parallel velocity, represented by the radial profile at two fixed positions of θ corresponding to the minimum and maximum value of parallel velocity. The main observation is that the boundary condition is transported as expected by the diffusion coefficient, although an asymmetry appears between positive and negative parallel rotation. The cause for this asymmetry is not understood at the moment.

In Fig. 5.8b, we consider the effect of the velocity outside the buffer region by analyzing the poloidal profile at several radii. At $r/a = 0.825$, corresponding roughly to the limit of the buffer region, the parallel velocity still has the shape imposed at the boundary, but with an important asymmetry, as observed in Fig. 5.8a. Further inward, we clearly observe two lobes of negative parallel velocity moving toward the high-field side, corresponding to the structures observed in Fig. 5.7. Eventually, the initial $\cos\theta$ structure (see Fig. 5.6) is recovered for $r/a \lesssim 0.75$.

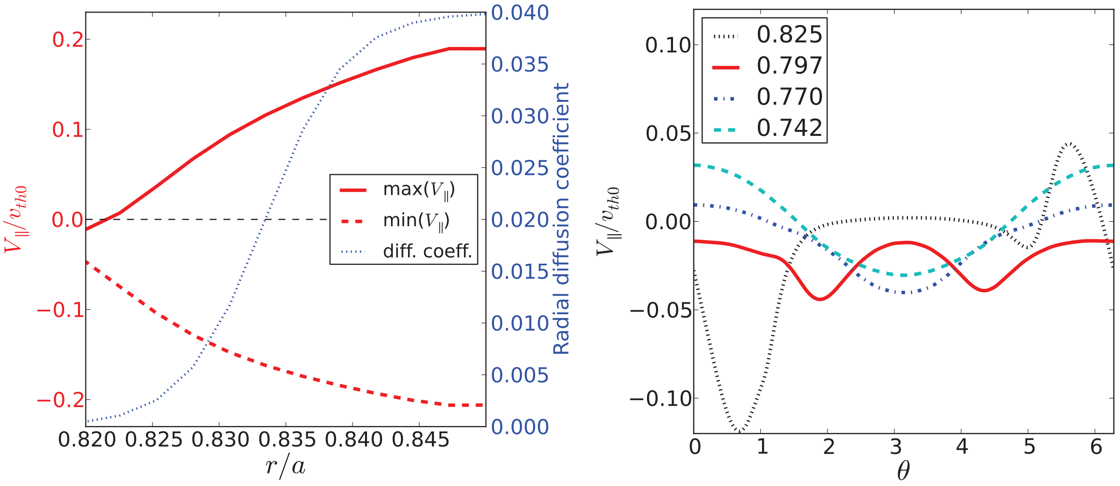

(a) (b)

Figure 5.8: (a) Maximum (solid red) and minimum (dashed red) of parallel velocity in the buffer region where radial diffusion is applied, the radial profile of the diffusion coefficient is given by the dotted blue line. (b) Poloidal profiles of the parallel velocity at different radii near the boundary of the simulation domain.

In order to understand both the asymmetry of the result obtained here in terms of positive and negative parallel velocity, an analogue simulation was run but with the opposite boundary condition: the maximum value $V_\parallel/v_{th0} = 0.25$ is now at $\theta = +\pi/4$, compared to $\theta = -\pi/4$ previously (see Fig. 5.4). In terms of the flux-surface averaged velocity, the effect is the opposite in the region near the edge, with the parallel velocity increasing on the same time scale and with roughly the same magnitude as the decrease observed in Fig. 5.5b.

Analyzing the propagation of the poloidal structure of the boundary conditions, one again finds an asymmetry in the buffer region and a propagation to the high-field side further inward, as highlighted in Fig. 5.9. However, the lobes propagating inward correspond to a positive velocity, the opposite sign as in the previous simulation. Thus it appears that their sign, and ultimately the flux-surface averaged parallel velocity, is determined by the value of the edge velocity for $\theta > 0$.

Note that in both cases, no measurable effect is observed inside $r/a \simeq 0.75$, suggesting that the impact of SOL flows on core rotation is limited to a narrow region near the edge.

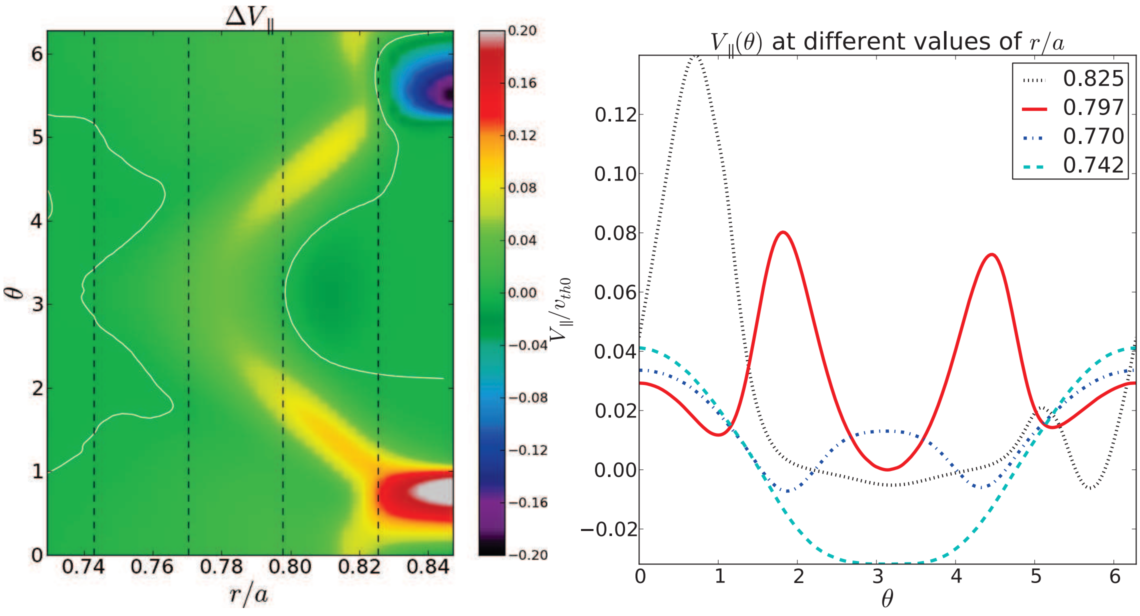

(a) (b)

Figure 5.9: Effect of a boundary condition with $V_\parallel/v_{th0} = 0.25$ at $\theta = +\pi/4$. (a) Modification of the poloidal structure of parallel velocity near the edge, and (b) poloidal profiles at several radii, indicated with dashed black lines in (a).

This key result does not appear to depend directly on the amplitude of the SOL flow, as a simulation with equivalent boundary profiles and $V_\parallel/v_{th0}$ doubled from 0.25 to 0.5 (at $\theta = +\pi/4$) leads to a comparable penetration in the core.

Pedestal-like boundary conditions

In the previous section, the boundary condition applied to the core plasma mimicked the structure of flows in the scrape-off layer, as they are observed experimentally in L-mode plasmas. When the plasma is in the so-called H-mode (see [ASD89] for a review) of improved confinement, a transport barrier develops near the plasma edge, modifying the coupling of the core plasma to the scrape-off layer. At the position of this barrier, also referred to as the *pedestal*, a strong shear is measured for the toroidal rotation, which increases in the core [RICd+07]. Consequently, in H-mode plasmas, the boundary condition for core toroidal rotation can be described by a uniform (or "solid") rotation of relatively large amplitude at the radial position of the pedestal.

Here, we investigate the effect of such boundary conditions on the plasma core, starting from the same reference simulation described previously ($\rho_* = 1/150$). Rather than an inhomogeneous poloidal profile, we set the boundary condition to a fixed non-vanishing value at the edge of the simulation domain, i.e. $r/a = 0.85$. Two simulations have been performed, with $V_\parallel(r/a = 0.85) = \pm 0.1 v_{th0}$, which is of the order of the pedestal velocities observed experimentally [RICd+07]. The resulting parallel velocity profiles are shown in Fig. 5.10 approximately $2.3\,10^5\,\omega_c^{-1}$ after the modification of the boundary condition, averaged over $5\,10^3 \omega_c^{-1}$. As a reference, the simulation with no-slip conditions (i.e. $V_\parallel(r/a = 0.85) = 0$) has also been run for the same simulation time. In contrast to the previous simulations where the effect of modified boundary conditions had a limited impact

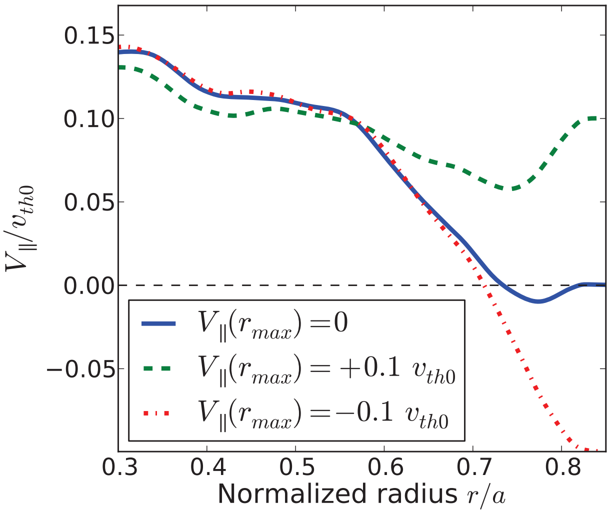

Figure 5.10: Mean parallel velocity profile for simulations with poloidally homogeneous boundary conditions, either no-slip or with $V_{\|}(r_{max}) = \pm 0.1 v_{th0}$. The profiles have been averaged over a time frame of approximately $5\,10^3\,\omega_c^{-1}$.

on the radial velocity profile, the homogeneous conditions applied here strongly impact the core rotation, at least up to $r/a \sim 0.6$. For the case where $V_{\|}(r_{max}) = -0.1 v_{th0}$, no significant effect on parallel velocity can be measured inside this radius, as observed differences remain well within the level of fluctuations. In the case where $V_{\|}(r_{max}) = 0.1 v_{th0}$, the gradient of toroidal rotation is strongly reduced, and this appears to lead to a modification of the rotation profile throughout the radial domain. This suggests that a local description of momentum transport in the core is not adequate as, in certain conditions, edge flows can have a significant impact in the entire plasma. However, the modification observed in Fig. 5.10 for $r/a < 0.6$ is only marginally larger than the observed fluctuations in the velocity profile. In order to confirm this result with more certainty, the simulation would need to be run for a time larger than the energy confinement time, which was not the case here as more numerical resources would be necessary for such a simulation.[3]. Additionally, it would be useful to perform similar simulations at lower values of ρ_* in order to investigate whether the penetration – or screening – of edge flows is dependent on the machine size.

5.4 Discussion

As a conclusion to this chapter, it appears that the description of turbulence, and especially momentum transport, in terms of local transport coefficients, cannot capture the complexity of the processes at play. Even with flux-surface averaging, which tends to reduce the intermittent effects, transport is clearly non-diffusive and large-scale events *are* observed. This is even more critical when considering (poloidally) local transport, as avalanches are strongly localized events, and the intermittency of turbulent transport is not poloidally homogeneous. In the case of momentum transport, the influence of edge

---

[3] Each of the simulations presented in Fig. 5.10, for a simulation time of $1.8\,10^5\,\omega_c^{-1}$, required approximately $8\,10^5$ computing hours, running on 8192 processors on the *Curie* supercomputer of the Très Grand Centre de Calcul (TGCC) in Bruyères-le-Châtel, France.

flows on core rotation can lead to additional, complex, non-local effects which would be difficult to capture in a local approach.

Although the statement may appear self-contradictory, one may actually recover a local description by performing averages. The flux-surface average is not sufficient, and averages over time and over extended radial domains must also be performed for a description in terms of transport coefficients to be foreseeable. Through adequate averaging, for instance, the gyro-Bohm scaling of turbulent transport can be recovered. Such results are encouraging as describing intermittent transport by the average resulting transport may be a useful *ansatz* for computationally light transport codes. However, it is not clear that the complex dynamics observed in simulations can be correctly captured by a local description. For instance, meso-scale events and self-organization can play an important role, as discussed in [SvMC05].

Recently, a method was suggested which considers the calculation of transport coefficients as an inverse problem [ES12], with a matricial approach aiming to compute diffusion and convection coefficients from experimental plasma profiles in modulation experiments. Importantly, this approach is capable of identifying situations where such a description is *not* possible. One could apply this method to modulation experiments not only in tokamaks but also in numerical simulations.[4] In fact, one may expect the method to be more efficient in the latter case, as the precision of the method depends on the accuracy with which the source is computed. Performing various choices of averaging, the method could provide insights into the question of whether a description of turbulence in terms of local transport coefficients is relevant, and at which – spatial and temporal – scales.

Finally, if a local description proves inefficient, a possible compromise between local transport coefficients and complete turbulence simulations could be the use of nonlocal kernels [DPDG+10], which may provide a more satisfying description of the meso-scale and intermittent dynamics of turbulent transport with only a limited increase in numerical cost.

---

[4] As a caveat, note that this method would require very long simulation times, greater than the energy confinement time. For values of ρ_* relevant to ITER, such simulations are hard to imagine with global gyrokinetic codes at the moment, but may be achievable in the future with increased numerical resources. Otherwise, this could be analyzed in flux-tube simulations or, in order to remain in the flux-driven regime, in fluid simulations.

Chapter 6

Toroidal symmetry breaking by the equilibrium magnetic field

> The law that entropy always increases holds, I think, the supreme position among the laws of Nature. If someone points out to you that your pet theory of the universe is in disagreement with Maxwell's equations — then so much the worse for Maxwell's equations. If it is found to be contradicted by observation — well, these experimentalists do bungle things sometimes. But if your theory is found to be against the second law of thermodynamics I can give you no hope; there is nothing for it but to collapse in deepest humiliation.
>
> Sir Arthur Stanley Eddington, *The Nature of the Physical World*, 1928

An important result of the conservation equation for toroidal momentum derived in chapter 3 is that the generation of toroidal rotation in tokamaks requires a breaking of axisymmetry. One means of breaking the axisymmetry, explored in the previous chapters, is electrostatic turbulence Another possibility is via a non-axisymmetric equilibrium magnetic field. We will see that, even in the absence of turbulence and through purely collisional processes, this can lead to the generation of toroidal rotation.

In particular, for any tokamak, the finite number of coils gives rise to toroidal magnetic field ripple, i.e. variations of the magnetic field amplitude along the field lines. Through collisional processes, the presence of ripple leads to a neoclassical friction driving the toroidal velocity in the counter-current direction. In tokamaks where the ripple amplitude is strong, such as Tore Supra or JT-60U, this effect can be dominant in generating the toroidal rotation profile. In the general case, the neoclassical friction will compete with other mechanisms resulting from various symmetry breakers such as electrostatic turbulence, as will be discussed in section 6.4, fast particle losses [EJH+04] or magnetohydrodynamic (MHD) modes [SCH+90], which may drive the plasma in either co-current or counter-current direction.

Experimentally, toroidal field ripple was found to play an important role in determining toroidal rotation in various tokamaks. Dedicated experiments on JET [dVSP+08, CAB+09, NJE+10] found that, when increasing the ripple, a significant torque drives the toroidal rotation in the counter-current direction. Similar observations were made on JT-60U [YKT+06, UOK+07]. Recently, dedicated experiments were performed on Tore Supra where the ripple amplitude was varied by over an order of magnitude [FGT+11].

On the theoretical side, the effect of a non-axisymmetric magnetic field on toroidal rotation was the subject of much work in the 1990s [Yus90, Mik95, KMS95, Sha96, Kov99].

The issue was extensively developed for the study of the penetration of Resonant Magnetic Perturbations (RMPs), which are also static non-axisymmetric magnetic fields and can be tackled using the same theoretical framework as magnetic field ripple [Sha03, CHC07, BHG+09]. Recently, the predictions for neoclassical toroidal rotation were reviewed in [GAT+10]. In this work, an approach based on an extremum of the entropy production rate allows one to recover and clarify previous theoretical predictions in a large number of limit cases. Long-standing contradictions between previous works [Mik95, Kov99] are also resolved by this work.

We review in sections 6.1 and 6.2 the methodology developed in [GAT+10] and present the key resulting theoretical predictions in 6.3. Gyrokinetic simulations including both turbulent momentum transport and the effect of toroidal field ripple will be presented in section 6.4.

6.1 Obtaining neoclassical equilibria from entropy production rates

In this section, we present the method for determining the neoclassical equilibrium in tokamaks in the presence of toroidal field ripple. In fact, the approach is more general as it allows for an arbitrary helical perturbation. Several regimes are identified depending on collisionality and on the amplitude of the helical perturbation. For each regime, using a variational principle based on entropy production rates, one can compute the neoclassical equilibrium in terms of particle, heat and momentum transport. The aim of this section is not to present the complete and detailed calculations, which can be found in [GAT+10, GAS+10]. Rather, we will present the key concepts to carry out the calculations and the different regimes which can be obtained depending on the perturbation. A summary of the results will follow in section 6.3.

The equilibrium Hamiltonian is $H = mv_{G\parallel} + \mu B + e\phi$ where B is a *reference* – uniform – magnetic field and ϕ is the *mean* electric potential. The perturbed Hamiltonian reads

$$\delta H = -\mu B\epsilon \cos\theta + \mu B\delta \cos\left(N\varphi + M\theta\right) \tag{6.1}$$

where $\epsilon = \frac{r}{R}$ and $\delta(r)$ is the amplitude of the helical perturbation. For simplicity, we assume here that the perturbation does not depend on the poloidal angle. In the case of toroidal field ripple, $M = 0$ and N corresponds to the number of toroidal field coils ($N = 18$ for Tore Supra and ITER). Note that the perturbed Hamiltonian contains both the standard neoclassical (banana) effects and the helical perturbation. Particles can be trapped by either perturbation, as can be seen in Fig. 6.1, which corresponds to a case with strong perturbation amplitude and $M = 0$. Particles will be trapped in the helical perturbation when the perturbed magnetic field along a field line exhibits a local extremum, as is the case in Fig. 6.1. The condition for this local trapping depends on the perturbation amplitudes and mode numbers and will be detailed in section 6.2.2.

The distribution function is a function of motion invariants and is close to a local Maxwellian, namely

$$F_M = \frac{\mathcal{N}}{\left(2\pi T/m\right)^{3/2}} \exp\left(-\frac{H}{T}\right)\left(1 + \frac{mWv_\parallel}{T}\right) \tag{6.2}$$

The function $\mathcal{N}$ is defined as $\mathcal{N} = n \exp\left(e\phi/T\right)$. The density n, electric potential ϕ and temperature T are functions of the toroidal kinetic momentum $p_\varphi = -e\chi + mRv_\parallel$, while

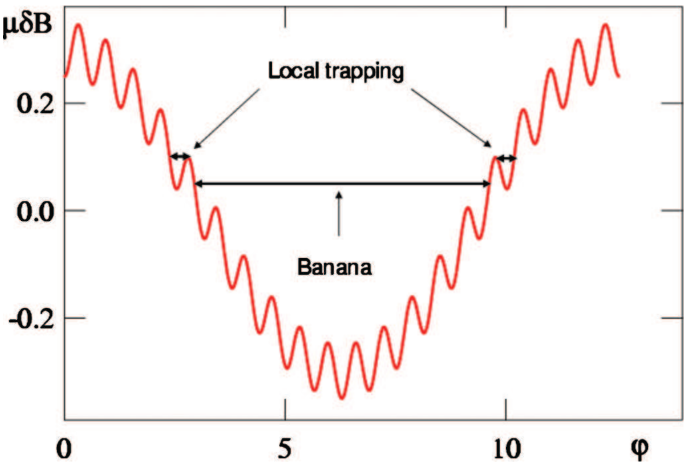

Figure 6.1: Amplitude of the perturbed Hamiltonian along a field line $\theta = \varphi/q$. The parameters are $q = 2$, $\epsilon = 0.3$, $N = 10$ and $\delta = 0.05$.

W is a function of the total energy H that ensures finite mean parallel velocity and parallel thermal flux. The distribution function F_M, Eq. (6.2), is an exact solution of the kinetic equation $dF/dt = \mathcal{C}(F)$ for the unperturbed problem when the condition

$$\frac{RT}{e}\partial_\psi \Xi + W = V_T \tag{6.3}$$

is fulfilled, where

$$\partial_\psi \Xi = \partial_\psi \ln n + \frac{e}{T}\partial_\psi \phi + \left(\frac{E}{T} - \frac{3}{2}\right)\partial_\psi \ln T \tag{6.4}$$

and V_T is the toroidal velocity (strictly speaking the parallel velocity).

Multiplying Eq. (6.2) by $v_\parallel^2/v_T^2$, where $v_T = \sqrt{T/m}$ is the thermal velocity, and integrating over the velocity space yields the conventional force balance equation in the large aspect ratio limit [GDPN+09]

$$-\partial_r \phi + V_p B - V_T B_p = \frac{\partial_r p}{ne} \tag{6.5}$$

where V_p is the poloidal velocity and B_p is the poloidal component of the magnetic field. With this equation and following the equations derived in [GDPN+09, GAT+10], one can compute the resonant entropy production rate and express it using the general form of transport equations as

$$\dot{S}_{res} = -\frac{1}{2}\int dV n \left(\frac{\Gamma}{n}\frac{\partial_r n}{n} + \frac{\mathcal{M}}{nmv_T}\frac{V_T}{v_T} + \frac{Q}{nT}\frac{\partial_r T}{T}\right) \tag{6.6}$$

where $dV = 4\pi^2 R r dr$. Γ and Q are the particle and heat fluxes, and $\mathcal{M}$ is the rate of dissipated momentum due to toroidal collisional damping. These fluxes can therefore be calculated as functional derivatives of the resonant entropy production rate

$$\Gamma = -\frac{1}{2}\frac{\delta \dot{S}_{res}}{\delta \partial_r \ln n} \tag{6.7}$$

$$\mathrm{M} = -\frac{1}{2} n m v_T^2 \frac{\delta \dot{S}_{res}}{\delta V_T} \tag{6.8}$$

$$Q = -\frac{1}{2} n T \frac{\delta \dot{S}_{res}}{\delta \partial_r \ln T} \tag{6.9}$$

where $\dot{S}_{res}$ is the total entropy production rate, and the partial derivatives on the r.h.s. are functional derivatives. These derivatives provide the particle, momentum and heat fluxes.

The strategy to determine the neoclassical equilibrium from the entropy production rate is rather straightforward. First the extremum of the entropy production rate with respect to density yields the particle flux. As the electron flux is smaller than the ion flux by a factor $\sqrt{m_e/m_i} \ll 1$. Therefore the ambipolarity constraint reduces to a condition of vanishing ion flux, $\Gamma = 0$. This constraint provides a relation between the radial electric field, toroidal velocity and gradients of density and temperature (the poloidal velocity can be eliminated using the force balance equation). The dynamics governing radial electric field is assumed to be faster than that for the toroidal velocity. Second the extremum with respect to toroidal velocity allows one to determine the damping rate in the toroidal direction and another relation between the radial electric field E_r, toroidal velocity V_T, and gradients of density and temperature. Finally, the extremum with respect to temperature gradient provides the ion thermal diffusivity.

6.2 Entropy production rates

As shown in the previous section, in order to obtain the neoclassical equilibrium, one must compute the resonant entropy production rate $\dot{S}_{res}$ due to the perturbed Hamiltonian (6.1). This calculation is complicated by the fact that the two perturbations in (6.1) resonate on neighboring resonant surfaces in phase-space, namely where $v_{G\|} = 0$. This general problem is addressed in [GAT+10]. When both perturbations are taken into account, one must be considered as the primary perturbation and the other as secondary. Therefore, the resulting entropy production depends on the orderings between the two perturbations, which governs the choice of the primary perturbation. Accordingly, the total entropy production rate can be split into four contributions

$$\dot{S}_{res} = \dot{S}_{tor} + \dot{S}_{hel} + \dot{S}'_{tor} + \dot{S}'_{hel} \tag{6.10}$$

where each entropy production rate describes a specific process:

- $\dot{S}_{tor}$ corresponds to toroidally trapped particles,
- $\dot{S}_{hel}$ corresponds to helically trapped particles,
- $\dot{S}'_{tor}$ due to the effect of the toroidal perturbation on helically trapped particles,
- $\dot{S}'_{hel}$ due to the effect of the helical perturbation on toroidally trapped particles.

Detailed calculations of these terms, using the reduced collision operator presented in section 2.3.2, are given in [GAT+10] and will not be reproduced here, the focus is on the resulting neoclassical equilibria depending on the ordering parameters, i.e. on which term is dominant in (6.10).

6.2.1 Toroidally trapped particles

For toroidally trapped particles only, the entropy production rate corresponds to the standard neoclassical calculation [HH76], and reads

$$\begin{aligned}\dot{S}_{tor} &= \frac{1}{2}\sqrt{\frac{\pi}{2}}\int dVn\frac{qRv_D^2}{v_T}\int_0^{+\infty} du\, e^{-u}u^2 \min\left(1, \frac{4}{\pi}\mathcal{I}\nu^*\frac{\bar{\nu}}{u^{1/2}}\right) \times \\ &\left(\partial_r \ln\mathcal{N} + \left(u-\frac{3}{2}\right)\partial_r \ln T + \frac{eB_p}{T}V_T\right)^2 \qquad (6.11)\end{aligned}$$

where $v_D = \frac{T}{eBR}$ is the thermal curvature drift velocity, $\mathcal{I} \simeq 1.38$ and the collisionality ν^*, which is the conventional parameter for neoclassical theory, is defined as in section 2.3.2. The normalized collision frequency is

$$\bar{\nu}(v) = \frac{3}{4}\sqrt{2\pi}\frac{\Phi(v) - G(v)}{v^3} \qquad (6.12)$$

where

$$\begin{aligned}\Phi(v) &= \frac{2}{\sqrt{\pi}}\int_0^v dx \exp\left(-x^2\right) \\ G(v) &= \frac{\Phi(v) - v\Phi'(v)}{2v^2} \qquad (6.13)\end{aligned}$$

Close to the resonance $v_{G\parallel} = 0$, one has $v = (\mu B/T)^{1/2} = \sqrt{u}$.

6.2.2 Helically trapped particles

We call $M_h = M + Nq$ the helical wave number. If $|M_h| \gg 1$, which is relevant for toroidal field ripple in tokamaks, local trapping occurs when $Y = \alpha\,|\sin\theta| < 1$, where $\alpha = \frac{\epsilon}{|M_h|\delta}$. This condition defines for each minor radius r a domain in θ for which there exists locally trapped particles. One can define an effective ripple amplitude, which is the depth of the magnetic well along the field lines between successive minima and maxima [Yus90], namely

$$2\delta_{eff} = \frac{B_{max}}{B_{min}} - 1 = 2\delta\left(\sqrt{1-Y^2} - Y\arccos Y\right) \qquad (6.14)$$

The collisionality paremeter for helical trapping, which is the equivalent of ν^* for toroidal trapping, is $\nu^*_{hel} = \frac{\nu^*}{|M_h|}\left(\frac{\epsilon}{\delta}\right)^{3/2}$. We also define an effective collisionality $\nu^*_{eff} = \max(1, M_h^2)\nu^*$. Note that, for the case of ripple in tokamaks, $\nu^*_{eff} = M_h^2\nu^*$. With these notations, the entropy production rate due to helically trapped particles reads

$$\begin{aligned}\dot{S}_{hel} &= \frac{1}{2}\sqrt{\frac{\pi}{2}}\int dVn\frac{M^2}{|M_h|}\left(\frac{\delta}{\epsilon}\right)^2\frac{qRv_D^2}{v_T}\int_0^{+\infty} due^{-u}u^2 \\ &\left(G_0'(\alpha) + G_0(\alpha)\min\left(1, \frac{4}{\pi}\mathcal{I}\nu^*_{hel}\frac{\bar{\nu}}{u^{1/2}}\right)\right) \\ &\left(\partial_r \ln\mathcal{N} + \left(u-\frac{3}{2}\right)\partial_r \ln T + \frac{eB_p}{T}\frac{M_h}{M}V_T\right)^2 \qquad (6.15)\end{aligned}$$

where G_0 and G_0' are form factors [GAT+10]. When $\alpha \gg 1$, they are given by $G_0(\alpha) = \frac{1}{2\pi}\int_{Y<1} d\theta$ and $G_0'(\alpha) = \frac{1}{2\pi}\int_{Y>1} d\theta$. We recall that the integration domains $Y < 1$

correspond to the fraction of phase-space where helical trapping occurs. In the opposite limit $\alpha \ll 1$, one gets $G_0 = 1$ and $G_0' = 0$.

In the specific case where $M = 0$ and $\nu^*_{hel} \gg 1$, corresponding to ripple trapped particles in the plateau regime, Eq. (6.15) can be replaced by its limit when $M \to 0$, which yields

$$\dot{S}_{hel} = \sqrt{\frac{\pi}{2}} \int dV n \left(\frac{\delta}{\epsilon}\right)^2 \frac{qRv_D^2}{v_T} \int_0^{+\infty} due^{-u}u^2 \left(\frac{eB_p}{T}V_T\right)^2 \tag{6.16}$$

as $G_0 + G_0' = 1$. Notice that the mode number N no longer appears in this expression.

6.2.3 Effect of the toroidal perturbation on helically trapped particles

We now consider the case where the helical trapping is the primary perturbation to the Hamiltonian while toroidal trapping by the vertical drift is the secondary perturbation. For large collisionality $\nu^*_{hel} \gg 1$, this term is small, as the effect of collisional detrapping will be more important than the secondary perturbation. When $\nu^*_{hel} \ll 1$, the entropy production rate reads

$$\begin{aligned} \dot{S}'_{tor} &= K_{hel} \int dV G_1(\alpha) n \left(\frac{Nq}{M_h}\right)^2 \left(\frac{\delta}{\epsilon}\right)^{3/2} \frac{1}{\nu^*} \frac{qRv_D^2}{v_T} \\ & \int_0^{+\infty} due^{-u}u^{5/2} \frac{1}{\bar{\nu}(u)} \left(\partial_r \ln \mathcal{N} + \left(u - \frac{3}{2}\right) \partial_r \ln T\right)^2 \end{aligned} \tag{6.17}$$

where $K_{hel} = \left(\frac{2}{\pi}\right)^{3/2} \min\left(\frac{8}{9}, |M_h|\right)$ and G_1 is a form factor [GAT+10], given by $G_1(\alpha) = \frac{1}{2\pi} \int_{Y<1} d\theta \sin^2\theta$ when $\alpha \gg 1$. In the opposite limit $\alpha \ll 1$, one gets $G_1 = 1$.

6.2.4 Effect of the helical perturbation on toroidally trapped particles

We now consider the case where the toroidal trapping is the primary perturbation to the Hamiltonian while helical trapping is the secondary perturbation. Similarly to the previous section, this effect will be negligible when $\nu^* \gg 1$ and collisional detrapping dominates.

If $\nu^* \ll 1$, the expression of $\dot{S}'_{hel}$ depends on the effective collision frequency. In the low effective collisionality regime $\nu^*_{eff} \ll 1$

$$\begin{aligned} \dot{S}'_{hel} &= K'_{hel} \int dV n (Nq)^2 \left(\frac{\delta}{\epsilon}\right)^2 \frac{1}{\nu^*} \frac{qRv_D^2}{v_T} \\ & \int_0^{+\infty} due^{-u}u^{5/2} \frac{1}{\bar{\nu}(u)} \left(\partial_r \ln \mathcal{N} + \left(u - \frac{3}{2}\right) \partial_r \ln T\right)^2 \end{aligned} \tag{6.18}$$

where $K'_{hel} = \left(\frac{2}{\pi}\right)^{3/2} \min\left(\frac{8}{9}, \frac{1}{|M_h|^3}\right)$, while for larger effective collisionality $\nu^*_{eff} \gg 1$ one has

$$\begin{aligned} \dot{S}'_{hel} &= \frac{1}{2}\sqrt{\frac{\pi}{2}} \int dV n \frac{N^2q^2}{|M_h|} \left(\frac{\delta}{\epsilon}\right)^2 \frac{qRv_D^2}{v_T} \\ & \int_0^{+\infty} due^{-u}u^2 \left(\partial_r \ln \mathcal{N} + \left(u - \frac{3}{2}\right) \partial_r \ln T\right)^2 \end{aligned} \tag{6.19}$$

6.3 Neoclassical equilibria in limit cases

The different contributions to the total entropy production rate Eq. (6.10) have been computed in the previous section 6.2, and can now be used to determine the neoclassical equilibrium, following the procedure described in section 6.1. Several regimes must be considered, depending on whether local trapping occurs or not, and depending on the various collisionality parameters. We will focus on cases with a weak helical perturbation where local trapping does not occur in section 6.3.1 while section 6.3.2 will focus on strong perturbation regimes where helical trapping is present. Note that we restrict the study to the case of toroidal field ripple, which implies $M = 0$.

The radial electric field, poloidal velocity and toroidal velocity are generically of the form

$$\frac{eE_r}{T} = \partial_r \ln n + k_E \partial_r \ln T \tag{6.20}$$

$$V_p = k_p \frac{\partial_r T}{eB} \tag{6.21}$$

$$V_T = k_T \frac{\partial_r T}{eB_p} \tag{6.22}$$

The aim of the following sections is to obtain the expressions for k_E, k_p and k_T in the various regimes. The heat diffusivity and the friction rate driving the toroidal velocity to its relaxed value Eq. (6.22) can also be derived.

6.3.1 Weak perturbation regime

When the amplitude of the helical perturbation is small, i.e. when $Y > 1$, particles are not trapped in the helical perturbation. In this case, only banana-trapped particles are important. In the total entropy production rate Eq. (6.10), two terms must therefore be taken into account: the entropy productions due to toroidally trapped particles $\dot{S}_{tor}$ and due to the effect of the helical perturbation on these particles $\dot{S}'_{hel}$.

Two regimes can be considered depending on the effective collisionality $\nu^*_{eff} = (Nq)^2\nu^*$. These two limit cases will be referred to as “banana-drift” ($\nu^*_{eff} \ll 1$) and “ripple-plateau” ($\nu^*_{eff} \gg 1$), following the terminology introduced by Yushmanov [Yus90].

Banana-drift regime

For small effective collisionality $\nu^*_{eff} \ll 1$, the expression for the total entropy production rate is $\dot{S}_{res} = \dot{S}_{tor} + \dot{S'}_{hel}$ where $\dot{S}_{tor}$ is given by Eq. (6.11) and $\dot{S'}_{hel}$ is given by Eq. (6.18). From this expression of $\dot{S}_{res}$, the ambipolarity condition $\Gamma = 0$ reads

$$(1 + k_1)\partial_r \ln \mathcal{N} + (3.37 - 0.17k_1)\partial_r \ln T + k_1 \frac{eB_pV_T}{T} = 0 \tag{6.23}$$

where the collisionality parameter k_1 is defined as

$$k_1 \simeq \frac{1.1}{7.41G_2(\alpha)} Nq \left(\frac{\epsilon\nu^*}{\delta}\right)^2 \tag{6.24}$$

where G_2 is a form factor [GAT$^+$10]. A high collisionality regime is obtained when $\nu^* \gg \frac{1}{\sqrt{Nq}}\frac{\delta}{\epsilon}$ Note that, for this condition to be consistent with $\nu^*_{eff} \ll 1$, one must have $\delta/\epsilon \ll$

$(Nq)^{-3/2}$. If this is the case, two separate regimes, are identified, namely “banana-drift weakly collisional” and “banana-drift collisional”.

The extremalization with respect to the toroidal velocity yields the following evolution equation

$$\partial_t V_T = -\frac{1.1}{1+k_1}\sqrt{\epsilon}\nu\left(V_T - 3.54\frac{\partial_r T}{eB_p}\right) \tag{6.25}$$

When the toroidal velocity has relaxed, i.e. $V_T = 3.54\frac{\partial_r T}{eB_p}$, the poloidal velocity is found by combining the ambipolarity condition (6.23) with the force balance equation. It turns out that, whatever the collisionality, it is equal to the conventional neoclassical poloidal velocity

$$V_p = 1.17\frac{\partial_r T}{eB} \tag{6.26}$$

The force balance equation yields the radial electric field

$$\frac{eE_r}{T} = \partial_r \ln n + 3.37\partial_r \ln T \tag{6.27}$$

Finally the extremalization with respect to $\partial_r \ln T$ yields the heat flux $Q = -\chi_i n \partial_r T$ where

$$\chi_i = 36.94 G_2(\alpha)\frac{\delta^2}{Nq\epsilon^{1/2}}\frac{v_D^2}{\nu}(1+0.246k_1) \tag{6.28}$$

These results are consistent with the values given by Kovrizhnykh [Kov99]. At high collisionality, $k_1 \gg 1$, the heat diffusivity coincides with the banana neoclassical value $1.35\nu^*\frac{qRv_D^2}{v_T}$, as it should, since in that case the dominant entropy production rate comes from banana particles.

Ripple-plateau regime

For large effective collisionality $\nu^*_{eff} \gg 1$, the expression for the total entropy production rate is $\dot{S}_{res} = \dot{S}_{tor} + \dot{S}'_{hel}$ where $\dot{S}_{tor}$ is given by Eq. (6.11) and $\dot{S}'_{hel}$ is given by Eq. (6.19). The ambipolarity condition reads

$$(1+k_2)\partial_r \ln \mathcal{N} + (1.5 - 0.17k_2)\partial_r \ln T + k_2\frac{eB_pV_T}{T} = 0 \tag{6.29}$$

where the collisionality parameter k_2 is defined as

$$k_2 \simeq \sqrt{\frac{2}{\pi}}\frac{1.1}{G_2(\alpha)}\frac{1}{Nq}\left(\frac{\epsilon}{\delta}\right)^2\nu^* \tag{6.30}$$

The weak collisional regime is defined as $\nu^* \ll Nq\left(\frac{\delta}{\epsilon}\right)^2$, which is consistent with $\nu^*_{eff} > 1$ if $\delta/\epsilon \gg (Nq)^{-3/2}$. In this case, as in the previous section, two regimes are identified, namely “ripple-plateau weakly collisional” and “ripple-plateau collisional”.

The extremalization with respect to the toroidal velocity yields the following evolution equation

$$\partial_t V_T = -\frac{1.1}{1+k_2}\sqrt{\epsilon}\nu\left(V_T - 1.67\frac{\partial_r T}{eB_p}\right) \tag{6.31}$$

The poloidal velocity is found by combining the relaxed toroidal velocity $V_T = 1.67\frac{\partial_r T}{eB_p}$ with the force balance equation and the ambipolarity condition Eq. (6.29). Again it is

regime	banana-drift weakly collisional	banana-drift collisional	ripple-plateau collisional
collisionality	$\nu^* \ll \frac{1}{\sqrt{Nq}}\frac{\delta}{\epsilon}$	$\frac{1}{\sqrt{Nq}}\frac{\delta}{\epsilon} \ll \nu^* \ll \frac{1}{N^2q^2}$	$\frac{1}{N^2q^2} \ll \nu^*$
k_E	3.37	3.37	1.5
k_p	1.17	1.17	1.17
k_T	3.54	3.54	1.67
toroidal damping rate ν_φ	$1.1\sqrt{\epsilon}\nu$	$7.41 G_2(\alpha)\frac{\delta^2\epsilon^{3/2}}{Nq^3}\frac{1}{\nu}\left(\frac{v_T}{R}\right)^2$	$\sqrt{\frac{\pi}{2}}G_2(\alpha)N\delta^2\frac{v_T}{R}$
heat diffusivity χ_i	$1.35\nu^*\frac{qRv_D^2}{v_T}$	$36.94 G_2(\alpha)\frac{\delta^2}{Nq\epsilon^{1/2}}\frac{v_D^2}{\nu}$	$1.35\nu^*\frac{qRv_D^2}{v_T}$

Table 6.1: Neoclassical equilibrium without local trapping $Y > 1$, when $\frac{\delta}{\epsilon} \ll \frac{1}{(Nq)^{3/2}}$.

regime	banana-drift weakly collisional	ripple-plateau weakly collisional	ripple-plateau collisional
collisionality	$\nu^* \ll \frac{1}{N^2q^2}$	$\frac{1}{N^2q^2} \ll \nu^* \ll Nq\left(\frac{\delta}{\epsilon}\right)^2$	$Nq\left(\frac{\delta}{\epsilon}\right)^2 \ll \nu^*$
k_E	3.37	1.5	1.5
k_p	1.17	1.17	1.17
k_T	3.54	1.67	1.67
toroidal damping rate ν_φ	$1.1\sqrt{\epsilon}\nu$	$1.1\sqrt{\epsilon}\nu$	$\sqrt{\frac{\pi}{2}}G_2(\alpha)N\delta^2\frac{v_T}{R}$
heat diffusivity χ_i	$1.35\nu^*\frac{qRv_D^2}{v_T}$	$3\sqrt{\frac{\pi}{2}}G_2(\alpha)N\left(\frac{q\delta}{\epsilon}\right)^2\frac{Rv_D^2}{v_T}$	$1.35\nu^*\frac{qRv_D^2}{v_T}$

Table 6.2: Neoclassical equilibrium without local trapping $Y > 1$, and $\frac{\delta}{\epsilon} \gg \frac{1}{(Nq)^{3/2}}$.

found to be equal to the conventional neoclassical poloidal velocity $V_p = 1.17\frac{\partial_r T}{eB}$ whatever the collisionality parameter k_2. The force balance equation yields the radial electric field

$$\frac{eE_r}{T} = \partial_r \ln n + 1.5\partial_r \ln T \tag{6.32}$$

Finally the extremalization with respect to $\partial_r \ln T$ yields the heat flux $Q = -\chi_i n \partial_r T$ where

$$\chi_i = 3\sqrt{\frac{\pi}{2}}G_2(\alpha)N\left(\frac{q\delta}{\epsilon}\right)^2\frac{Rv_D^2}{v_T}(1 + 0.41k_2) \tag{6.33}$$

The heat diffusivity coincides with the banana neoclassical value at high collisionality $k_2 \gg 1$ as expected.

Summary of the weak perturbation regime

The weak perturbation regime is split into two regimes, "banana-drift" ($\nu^*_{eff} \ll 1$) and "ripple-plateau" ($\nu^*_{eff} \gg 1$). One of these two regimes, depending on the relative amplitudes of δ/ϵ and $(Nq)^{-3/2}$, will be split into a weakly collisional and a collisional regime. In either case, three regimes are obtained. For each regime, the values of k_E, k_p, k_T and the relevant damping rates have been calculated. These results are summarized in tables 6.1, and 6.2.

6.3.2 Strong perturbation regime

Large helical perturbations can locally trap particles, in the case of $Y < 1$, where we recall the definition $Y = \frac{\epsilon}{Nq\delta}|\sin\theta|$ in the case of an $M = 0$ perturbation. In tokamaks, this condition may be present for large ripple amplitudes. As in the weak perturbation regime, many situations are possible depending on the orderings, especially since all four contributions to the entropy production rate in Eq. (6.10) should be taken into account. We focus here on an experimentally relevant case for tokamaks with $\nu^* \ll 1$, implying that the relevant contributions will be those proportional to $1/\nu$, i.e. $\dot{S}'_{tor}$ and $\dot{S}'_{hel}$, Eqs. (6.17) and (6.18). For standard values of collisionality, ripple amplitude and toroidal mode number, the characteristic frequencies verify $\nu^*_{eff} = (Nq)^2\nu^* \gg 1$ and $\nu^*_{hel} = \frac{\nu^*}{|M_h|}\left(\frac{\epsilon}{\delta}\right)^{3/2} \ll 1$. With these conditions, particles trapped in the ripple perturbation are in the ripple-plateau regime, and the dominant entropy production rate is $\dot{S}'_{tor}$, as given by Eq. (6.17) with $G_1 = 1$ considering that all the particles are helically trapped. The extremalization of this expression yields the particle and heat fluxes as

$$\begin{pmatrix} \Gamma \\ Q \end{pmatrix} = -nD_{lt} \begin{pmatrix} \partial_r \ln \mathcal{N} + 3.37\partial_r \ln T \\ 5\partial_r T \end{pmatrix} \tag{6.34}$$

where $D_{lt} = 6.58Nq\delta^{3/2}v_D^2/\nu$. The radial electric field can then be obtained from the ambipolarity constraint $\Gamma = 0$, leading to

$$\frac{eE_r}{T} = \partial_r \ln n + 3.37\partial_r \ln T \tag{6.35}$$

In order to obtain the toroidal velocity, which cannot be derived from $\dot{S}'_{tor}$ and $\dot{S}'_{hel}$, the other contributions to the entropy production rate must be considered. For $M = 0$, $\dot{S}_{tor} \gg \dot{S}_{hel}$ is the dominant term. Thus, one finds $V_T = 3.54\frac{\partial_r T}{eB_p}$ with a damping rate $\nu_\varphi \simeq 1.1\sqrt{\epsilon}\nu$. Note that neither the equilibrium velocity nor the damping rate depend on the ripple characteristics in this case. Finally, the force balance equation yields the poloidal velocity as $V_p = 1.17\frac{\partial_r T}{eB}$

6.4 Interplay between neoclassical and turbulent momentum transport

6.4.1 Implementing toroidal field ripple in GYSELA

The turbulent momentum transport studied in chapter 4 can also be described in terms of entropy production rates [GAS+12]. However, in such an approach, neoclassical and turbulent processes are simply additive. The aim of this section is to explore the competition between neoclassical and turbulent momentum transport by taking into account the effects of a non-axisymmetric magnetic field in the GYSELA code.

In terms of code development, this could in principle be achieved by modifying the equilibrium magnetic field in the code. As the GYSELA code has been developed assuming an axisymmetric **B** field, this would require substantial modifications to the code[1]. However, in the context of toroidal field ripple, the amplitude of the non-axisymmetric component of the magnetic field is small compared to the equilibrium field. Thus, one can consider an axisymmetric equilibrium field, and take into account toroidal field ripple as a

---

[1] For example, the description of the metric would be modified, and the velocity-space Jacobian $B^*_{||}$ would depend on the toroidal angle. In addition to the important implications for code development, this would significantly increase the memory cost of the simulations. As a consequence, this would deteriorate the scalability of the code when running simulations on a large number of processors.

perturbation. This can be expressed in terms of a perturbation to the Hamiltonian, given by Eq. (2.5), which we recall here:

$$\bar{H} = \frac{1}{2} m {v_{G\parallel}}^2 + e\bar{\phi} + \mu B \tag{6.36}$$

If the magnetic field is expressed as $\mathbf{B} = \mathbf{B_{eq}} + \delta\mathbf{B}$, then its amplitude can be computed at the first order in $\delta B / B_{eq}$ as

$$\begin{aligned} \|\mathbf{B_{eq}} + \delta\mathbf{B}\| &\simeq \left(B_{eq}^2 + 2\mathbf{B_{eq}} \cdot \delta\mathbf{B}\right)^{1/2} \\ &\simeq B_{eq} + \underbrace{\mathbf{b_{eq}} \cdot \delta\mathbf{B}}_{\equiv \delta B_\parallel} \end{aligned} \tag{6.37}$$

where $\mathbf{b_{eq}}$ is the unit vector in the direction of $\mathbf{B_{eq}}$ Thus, toroidal field ripple can be described by an additional perturbation $\mu\delta B_\parallel$ to the Hamiltonian Eq. (6.36), and we consider a perturbation $\delta B_\parallel$ of the form $\delta \cos(N\varphi)$. In principle, the perturbation amplitude δ could depend on the radius and poloidal angle, but we assume here a homogeneous ripple amplitude.

6.4.2 Theoretical predictions for the perturbations considered

We consider a simulation with normalized gyroradius $\rho_* = 1/150$ and collisionality $\nu^* = 0.02$. The aspect ratio is $R/a = 3.2$ and the safety factor profile is $q(r) = 1.5 + 1.7\,(r/a)^{2.8}$. The simulation was run without toroidal field ripple for approximately $3.10^5\,\omega_c^{-1}$. Several simulations were then performed from this starting point with various ripple perturbations. Before discussing the results in terms of momentum transport, it is useful to relate the perturbations considered here with the theoretical predictions from section 6.3.

First of all, we consider a perturbation with $\delta = 5.10^{-3}$ and a toroidal mode number $N = 8$. This choice of mode number, smaller than for most cases of toroidal field ripple in tokamaks[2], is imposed by the resolution of the simulation in the toroidal direction, as the presence of ripple generates Fourier modes at the harmonics of the toroidal mode number (see section 6.4.3). With this perturbation, the effect of local trapping is expected to be small, as the domain where particles can be trapped is narrow[3], as can be seen in Fig. 6.2a. For the domain without local trapping, we can compare the values used here with the limits identified in section 6.3.1. Throughout most of the simulation domain, we find that $\delta/\epsilon > (Nq)^{-3/2}$ and $\nu^* > Nq(\delta/\epsilon)^2$. Thus, the particles are expected to be mainly in the ripple-plateau collisional regime (see table 6.2). We recall that this implies a toroidal damping rate of $\nu_\varphi \sim N\delta^2 \frac{v_T}{R}$ towards a relaxed toroidal velocity $V_T = 1.67 \frac{\partial_r T}{eB_p}$. This regime was previously identified as relevant in experimental observations on Tore Supra [FGT+11], albeit for higher toroidal mode number and larger ripple amplitude.

We also consider simulations with higher ripple amplitudes. For $\delta = 10^{-2}$, the local trapping region ($Y < 1$) is larger, as can be seen in Fig. 6.2b. In this region, the conditions described in section 6.3.2 for the strong perturbation regime are verified, i.e. $\nu^*_{eff} \gg 1$ and $\nu^*_{hel} \ll 1$. For this situation, where particles trapped by the toroidal field ripple are in the ripple-plateau regime, the damping rate is $\nu_\varphi = 1.1\sqrt{\epsilon}\nu$ and the relaxed toroidal velocity is $V_T = 3.54 \frac{\partial_r T}{eB_p}$. Increasing the ripple amplitude also implies that the region without local

---

[2] For example, the number of toroidal field coils is $N = 18$ for Tore Supra and ITER

[3] Note that a domain where local trapping occurs is always present near $\theta = 0$ and $\theta = \pi$ due to the expression of the local trapping condition.

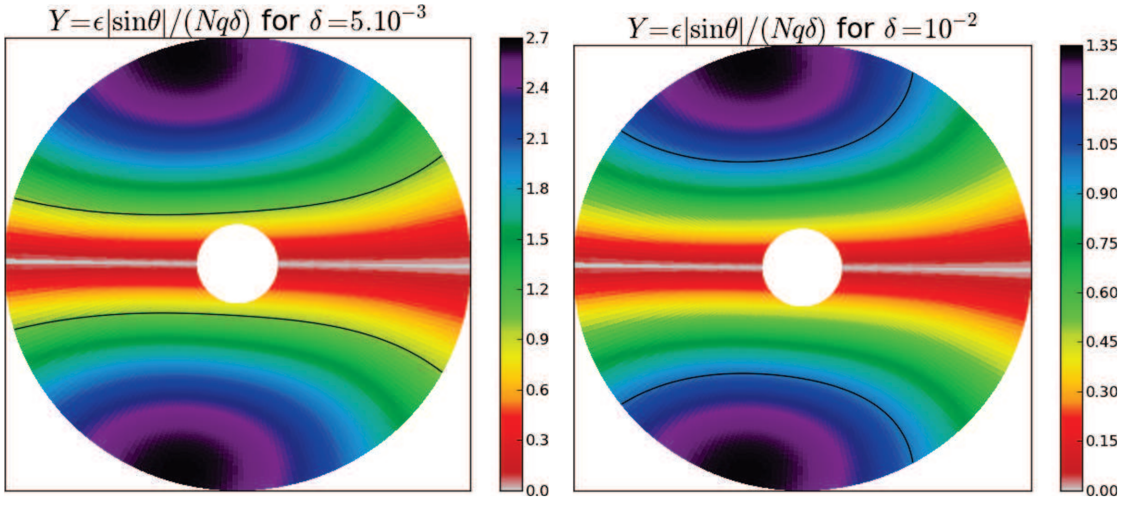

(a) (b)

Figure 6.2: Poloidal cross-sections of the condition for local trapping in the ripple perturbation with the parameters: $R_0/a = 3.2$, $N = 8$ and (a) $\delta = 5.10^{-3}$ or $\delta = 10^{-2}$. Local trapping occurs when $Y < 1$, corresponding to the domain between the two black lines.

trapping moves from the ripple-plateau collisional regime to the ripple-plateau *weakly* collisional regime (see table 6.2). The damping rate becomes $\nu_\varphi = 1.1\epsilon\nu$ while the relaxed velocity remains $V_T = 1.67\frac{\partial_r T}{eB_p}$. On a given flux-surface, both regimes are present, and making a general theoretical prediction is tricky. However, the damping rates and relaxed velocities are of the same order of magnitude, and the damping rate is larger than in the case with a weaker perturbation amplitude.

Finally, further increasing the ripple amplitude to $\delta = 2.10^{-2}$, the condition $Y < 1$ is verified throughout the domain, and we are in the situation of strong ripple amplitude. The conditions described in section 6.3.2, $\nu^*_{eff} \gg 1$ and $\nu^*_{hel} \ll 1$, are still verified, therefore we can expect a damping rate $\nu_\varphi = 1.1\sqrt{\epsilon}\nu$ and a relaxed toroidal velocity $V_T = 3.54\frac{\partial_r T}{eB_p}$. Notice that the damping rate in the trapped regime does not depend on the ripple amplitude. However, as the trapping region is larger in this case and the damping rate is weaker in the region without local trapping, the overall damping rate is expected to be larger than for the case $\delta = 10^{-2}$.

6.4.3 Numerical results

A direct result of the addition of toroidal field ripple in the simulation can be observed in the Fourier transform of the electric potential, shown in Fig. 6.3 for the case $\delta = 2.10^{-2}$. Comparing this result with a standard simulation without ripple (for example Fig. 2.7), one finds that the modes corresponding to low poloidal mode number and to the perturbation's toroidal mode number – in this case $N = 8$ – and its first harmonics develop with a strong amplitude. These modes correspond mainly to the coupling of the $(M = 0, N = \pm 8)$ modes of the perturbation with the $(M = \pm 1, N = 0)$ modes corresponding to the poloidal variation of the magnetic field.

The effect of toroidal field ripple can also be identified in terms of heat transport, by considering the time evolution of the neoclassical ion heat diffusivity, averaged over 20% of the radial domain, near the center of the simulation. The result is shown in Fig. 6.4a for

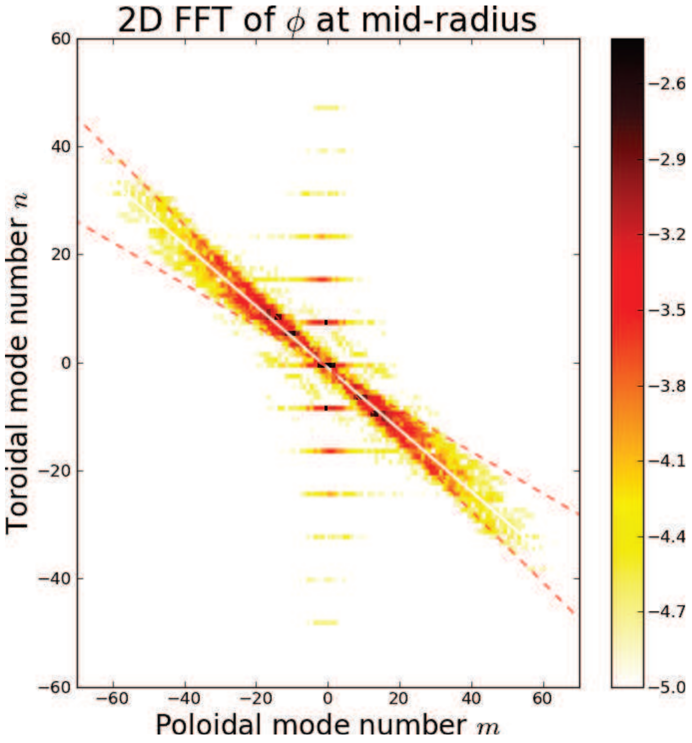

Figure 6.3: Two-dimensional Fast Fourier Transform (FFT) of the electric potential at mid-radius in the presence of a toroidal field ripple with $\delta = 2.10^{-2}$ and $N = 8$. The colors represent the logarithm of the amplitude for each (m, n) mode. The white line corresponds to the local resonance $m/n = -q$, while the dashed red lines correspond to the resonance computed from the minimum and maximum values of q in the simulation domain.

the different ripple amplitudes considered and, for comparison, in the absence of ripple. In the case without ripple, the heat diffusivity oscillates near the value predicted by standard – i.e., axisymmetric – neoclassical theory in the banana regime [Tag88], as previously verified in GYSELA simulations [DPDG+11]. In the presence of ripple, as expected from the theoretical predictions in section 6.3, the neoclassical ion heat diffusivity increases with toroidal field ripple.

When adding toroidal field ripple to the simulation, a rapid transient phase is observed due to the modification of the neoclassical equilibrium in the simulation. This transient is similar to what has been reported in gyrokinetic simulations when the initial state is not an equilibrium solution of the equation, such as when initializing the distribution function with a local Maxwellian rather than a "canonical" Maxwellian, i.e. a function of the motion invariants [ITK03]. This transient is not expected to modify the transport on longer time-scales [DPGS+08]. Notice that, at the moment, the various simulations have not been run for the same duration. This is due to the significant numerical cost of such simulations: as an example, to obtain a simulation time of $7.10^4 \omega_c^{-1}$, a run of 24 hours on 8192 processors is required, corresponding to nearly 2.10^5 hours of computing time[4]. However, the results presented here are enough to obtain a qualitative observation of the interplay between neoclassical and turbulent momentum transport, and to study

---

[4] The simulations were performed on the *Curie* supercomputer of the Très Grand Centre de Calcul (TGCC) in Bruyères-le-Châtel, France.

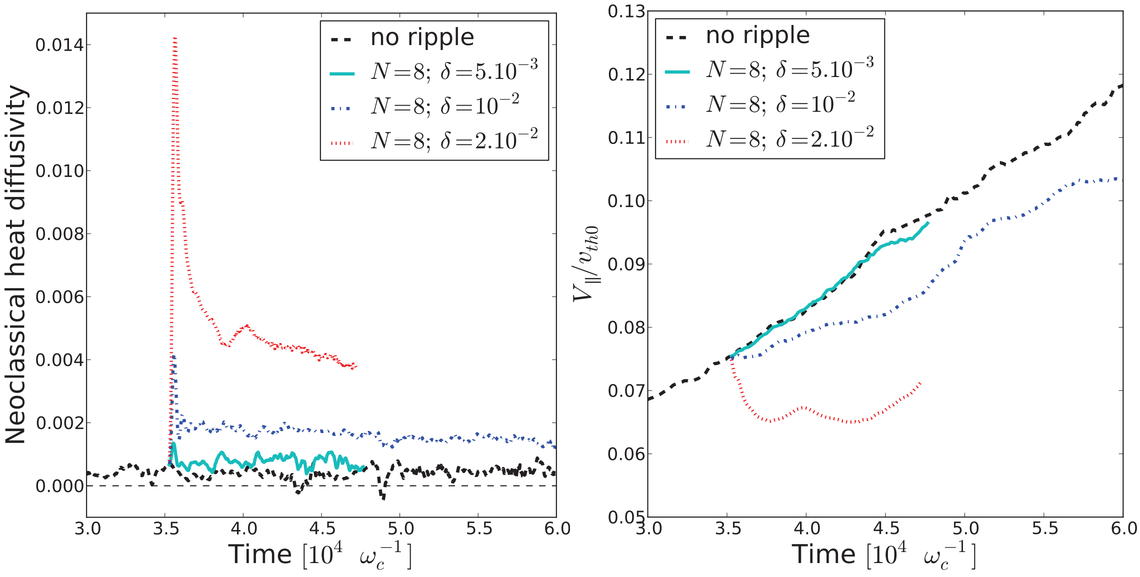

(a) (b)

Figure 6.4: Time evolution of the (a) neoclassical heat diffusivity and (b) parallel velocity, averaged over a large radial domain, without ripple and for different cases of toroidal field ripple, depending on the perturbation amplitude δ.

the trends with varying ripple amplitude.

To analyze the effect of ripple on toroidal rotation, we consider the time evolution of the velocity, also averaged over 20% of the radial domain, near the center of the simulation. As the simulation was run on a time shorter than the confinement time, the mean flows are still evolving. Therefore, the simulations in the presence of ripple must be compared to the same simulation without adding the perturbation. The result is shown in Fig. 6.4b. A first observation is that in the case with the weakest ripple amplitude, $\delta = 5.10^{-3}$, the mean velocity is *not* affected by the presence of ripple. When increasing the perturbation to $\delta = 10^{-2}$, although the velocity continues to increase, the rate of increase is not as fast as in the case without ripple. With this realistic value of toroidal field ripple, it appears that neoclassical momentum transport *can* compete with the contribution from electrostatic turbulence. Furthermore, for $\delta = 2.10^{-2}$, the friction from toroidal field ripple appears sufficient to counter the generation of toroidal rotation by turbulence.

As a conclusion, we find that these results are consistent with recent experimental results on Tore Supra [FGT+11], where the measured rotation was in the co-current direction for small values of toroidal field ripple (down to 0.5%), while it approached the – counter-current – neoclassical prediction for the highest ripple achievable by the tokamak (up to 5.5%). Quantitative comparisons between Gysela simulations and Tore Supra experiments could be performed in the future, although several ingredients are still missing in the model, such as realistic radial profiles for the collisionality and ripple amplitude. Experimental density and temperature profiles should also be used in the simulations in order to obtain a consistent amplitude for the neoclassical and turbulent contributions to the generation of toroidal rotation.

Chapter 7

Conclusions

Understanding and predicting toroidal momentum transport in tokamaks is an important challenge on the path to using nuclear fusion as a source of energy. The level and profile of toroidal rotation can significantly impact the energy confinement time, which describes the quality of the energy confinement in the plasma and is a key parameter in view of obtaining an economically viable fusion reactor. This issue will become specifically critical for future devices such as ITER as external sources will play a minor role. *Intrinsic* toroidal rotation has been observed experimentally in present tokamaks, in the absence of sources, but the physical mechanisms governing its generation are not entirely understood. Thus, reliable predictions for future experiments are lacking. In this thesis, we studied **the generation of intrinsic toroidal rotation by electrostatic turbulence and collisional effects**. Because tokamak plasmas are not in thermodynamic equilibrium, studying such collective processes requires the use of a kinetic model to model the distribution of particles in phase-space. The presence of a strong magnetic field allows us to reduce this six-dimensional phase-space to five dimensions, leading to the **gyrokinetic model** used in this thesis.

In the context of this reduced model, we derived exact local conservation laws for charge density, energy and toroidal momentum. The latter is particularly important as it demonstrates that the gyrokinetic model can accurately describe the transport of toroidal momentum, and provides the framework for this description by identifying the key contributions, most notably the toroidal component of the Reynolds stress. This conservation law was verified numerically with the global, full-f gyrokinetic code GYSELA. Combining the conservation of toroidal momentum with an equation for polarization, which can be interpreted as the momentum carried by the electromagnetic field, we obtain an equation for the *total* momentum. Along with the force balance equation, which is also verified numerically in GYSELA, this provides a complete description of mean flows in tokamaks.

A corollary to the conservation equation of toroidal angular momentum is that the generation of toroidal rotation requires a breaking of axisymmetry. Electrostatic turbulence is found to provide this symmetry breaking and can generate toroidal rotation in simulations with a vanishing initial rotation profile and no momentum source. This rotation, governed by the turbulent Reynolds stress, initially exhibits a dipolar structure due to the conservation properties. Eventually, the diffusion of momentum fluxes at the edge of the simulation allows for a *net* generation of toroidal rotation. Turbulent transport exhibits large-scale avalanche-like events, which are found to transport large quantities of both heat and momentum transport. In the statistical steady-state of the simulation, turbulent heat and momentum transport are found to be strongly correlated. Moreover, their dynamics – measured in terms of probability distribution functions – are remarkably similar.

We also explored possible non-local effects in turbulent heat and momentum transport. An important observation is that the description of turbulence strongly depends on the spatial and temporal scales considered. On the one hand, in addition to the intermittency observed in the flux-surface averaged turbulence, the fluxes are found to be strongly localized in the poloidal direction on the low-field side (LFS) of the tokamak, and the dynamics on the LFS and high-field side (HFS) show significant differences. On the other hand, when performing averages in the radial and temporal dimensions, in addition to the flux-surface average, one can recover the scaling expected from gyro-Bohm estimates for both heat and momentum transport, which correspond to the assumptions of a purely local and diffusive transport. This apparent contradiction suggests the existence of a meso-scale, larger than the turbulence correlation length but smaller than the system size, limiting the radial extent of the avalanches. Another feature which suggests that a purely local description of turbulence is not satisfactory is the dependence of core toroidal rotation on flows in the scrape-off layer. This was investigated through modified boundary conditions in GYSELA simulations, including poloidally inhomogeneous edge flows.

Apart from electrostatic turbulence, another means of breaking the axisymmetry in tokamaks is via the equilibrium magnetic field. In all tokamaks, the finite number of toroidal field coils leads to toroidal field ripple, i.e. variations of the magnetic field in the toroidal direction. Other non-axisymmetric magnetic fields are also possible, such as Resonant Magnetic Perturbations. Through purely collisional processes, in the absence of turbulence, a non-axisymmetric magnetic field modifies the neoclassical equilibrium, and in particular leads to a friction of the toroidal rotation. This friction, and the resulting (counter-current) rotation, can be computed for a number of limit cases through the extremalization of the entropy production rate. By implementing toroidal field ripple as a perturbation to the Hamiltonian in GYSELA, the competition between the neoclassical friction and the turbulent generation of intrinsic toroidal rotation can be investigated. For low values of the perturbation amplitude, toroidal rotation is not affected by ripple. For higher ripple, neoclassical effects can compete with turbulent momentum transport, as observed experimentally in Tore Supra.

Directions for future work

The issue of toroidal momentum transport in tokamaks is far from resolved. The model used in the present study is based on a number of approximations which limit the scope of physics that can be addressed, excluding for example electron turbulence or MHD modes. The effect of *extrinsic* momentum sources, for instance by neutral beam injection or radio-frequency heating, and its interaction with intrinsic momentum transport, also raises some difficult questions. However, rather than going through a (long) list of open issues, we focus here on three important aspects: the interaction between core and edge momentum transport, the comparison between simulations and experiments, and the search for a "minimal model" of tokamak turbulence.

As mentioned throughout this thesis, the conservation of toroidal momentum implies that edge physics can have a significant impact on core toroidal rotation, and a more consistent treatment of the effect of the edge on core rotation than was presented here appears mandatory. Rather than a question of boundary conditions in gyrokinetic codes, one should consider this issue as one of interaction. For instance, the structure of scrape-off layer flows is intricately linked with the ballooning of turbulent transport, and the properties of turbulence in the core and in the SOL cannot be decoupled. As the appropriate models and relevant scales for edge and core modeling are significantly different, such effects could be investigated through, for example, the coupling of a core gyrokinetic code to a fluid simulation for the edge.

A second issue which should be addressed in the future is the comparison of gyrokinetic simulations with experimental results. In terms of toroidal momentum transport, gyrokinetic codes such as GYSELA can now take into account self-consistently the turbulent and neoclassical contributions, and the first results presented here have shown good qualitative agreement. With a proper coupling to a model for the edge rotation, the key ingredients should be present for a quantitative comparison with experimental results, at least in situations where the effects of fast particles and MHD can be neglected. Such comparisons would represent an important step in the validation of the underlying theoretical and numerical models, thus allowing for these models to be used for reliable predictions of intrinsic rotation in future experiments. More generally, the observation in numerical simulations of intermittent, non-local turbulent transport raises questions in terms of the quantities of interest when comparing simulations and experiments. It appears that conventional comparisons through averaged quantities such as diffusion coefficients may be misleading, and more significant measurements, perhaps focusing on detailed characteristics of the fluctuations, must be be considered. Ideally, this should be achieved by simultaneously improving the resolution of experimental diagnostics and implementing *synthetic* diagnostics in numerical codes.

Finally, an issue which goes beyond the question of momentum transport but could lead to significant advances in the study of plasma turbulence is that of the importance of kinetic effects in electrostatic turbulence, and whether an adequate reduction can be found which reproduces these effects. As mentioned in the introduction, tokamak plasmas are not in thermodynamic equilibrium, and fluid models assuming this equilibrium systematically fail to reproduce experimental observations. Indeed, the distribution functions obtained in kinetic simulations of electrostatic turbulence such as presented in this thesis are clearly non-Gaussian. As a result, a dominant trend in plasma physics at the moment is to perform ever more costly numerical simulations, using the constantly increasing numerical resources of modern supercomputers. This increase in computer cost – which is not without a significant cost in terms of energy – allows us to progressively enrich the physics content of gyrokinetic simulations, by including the effects of impurities, kinetic electrons, magnetic geometry, electromagnetic turbulence, etc. However, a different approach should also be considered, where kinetic simulations are not only the ends but also the means to explicitly identify – for instance through comparisons with fluid simulations – the kinetic effects, in view of reducing the model. Current simulations seem to indicate that a conventional fluid approach will not be sufficient, but a careful study of gyrokinetic simulations could help identify a “minimal model” capable of reproducing the properties of turbulence in tokamak plasmas.

Appendix A

Toroidal flux coordinates

A.1 Deriving straight field-line coordinates

The aim of this section is to derive a set of toroidal flux coordinates, i.e. coordinates in which the magnetic field lines are straight lines on a given flux-surface. We assume as a starting point that the magnetic field **B** is known for an arbitrary set of coordinates $(\rho, \hat{\theta}, \hat{\varphi})$ where the radial variable ρ is a flux-surface label and the angles $\hat{\theta}$ and $\hat{\varphi}$ are the "geometric" angles. The orientation of these angles is important in order to determine details of the metric, in particular the sign of the Jacobian. Here, we choose the toroidal angle $\hat{\varphi}$ in the counterclockwise direction and the poloidal angle $\hat{\theta}$ in the clockwise direction. We use the notation $\hat{\theta}$ and $\hat{\varphi}$ to distinguish from the straight field line coordinates θ and φ used throughout the thesis, which will be derived here. Conventional covariant and contravariant notations are adopted in the following.

First of all, a label of flux surfaces must be chosen[1]. A number of choices can be considered [DHCS91], but a convenient solution is to use the opposite of the poloidal flux of the magnetic field

$$\chi \equiv -\psi_{pol}(\chi) = -\frac{1}{2\pi} \int_{S_{\hat{\theta}}} dS \, \mathbf{B} \cdot \frac{\nabla\hat{\theta}}{|\nabla\hat{\theta}|} \tag{A.1}$$

where $S_{\hat{\theta}}$ is the ribbon-like surface stretched between the magnetic axis and the flux surface at a given value of $\hat{\theta}$. We use the opposite of the poloidal magnetic flux – rather than ψ_{pol} itself – as a flux-surface label because it increases with the radius.

Flux surfaces can then be defined simply by the equation $\mathbf{B} \cdot \nabla\chi = 0$. Thus, in contravariant coordinates, the expression of the magnetic field is

$$\mathbf{B} = B^{\hat{\theta}} \sqrt{g} \nabla\hat{\varphi} \times \nabla\chi + B^{\hat{\varphi}} \sqrt{g} \nabla\chi \times \nabla\hat{\theta} \tag{A.2}$$

where g is the determinant of the metric tensor for the system of coordinates $(\chi, \hat{\theta}, \hat{\varphi})$. From the relation $\nabla \cdot \mathbf{B} = 0$, one can write

$$\partial_{\hat{\theta}} \left(\sqrt{g} B^{\hat{\theta}} \right) + \partial_{\hat{\varphi}} \left(\sqrt{g} B^{\hat{\varphi}} \right) = 0 \tag{A.3}$$

The two components of the magnetic field can then be expressed as a function of a single

---

[1] Note that we only consider cases where flux surfaces *exist*. The following cannot be applied in the case of a chaotic magnetic field, where flux surface labels are not defined.

variable $v(\chi, \hat{\theta}, \hat{\varphi})$

$$B^{\hat{\theta}} = -\frac{1}{\sqrt{g}}\partial_{\hat{\varphi}} v \tag{A.4}$$

$$B^{\hat{\varphi}} = \frac{1}{\sqrt{g}}\partial_{\hat{\theta}} v \tag{A.5}$$

Therefore, since $\nabla\chi \times \nabla\chi = 0$, Eq. (A.2) becomes

$$\mathbf{B} = \nabla\chi \times \nabla v \tag{A.6}$$

From this expression of the magnetic field, it appears that the equation for a magnetic field line on a given flux surface is $v =$ constant. Furthermore, as $\mathbf{B}$ is periodic in $(\hat{\theta}, \hat{\varphi})$, ∇v must also be periodic in $(\hat{\theta}, \hat{\varphi})$. The general form of v is

$$v = \alpha(\chi)\hat{\theta} + \beta(\chi)\hat{\varphi} + \tilde{v}(\chi, \hat{\theta}, \hat{\varphi}) \tag{A.7}$$

where $\tilde{v}$ is periodic in $(\hat{\theta}, \hat{\varphi})$. From the expressions of the contravariant components of $\mathbf{B}$, the functions α and β can be straightforwardly obtained as functions of the poloidal and toroidal fluxes of the magnetic field

$$\alpha = -\frac{\mathrm{d}\psi_{tor}}{\mathrm{d}\chi} \tag{A.8}$$

$$\beta = \frac{\mathrm{d}\psi_{pol}}{\mathrm{d}\chi} \tag{A.9}$$

where the poloidal flux ψ_{pol} is defined in Eq. (A.1) and the toroidal flux ψ_{tor} is

$$\psi_{tor} = \frac{1}{2\pi}\int_{S_{\hat{\varphi}}} dS\, \mathbf{B}\cdot\frac{\nabla\hat{\varphi}}{|\nabla\hat{\varphi}|} \tag{A.10}$$

where $S_{\hat{\varphi}}$ is a surface of constant $\hat{\varphi}$ bounded by a given flux surface. In order for magnetic field lines to be straight in a given set of coordinates, one needs $\tilde{v} = 0$. This can be achieved by a change of coordinates, for instance

$$\theta = \hat{\theta} - \tilde{v}\left(\frac{\mathrm{d}\psi_{tor}}{\mathrm{d}\chi}\right)^{-1} \quad \text{and} \quad \varphi = \hat{\varphi} \tag{A.11}$$

For a simple magnetic field geometry, the angle θ can expressed or computed as a function of $\hat{\theta}$. An example is given in Fig. A.1 for the case of concentric, circular magnetic flux surfaces, corresponding to the geometry used in GYSELA, with an aspect ration $R/a = 3.2$. One can note that surfaces of constant θ (solid blue lines) can significantly deviate from surfaces of constant $\hat{\theta}$ (dashed black).

In the new flux coordinates (χ, θ, φ), the equation of a magnetic field line is

$$\frac{\mathrm{d}\psi_{tor}}{\mathrm{d}\chi}\theta - \frac{\mathrm{d}\psi_{pol}}{\mathrm{d}\chi}\varphi = \text{constant} \tag{A.12}$$

which corresponds to a straight line. A convenient expression of $\mathbf{B}$ is obtained from Eq. (A.6) as

$$\mathbf{B} = \nabla\chi \times \nabla\left(q\theta - \varphi\right) \tag{A.13}$$

where the safety factor q is a flux function defined as

$$q \equiv -\frac{\mathrm{d}\psi_{tor}}{\mathrm{d}\chi} = \frac{B^{\varphi}}{B^{\theta}} \tag{A.14}$$

The choice of the variable χ – rather than the poloidal flux – ensures that the coordinate system (χ, θ, φ) is direct and the safety factor positive.

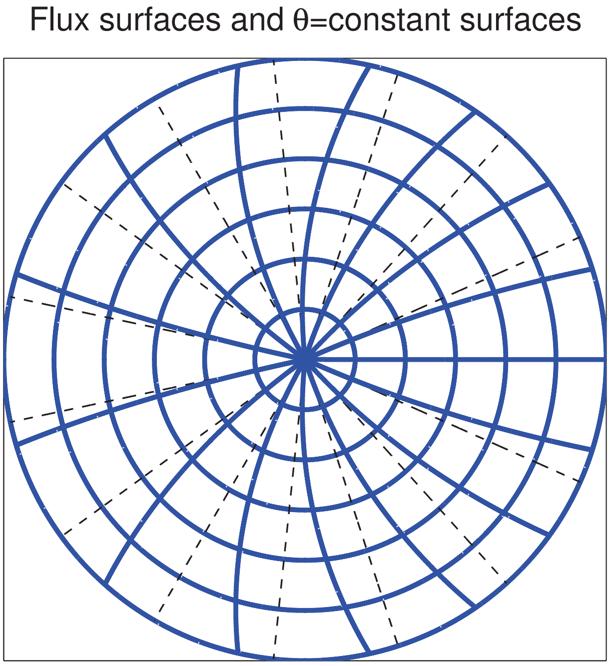

Figure A.1: Poloidal cross-section showing flux surfaces and contours of $\theta = constant$ (solid blue lines) and $\hat{\theta} = constant$ (dashed black lines) surfaces, in the case of circular concentric flux surfaces.

A.2 Properties of the system of coordinates

For the coordinate system (r, θ, φ), which is also direct, the metric tensor is

$$g^{ij} = \begin{pmatrix} |\nabla r|^2 & \nabla r \cdot \nabla\theta & 0 \\ \nabla r \cdot \nabla\theta & |\nabla\theta|^2 & 0 \\ 0 & 0 & \frac{1}{R^2} \end{pmatrix} \tag{A.15}$$

In the special case of circular concentric surfaces, $\nabla r \cdot \nabla\theta = 0$ and the metric tensor is diagonal. The Jacobian of the metric is defined as $\mathcal{J}_s^{-1} = (\nabla r \times \nabla\theta) \cdot \nabla\varphi = \sqrt{g}$ where g is the determinant of the metric tensor. Here, the Jacobian reads

$$\mathcal{J}_s = \frac{1}{\mathbf{B} \cdot \nabla\theta} \tag{A.16}$$

In the circular concentric case, the contravariant and covariant components of the magnetic field can be expressed as

$$\begin{aligned} B^r &= 0, & B^\theta &= \mathcal{J}_s^{-1}, & B^\varphi &= I/R^2 \\ B_r &= 0, & B_\theta &= g^{rr}\mathcal{J}_s/R^2, & B_\varphi &= I \end{aligned}$$

Appendix B

Derivation of the gyrokinetic quasi-neutrality equation

B.1 General expression

The aim of this section is to derive the gyrokinetic quasi-neutrality equation, as given by equation (2.14). We recall the general form of the quasi-neutrality equation (2.10), which is the starting point of the derivation

$$\sum_{species} n_s e_s = 0 \tag{B.1}$$

This equation contains the density of particles for each species. The main difficulty lies in expressing this *particle* density as a function of the *gyrocenter* distribution $\bar{F}_s$.

The derivation of such relation is not trivial. In particular, the difference between positions in particle phase-space and in guiding-center phase-space, which have been left out for simplicity in the description of the model, must be taken into account. When considering the canonical transformation between the particle variables $(\mathbf{x}, \mathbf{v})$ and the guiding-center variables $(\mathbf{x}_G, \mathbf{v}_G)$, one finds [BH07, GS] the following relation between the distribution functions of particles and guiding-centers

$$F(\mathbf{x}, \mathbf{v}, t) = \bar{F}(\mathbf{x}_G, \mathbf{v}_G, t) + \frac{e}{B}\left\{\phi(\mathbf{x}, t) - \bar{\phi}(\mathbf{x}_G, \mathbf{v}_G, t)\right\}\partial_\mu \bar{F}_{eq}(\mathbf{x}_G, \mathbf{v}_G) \tag{B.2}$$

in the electrostatic approximation considered here. The species subscript s has been omitted in equation (B.2) and in the following, as the density is computed independently for each species. Thus the particle density in equation (B.1) can be written

$$\begin{aligned} n(\mathbf{x}, \mathbf{v}, t) = &\int \mathrm{d}^3\mathbf{v}\, \bar{F}(\mathbf{x}_G, \mathbf{v}_G, t) \\ &+ \int \mathrm{d}^3\mathbf{v} \frac{e}{B}\left\{\phi(\mathbf{x}, t) - \bar{\phi}(\mathbf{x}_G, \mathbf{v}_G, t)\right\}\partial_\mu \bar{F}_{eq}(\mathbf{x}_G, \mathbf{v}_G) \end{aligned} \tag{B.3}$$

The difference between particle position and guiding-center position is $\mathbf{x} - \mathbf{x}_G = \boldsymbol{\rho}_c$ where we recall that $\boldsymbol{\rho}_c$ is the gyro-radius vector. The density can then be decomposed as

$n = n_G + n_{pol}$, and we find

$$\begin{aligned} n_G(\mathbf{x}) &= \int \mathcal{J}_v \mathrm{d}\mu \mathrm{d}v_{G\parallel} J \cdot \bar{F} && \text{(B.4)} \\ n_{pol}(\mathbf{x}) &= \int \mathcal{J}_v \mathrm{d}\mu \mathrm{d}v_{G\parallel} \frac{e}{B} \int_0^{2\pi} \frac{\mathrm{d}\alpha}{2\pi} e^{-\boldsymbol{\rho}_c \cdot \nabla} \partial\mu \bar{F}_{eq}(\mathbf{x},\mathbf{v}) \\ & \qquad \left\{ \phi(\mathbf{x},\mathbf{v}) - e^{-\boldsymbol{\rho}_c \cdot \nabla} \left\langle e^{\boldsymbol{\rho}_c \cdot \nabla} \right\rangle \phi(\mathbf{x},\mathbf{v}) \right\} && \text{(B.5)} \end{aligned}$$

where we recall that J is the gyro-averaging operator and α is the gyro-angle. The brackets $\langle \ldots \rangle$ correspond to the average over the gyro-angle, i.e. $\int_0^{2\pi} \mathrm{d}\alpha/(2\pi)$

Equation (B.5) is the exact expression of the polarization density. Note that the integrand is related to variations of the electric potential at the scale of the Larmor radius. However, this expression for the polarization density is extremely difficult to compute in a numerical code. In practice, it is most often replaced by an approximation in the long wavelength limit, $k_\perp \rho_c \ll 1$, which will be derived in the following section.

B.2 Polarization density in the long wavelength limit

Because the Larmor radius depends on the local direction and value of the magnetic field, the change from particle position to guiding-center position is not a straightforward bijection, and both directions correspond to different expressions:

$$\begin{aligned} \mathbf{x} \to \mathbf{x}_G : \quad & \mathbf{x} = \mathbf{x}_G + \boldsymbol{\rho}_c(\mathbf{x}) && \text{(B.6)} \\ \mathbf{x}_G \to \mathbf{x} : \quad & \mathbf{x}_G = \mathbf{x} - \boldsymbol{\rho}_c(\mathbf{x}_G) && \text{(B.7)} \end{aligned}$$

where the gyro-radius vectors $\boldsymbol{\rho}_c$ at the positions $\mathbf{x}$ and $\mathbf{x}_G$ are different. Using a Taylor expansion, we can write this difference as

$$\boldsymbol{\rho}_c(\mathbf{x}_G) \simeq \boldsymbol{\rho}_c(\mathbf{x}) + (\boldsymbol{\rho}_c \cdot \nabla)\, \boldsymbol{\rho}_c \qquad \text{(B.8)}$$

With this approximation, we can expand the operators in equation (B.5) as

$$\begin{aligned} e^{\boldsymbol{\rho}_c \cdot \nabla} &\simeq 1 + \boldsymbol{\rho}_c \cdot \nabla + \frac{1}{2} (\boldsymbol{\rho}_c \cdot \nabla)^2 && \text{(B.9)} \\ e^{-\boldsymbol{\rho}_c \cdot \nabla} &\simeq 1 - \boldsymbol{\rho}_c \cdot \nabla + \{(\boldsymbol{\rho}_c \cdot \nabla)\, \boldsymbol{\rho}_c\} \cdot \nabla + \frac{1}{2} (\boldsymbol{\rho}_c \cdot \nabla)^2 && \text{(B.10)} \end{aligned}$$

where all quantities are now expressed at the position $\mathbf{x}$. This allows us to rewrite the polarization density equation (B.5) as

$$\begin{aligned} n_{pol}(\mathbf{x}) = \int \mathcal{J}_v \mathrm{d}\mu \mathrm{d}v_{G\parallel} \frac{e}{B} \int_0^{2\pi} \frac{\mathrm{d}\alpha}{2\pi} (1 - \boldsymbol{\rho}_c \cdot \nabla)\, \partial\mu F_{eq} & \\ \left\{ 1 - \left[1 - \boldsymbol{\rho}_c \cdot \nabla + \{(\boldsymbol{\rho}_c \cdot \nabla)\, \boldsymbol{\rho}_c\} \cdot \nabla + \frac{1}{2} (\boldsymbol{\rho}_c \cdot \nabla)^2 \right] \right. & \\ \left. \left\langle 1 + \boldsymbol{\rho}_c \cdot \nabla + \frac{1}{2} (\boldsymbol{\rho}_c \cdot \nabla)^2 \right\rangle \right\} \phi & \qquad \text{(B.11)} \end{aligned}$$

Since the brackets correspond to the average over the gyro-angle, $\langle \boldsymbol{\rho}_c \cdot \nabla \rangle = 0$. At second order in $k \perp \rho_c$, the polarization density reads

$$
\begin{aligned}
n_{pol}(\mathbf{x}) = & \int \mathcal{J}_v \mathrm{d}\mu \mathrm{d}v_{G\parallel} \frac{e}{B} \int_0^{2\pi} \frac{\mathrm{d}\alpha}{2\pi} \left(1 - \boldsymbol{\rho}_c \cdot \nabla\right) \partial \mu F_{eq} \\
& \left\{ \boldsymbol{\rho}_c \cdot \nabla - \left(\left(\boldsymbol{\rho}_c \cdot \nabla\right) \boldsymbol{\rho}_c\right) \cdot \nabla - \frac{1}{2} \left(\boldsymbol{\rho}_c \cdot \nabla\right)^2 - \left\langle \frac{1}{2} \left(\boldsymbol{\rho}_c \cdot \nabla\right)^2 \right\rangle \right\} \phi \\
= & \int \mathcal{J}_v \mathrm{d}\mu \mathrm{d}v_{G\parallel} \frac{e}{B} \Bigg\langle \partial_\mu \bar{F} \left\{ - \left(\left(\boldsymbol{\rho}_c \cdot \nabla\right) \boldsymbol{\rho}_c\right) \cdot \nabla - \frac{1}{2} \left(\boldsymbol{\rho}_c \cdot \nabla\right)^2 - \left\langle \frac{1}{2} \left(\boldsymbol{\rho}_c \cdot \nabla\right)^2 \right\rangle \right\} \bar{\phi} \\
& - \left(\boldsymbol{\rho}_c \cdot \nabla \partial_\mu \bar{F}\right) \left(\boldsymbol{\rho}_c \cdot \nabla \bar{\phi}\right) \Bigg\rangle
\end{aligned}
\tag{B.12}
$$

The gyro-average of the various operators in this equation can be computed by projecting the gyro-radius $\boldsymbol{\rho}_c$ on a Cartesian basis in the plane perpendicular to the magnetic field, as $\boldsymbol{\rho}_c = \rho_c \left(\cos \alpha \mathbf{e}_{\perp 1} + \sin \alpha \mathbf{e}_{\perp 2}\right)$ where $\mathbf{e}_{\perp 1}$ and $\mathbf{e}_{\perp 2}$ are the two vectors of the basis and $\boldsymbol{\rho}_c$ is the norm of the gyro-radius. With this projection, straightforward calculations lead to

$$
\begin{aligned}
\left\langle \left(\boldsymbol{\rho}_c \cdot \nabla\right)^2 \right\rangle &= \frac{1}{2} \rho_s \nabla_\perp \cdot \left(\rho_s \nabla_\perp\right) \\
\left\langle \left(\left(\boldsymbol{\rho}_c \cdot \nabla\right) \boldsymbol{\rho}_s\right) \cdot \nabla \right\rangle &= \frac{1}{4} \left(\nabla_\perp \rho_s^2\right) \cdot \nabla_\perp \\
\left\langle \left(\boldsymbol{\rho}_c \cdot \nabla \partial_\mu \bar{F}\right) \left(\boldsymbol{\rho}_c \cdot \nabla \bar{\phi}\right) \right\rangle &= \frac{1}{2} \rho_s^2 \nabla_\perp \bar{\phi} \cdot \nabla_\perp \partial_\mu \bar{F}
\end{aligned}
$$

This leads to

$$
\begin{aligned}
n_{pol}(\mathbf{x}) = - \int \mathcal{J}_v \mathrm{d}\mu \mathrm{d}v_{G\parallel} \frac{e}{B} \Big\{ & \partial_\mu \bar{F} \left[\frac{1}{4} \nabla_\perp \rho_s^2 \nabla_\perp \bar{\phi} + \frac{1}{4} \rho_s \nabla_\perp \cdot \left(\rho_s \nabla_\perp \bar{\phi}\right) \right] \\
& + \frac{1}{2} \rho_s^2 \nabla_\perp \bar{\phi} \cdot \nabla_\perp \partial_\mu \bar{F} \Big\}
\end{aligned}
$$

With the relation $\rho_s \nabla_\perp \cdot \left(\rho_s \nabla_\perp \bar{\phi}\right) = \rho_s^2 \nabla_\perp^2 \bar{\phi} + \frac{1}{2} \nabla_\perp \rho_s^2 \nabla_\perp \bar{\phi}$, we can rewrite this as

$$
\begin{aligned}
n_{pol}(\mathbf{x}) &= - \int \mathcal{J}_v \mathrm{d}\mu \mathrm{d}v_{G\parallel} \frac{e}{2B} \left\{ \nabla_\perp \rho_s^2 \cdot \nabla_\perp \bar{\phi} + \rho_s^2 \nabla_\perp^2 \bar{\phi} + \rho_s^2 \nabla_\perp \bar{\phi} \cdot \nabla_\perp \right\} \partial_\mu \bar{F} \\
&= \int \mathcal{J}_v \mathrm{d}\mu \mathrm{d}v_{G\parallel} \frac{e}{2B} \partial_\mu \left\{ \nabla_\perp \rho_s^2 \cdot \nabla_\perp \bar{\phi} + \rho_s^2 \nabla_\perp^2 \bar{\phi} + \rho_s^2 \nabla_\perp \bar{\phi} \cdot \nabla_\perp \right\} \bar{F}
\end{aligned}
\tag{B.13}
$$

To complete the calculation, we use the fact that the operator $B^{-1} \partial_\mu = (m v_\perp)^{-1} \partial_{v_\perp}$ commutes with the operator $\nabla_\perp$, which also commutes with the integral in velocity space $\int \mathcal{J}_v \mathrm{d}\mu$. Finally, recalling the expression of the Larmor radius, we can use the expression $\partial_\mu \rho_s^2 = 2m/(e^2 B)$. We find

$$
\begin{aligned}
n_{pol}(\mathbf{x}) &= \int \mathcal{J}_v \mathrm{d}\mu \mathrm{d}v_{G\parallel} \nabla_\perp \cdot \left(\frac{m}{eB^2} \bar{F} \nabla_\perp \bar{\phi} \right) \\
&= \nabla_\perp \cdot \int \mathcal{J}_v \mathrm{d}\mu \mathrm{d}v_{G\parallel} \frac{m}{eB^2} \bar{F} \nabla_\perp \bar{\phi} \\
&= \nabla_\perp \cdot \left(\frac{nm}{eB^2} \nabla_\perp \bar{\phi} \right)
\end{aligned}
\tag{B.14}
$$

Appendix C

Deriving the reference Maxwellian for the collision operator

We recall the expression of the collision operator used in GYSELA:

$$\mathcal{C}(\bar{F}) = \frac{1}{B_{\|}^{*}}\partial_{v_{G\|}}\left\{B_{\|}^{*}D_{\|}F_{M}\partial_{\mu}\left(\frac{\bar{F}}{F_{M}}\right)\right\} \tag{C.1}$$

where the reference Maxwellian F_M is defined by its two moments T_{coll} and $V_{\|coll}$

$$F_{M} = n\left(\frac{m}{T_{coll}}\right)^{3/2}\exp\left\{-\frac{m\left(v_{G\|}-V_{\|coll}\right)^{2}}{T_{coll}} - \frac{\mu B}{T_{coll}}\right\} \tag{C.2}$$

This collision operator (C.1) trivially conserves the number of particles. The conservations of parallel momentum and energy impose

$$\int\frac{B_{\|}^{*}}{m}\mathrm{d}\mu\mathrm{d}v_{G\|}\; m v_{G\|}\mathcal{C}(\bar{F}) = 0 \tag{C.3}$$

$$\int\frac{B_{\|}^{*}}{m}\mathrm{d}\mu\mathrm{d}v_{G\|}\left(\frac{1}{2}m{v_{G\|}}^{2}+\mu B\right)\mathcal{C}(\bar{F}) = 0 \tag{C.4}$$

Let us first consider only the contribution of collisions in the parallel direction. We use the expression of the collision operator (C.1) and integrate Eq.(C.3) by parts twice in the variable $v_{G\|}$

$$\begin{aligned}
(\text{C.3})_{\|} &= \int\frac{B_{\|}^{*}}{m}\mathrm{d}\mu\mathrm{d}v_{G\|}\; m v_{G\|}\frac{1}{B_{\|}^{*}}\partial_{v_{G\|}}\left\{B_{\|}^{*}D_{\|}F_{M}\partial_{v_{G\|}}\left(\frac{\bar{F}}{F_{M}}\right)\right\}\\
&= -\int\mathrm{d}\mu\mathrm{d}v_{G\|}\; B_{\|}^{*}D_{\|}F_{M}\partial_{v_{G\|}}\left(\frac{\bar{F}}{F_{M}}\right)\\
&= \int\mathrm{d}\mu\mathrm{d}v_{G\|}\;\frac{\bar{F}}{F_{M}}\partial_{v_{G\|}}(B_{\|}^{*}D_{\|}F_{M})\\
&= \int\mathrm{d}\mu\mathrm{d}v_{G\|}\;\left\{\frac{\bar{F}}{F_{M}}B_{\|}^{*}D_{\|}\partial_{v_{G\|}}F_{M}+\bar{F}\partial_{v_{G\|}}(B_{\|}^{*}D_{\|})\right\}
\end{aligned}$$

Using the fact that $\partial_{v_{G\|}} F_M = -F_M \frac{m(v_{G\|} - V_{\|coll})}{T_{coll}}$, we obtain

$$\begin{aligned}
(\text{C.3})_{\|} &= \frac{1}{T_{coll}} \int B_{\|}^{*} \mathrm{d}\mu \mathrm{d}v_{G\|} \left\{ \frac{T_{coll}\bar{F}}{B_{\|}^{*}} \partial_{v_{G\|}} (B_{\|}^{*} D_{\|}) - D_{\|} \bar{F} m (v_{G\|} - V_{\|coll}) \right\} \\
&= \frac{m}{T_{coll}} \left\{ V_{\|coll} \left\langle m D_{\|} \right\rangle - \left\langle m D_{\|} v_{G\|} \right\rangle + T_{coll} \left\langle \frac{1}{B_{\|}^{*}} \partial_{v_{G\|}} (B_{\|}^{*} D_{\|}) \right\rangle \right\}
\end{aligned} \tag{C.5}$$

where the integration in velocity space is

$$\langle ... \rangle = \int \frac{B_{\|}^{*}}{m} \mathrm{d}\mu \mathrm{d}v_{G\|} \, \bar{F} ... \tag{C.6}$$

We perform similar operations on the contribution to Eq.(C.4) of collisions in the parallel direction:

$$\begin{aligned}
(\text{C.4})_{\|} &= \int \frac{B_{\|}^{*}}{m} \mathrm{d}\mu \mathrm{d}v_{G\|} (\mu B + \frac{1}{2} m {v_{G\|}}^{2}) \frac{1}{B_{\|}^{*}} \partial_{v_{G\|}} \left\{ B_{\|}^{*} D_{\|} F_M \partial_{v_{G\|}} \left(\frac{\bar{F}}{F_M} \right) \right\} \\
&= -\int \mathrm{d}\mu \mathrm{d}v_{G\|} \, B_{\|}^{*} D_{\|} F_M v_{G\|} \partial_{v_{G\|}} \left(\frac{\bar{F}}{F_M} \right) \\
&= \int \mathrm{d}\mu \mathrm{d}v_{G\|} \frac{\bar{F}}{F_M} \partial_{v_{G\|}} (B_{\|}^{*} D_{\|} v_{G\|} F_M) \\
&= \frac{1}{T_{coll}} \int B_{\|}^{*} \mathrm{d}\mu \mathrm{d}v_{G\|} \left\{ -v_{G\|} D_{\|} \bar{F} m (v_{G\|} - V_{\|coll}) + \frac{T_{coll}}{B_{\|}^{*}} \bar{F} \partial_{v_{G\|}} (B_{\|}^{*} v_{G\|} D_{\|}) \right\} \\
&= \frac{m}{T_{coll}} \left\{ V_{\|coll} \left\langle m D_{\|} v_{G\|} \right\rangle - \left\langle m D_{\|} {v_{G\|}}^{2} \right\rangle + T_{coll} \left\langle \frac{1}{B_{\|}^{*}} \partial_{v_{G\|}} (B_{\|}^{*} D_{\|} v_{G\|}) \right\rangle \right\}
\end{aligned} \tag{C.7}$$

For collisions in the perpendicular direction, Eq.(C.3) is trivially verified. We perform two integrations by parts in the variable μ for Eq.(C.4)

$$\begin{aligned}
(\text{C.4})_{\perp} &= \int \frac{B_{\|}^{*}}{m} \mathrm{d}v_{G\|} \mathrm{d}\mu \, (\mu B + \frac{1}{2} m {v_{G\|}}^{2}) \frac{1}{B_{\|}^{*}} \partial_{\mu} \left\{ B_{\|}^{*} D_{\perp} F_M \frac{1}{B^{2}} \partial_{\mu} \left(\frac{\bar{F}}{F_M} \right) \right\} \\
&= -\frac{1}{m} \int \mathrm{d}v_{G\|} \mathrm{d}\mu \, \frac{B_{\|}^{*}}{B} D_{\perp} F_M \partial_{\mu} \left(\frac{\bar{F}}{F_M} \right) \\
&= \frac{1}{m} \int \mathrm{d}v_{G\|} \mathrm{d}\mu \frac{\bar{F}}{F_M} \frac{1}{B} \partial_{\mu} (B_{\|}^{*} D_{\perp} F_M)
\end{aligned}$$

Using the fact that $\partial_{\mu} F_M = -F_M B / T_{coll}$, we obtain

$$\begin{aligned}
(\text{C.4})_{\perp} &= \frac{1}{m} \int \mathrm{d}v_{G\|} \mathrm{d}\mu \, \left\{ \frac{\bar{F}}{B} \partial_{\mu} (B_{\|}^{*} D_{\perp}) - B_{\|}^{*} D_{\perp} \frac{1}{T_{coll}} \bar{F} \right\} \\
&= \frac{1}{T_{coll}} \left\{ \left\langle \frac{1}{B B_{\|}^{*}} \partial_{\mu} (B_{\|}^{*} D_{\perp}) \right\rangle T_{coll} - \left\langle D_{\perp} \right\rangle \right\}
\end{aligned} \tag{C.8}$$

Using Equations (C.5), (C.7) and (C.8), the conservation equations (C.3) and (C.4) form a linear system in $T_{coll}(r,\theta,\varphi)$ and $V_{\|coll}(r,\theta,\varphi)$ as follows

$$\begin{aligned} V_{\|coll}\left\langle mD_{\|}\right\rangle + T_{coll}\left\langle \frac{1}{B_{\|}^{*}}\partial_{v_{G\|}}(B_{\|}^{*}D_{\|})\right\rangle &= \left\langle mD_{\|}v_{G\|}\right\rangle \\ V_{\|coll}\left\langle m^{2}D_{\|}v_{G\|}\right\rangle + T_{coll}\left\langle \frac{m}{B_{\|}^{*}}\partial_{v_{G\|}}(B_{\|}^{*}D_{\|}v_{G\|}) + \frac{1}{BB_{\|}^{*}}\partial_{\mu}(B_{\|}^{*}D_{\perp})\right\rangle &= \left\langle m^{2}D_{\|}{v_{G\|}}^{2} + D_{\perp}\right\rangle \end{aligned}$$

Solving this system, we find that the conservation constraints are verified if the profiles $V_{\|coll}(r,\theta,\varphi)$ and $T_{coll}(r,\theta,\varphi)$ for the collision operator are defined as follows

$$\begin{aligned} mPV_{\|coll} &= \left\langle \frac{m}{B_{\|}^{*}}\partial_{v_{G\|}}(B_{\|}^{*}D_{\|}v_{G\|}) + \frac{1}{BB_{\|}^{*}}\partial_{\mu}(B_{\|}^{*}D_{\perp})\right\rangle \left\langle mD_{\|}v_{G\|}\right\rangle \\ &\quad - \left\langle \frac{1}{B_{\|}^{*}}\partial_{v_{G\|}}(B_{\|}^{*}D_{\|})\right\rangle \left\langle m^{2}D_{\|}{v_{G\|}}^{2} + D_{\perp}\right\rangle \\ PT_{coll} &= \left\langle D_{\|}\right\rangle \left\langle m^{2}D_{\|}{v_{G\|}}^{2} + D_{\perp}\right\rangle - \left\langle mD_{\|}v_{G\|}\right\rangle^{2} \end{aligned}$$

where

$$P = \left\langle D_{\|}\right\rangle \left\langle \frac{m}{B_{\|}^{*}}\partial_{v_{G\|}}(B_{\|}^{*}D_{\|}v_{G\|}) + \frac{1}{BB_{\|}^{*}}\partial_{\mu}(B_{\|}^{*}D_{\perp})\right\rangle - \left\langle mD_{\|}v_{G\|}\right\rangle \left\langle \frac{1}{B_{\|}^{*}}\partial_{v_{G\|}}(B_{\|}^{*}D_{\|})\right\rangle$$

We recall that

$$\langle ... \rangle = \int \frac{B_{\|}^{*}}{m}\mathrm{d}\mu \mathrm{d}v_{G\|}\bar{F}$$

Only collisions in the parallel direction are taken into account at the moment in the code, i.e $D_{\perp} = 0$. In this case, the expressions of the mean velocity and mean temperature are reduced to

$$mPV_{\|coll} = \left\langle \frac{m}{B_{\|}^{*}}\,\partial_{v_{G\|}}\left(B_{\|}^{*}\,v_{G\|}\,D_{\|}\right)\right\rangle \left\langle mD_{\|}v_{G\|}\right\rangle - \left\langle m^{2}D_{\|}{v_{G\|}}^{2}\right\rangle \left\langle \frac{1}{B_{\|}^{*}}\,\partial_{v_{G\|}}\left(B_{\|}^{*}\,D_{\|}\right)\right\rangle \tag{C.9}$$

$$PT_{coll} = \left\langle D_{\|}\right\rangle \left\langle m^{2}D_{\|}{v_{G\|}}^{2}\right\rangle - \left\langle mD_{\|}v_{G\|}\right\rangle^{2} \tag{C.10}$$

$$P = \left\langle D_{\|}\right\rangle \left\langle \frac{m}{B_{\|}^{*}}\,\partial_{v_{G\|}}\left(B_{\|}^{*}\,v_{G\|}\,D_{\|}\right)\right\rangle - \left\langle D_{\|}v_{G\|}\right\rangle \left\langle \frac{m}{B_{\|}^{*}}\,\partial_{v_{G\|}}\left(B_{\|}^{*}\,D_{\|}\right)\right\rangle \tag{C.11}$$

Appendix D

Detailed integrations for the derivation of polarization stresses

In this appendix, we present several detailed calculations useful for the derivation of the gyrokinetic conservation laws in chapter 3.

D.1 Integration for the polarization flux of energy

The aim of this section is to compute the integral

$$\mathcal{I}_E = \frac{m}{2e} \int \mathrm{d}\tau^* \left\{ \partial_t \bar{F} \, \nabla \cdot \left(\frac{\mu}{B} \nabla_\perp \phi \right) - \phi \, \nabla \cdot \left(\frac{\mu}{B} \nabla_\perp \partial_t \bar{F} \right) \right\} \tag{D.1}$$

which corresponds to the polarization flux of energy. In order to perform this integration, it is useful to write the operator $\nabla \cdot (\frac{1}{B^2} \nabla_\perp)$ in covariant notations[1]. We use an approximation of this expression on a poloidal plane, i.e. the direction $\perp$ is actually perpendicular to $\nabla\varphi$ rather than $\mathbf{B}$. Given that $\nabla\varphi \cdot \nabla\theta = \nabla\varphi \cdot \nabla\chi = 0$, we can write in the covariant notations for a given field X:

$$\nabla \cdot \left(\frac{1}{B^2} \nabla X \right) = \frac{1}{\sqrt{g}} \partial_i \left(\frac{\sqrt{g}}{B^2} g^{ij} \partial_j X \right) + \frac{1}{B^2 R^2} \partial_{\varphi\varphi} X \tag{D.2}$$

where i and j correspond to χ or θ, and $\sqrt{g}$ is the Jacobian of the metric tensor. With these notations, the operator we consider is

$$\nabla \cdot \left(\frac{1}{B^2} \nabla_\perp X \right) = \frac{1}{\sqrt{g}} \partial_i \left(\frac{\sqrt{g}}{B^2} g^{ij} \partial_j X \right) \tag{D.3}$$

To perform the integration in a more general case, we consider two arbitrary fields X and Y, corresponding for example to $\partial_t \bar{F}$ and ϕ. We can calculate the integral using an integration by parts on the coordinate i

$$\mathcal{I} \equiv \int \mathrm{d}\chi \mathrm{d}\theta \mathrm{d}\varphi \sqrt{g} X \frac{1}{\sqrt{g}} \partial_i \left(\frac{\sqrt{g}}{B^2} g^{ij} \partial_j Y \right) \tag{D.4}$$

$$= - \int \mathrm{d}\chi \mathrm{d}\theta \mathrm{d}\varphi (\partial_i X) \frac{\sqrt{g}}{B^2} g^{ij} (\partial_j Y) + \int \mathrm{d}\theta \mathrm{d}\varphi X \frac{\sqrt{g}}{B^2} g^{\chi j} (\partial_j Y) \tag{D.5}$$

---

[1] We recall here that μB commutes with the operator ∇.

where i and j are still θ or χ. Because of the periodicity in θ, there is no surface term resulting from the integration by parts on $i = \theta$.

$$\mathcal{I} = -\int \mathrm{d}\chi \mathrm{d}\theta \mathrm{d}\varphi \frac{\sqrt{g}}{B^2} \nabla_\perp X \cdot \nabla_\perp Y + \int \mathrm{d}\theta \mathrm{d}\varphi \frac{\sqrt{g}}{B^2} X \nabla\chi \cdot \nabla_\perp Y \tag{D.6}$$

Notice that $\nabla\chi \cdot \nabla_\perp = \nabla\chi \cdot \nabla$, since $\nabla\varphi \cdot \nabla\chi = 0$. Finally, applying this result to $\mathcal{I}_E$, we find

$$\begin{aligned} \mathcal{I}_E = \ & \frac{m}{2e}\partial_\chi \int \mathrm{d}\tau^* \partial_t \bar{F} \frac{\mu}{B} \nabla\phi \cdot \nabla\chi \quad - \frac{m}{2e} \int \mathrm{d}\tau^* \frac{\mu}{B} (\nabla_\perp \partial_t \bar{F}) \cdot (\nabla_\perp \phi) \\ & - \frac{m}{2e}\partial_\chi \int \mathrm{d}\tau^* \phi \frac{\mu}{B} \nabla(\partial_t \bar{F}) \cdot \nabla\chi + \frac{m}{2e} \int \mathrm{d}\tau^* \frac{\mu}{B} (\nabla_\perp \phi) \cdot (\nabla_\perp \partial_t \bar{F}) \end{aligned} \tag{D.7}$$

D.2 Integration for the momentum polarization flux

The aim of this section is to calculate integrals of the form

$$\begin{aligned} \mathcal{I} &\equiv \int \mathrm{d}\chi \mathrm{d}\theta \mathrm{d}\varphi \sqrt{g} (\partial_\varphi X) \frac{1}{\sqrt{g}} \partial_i \left(\frac{\sqrt{g}}{B^2} g^{ij} \partial_j Y \right) && \text{(D.8)} \\ &= -\int \mathrm{d}\chi \mathrm{d}\theta \mathrm{d}\varphi (\partial^2_{\varphi i} X) \frac{\sqrt{g}}{B^2} g^{ij} (\partial_j Y) + \int \mathrm{d}\theta \mathrm{d}\varphi (\partial_\varphi X) \frac{\sqrt{g}}{B^2} g^{\chi j} (\partial_j Y) && \text{(D.9)} \end{aligned}$$

where i and j are θ or χ. The operator $\nabla \cdot (\frac{1}{B^2}\nabla_\perp)$ has been expressed in covariant notations, as justified in the previous section. This corresponds to several terms for the computation of the polarization stress of momentum, Eq. (G.2) and (G.4). Because of the periodicity in θ, there is no surface term resulting from the integration by parts on $i = \theta$.

$$\mathcal{I} = -\int \mathrm{d}\chi \mathrm{d}\theta \mathrm{d}\varphi \frac{\sqrt{g}}{B^2} (\partial_\varphi \nabla_\perp X) \cdot \nabla_\perp Y + \int \mathrm{d}\theta \mathrm{d}\varphi \frac{\sqrt{g}}{B^2} R^2 (\nabla\varphi \cdot \nabla X)(\nabla\chi \cdot \nabla_\perp Y) \tag{D.10}$$

Notice that $\nabla\chi \cdot \nabla_\perp Y = \nabla\chi \cdot \nabla Y$, since $\nabla\varphi \cdot \nabla\chi = 0$. Finally, we find

$$\begin{aligned} \mathcal{I} = \int \frac{\mathrm{d}\theta \mathrm{d}\varphi}{(\mathbf{B} \cdot \nabla\theta)} \partial_\varphi X \nabla \cdot \left(\frac{1}{B^2} \nabla_\perp Y \right) = & - \int \frac{\mathrm{d}\theta \mathrm{d}\varphi}{(\mathbf{B} \cdot \nabla\theta)} \frac{1}{B^2} (\partial_\varphi \nabla_\perp X) \cdot \nabla_\perp Y \\ & + \partial_\chi \int \frac{\mathrm{d}\theta \mathrm{d}\varphi}{(\mathbf{B} \cdot \nabla\theta)} \frac{R^2}{B^2} (\nabla\varphi \cdot \nabla X)(\nabla\chi \cdot \nabla Y) \end{aligned} \tag{D.11}$$

Appendix E

Effect of the electric potential on the toroidal canonical momentum

The objective of this appendix is to prove that $d_t P_\varphi = -e\partial_\varphi \bar{\phi}$. Because P_φ is an invariant of the equilibrium motion, this result is equivalent to proving that $\left[e\bar{\phi}, P_\varphi\right] = e\partial_\varphi \bar{\phi}$ where $[.,.]$ indicate the Poisson brackets. In the gyrokinetic framework, we recall the expression of the Poisson brackets for two given fields G and H

$$B_{||}^* [G, H] = -\frac{1}{e}\mathbf{b} \cdot \{\nabla G \times \nabla H\} + \mathbf{B}^* \cdot \left\{\nabla G \partial_{mv_{G\parallel}} H - \partial_{mv_{G\parallel}} G \nabla H\right\} \tag{E.1}$$

where $\mathbf{b} = \mathbf{B}/B$ is the unit vector parallel to the magnetic field and we define $\mathbf{B}^* = \mathbf{B} + (mv_{G\parallel}/e)\nabla \times \mathbf{b}$. In the chosen coordinate system, we recall that the magnetic field $\mathbf{B}$ and the toroidal canonical momentum P_φ can be written as

$$\mathbf{B} = I\nabla\varphi + \nabla\varphi \times \nabla\chi \tag{E.2}$$

$$P_\varphi = -e\chi + \frac{mI}{B} v_{G\parallel} \tag{E.3}$$

where I is a flux function. Using this we can write

$$\begin{aligned} -eB_{||}^* \left[\bar{\phi}, P_\varphi\right] \;=\; & -\nabla\bar{\phi} \cdot \left\{-e\left(1 - \frac{mv_{G\parallel}}{eB}\partial_\chi I\right)\mathbf{b} \times \nabla\chi \right. \\ & \left. -\frac{mIv_{G\parallel}}{B^2}\mathbf{b} \times \nabla B + \frac{eI}{B}\mathbf{B} + \frac{mIv_{G\parallel}}{B}\nabla \times \mathbf{b}\right\} \end{aligned} \tag{E.4}$$

Using the expression of $\mathbf{B}$ given by (E.2) we find that

$$\mathbf{B} \times \nabla\chi = I\mathbf{B} - B^2R^2\nabla\varphi \tag{E.5}$$

$$\nabla \times \mathbf{B} = -\partial_\chi I\mathbf{B} - R^2\partial_\chi P\nabla\varphi \tag{E.6}$$

where P is the plasma pressure. Thus equation (E.4) becomes

$$-eB_{||}^* \left[\bar{\phi}, P_\varphi\right] = -eR^2\nabla\bar{\phi} \cdot \nabla\varphi \left\{B - \frac{mv_{G\parallel}}{e}\partial_\chi I - \frac{mIv_{G\parallel}}{eB^2}\partial_\chi P\right\} \tag{E.7}$$

We can identify $B_{||}^*$ in this expression:

$$B_{||}^* = B - \frac{mv_{G\parallel}}{e}\partial_\chi I - \frac{mv_{G\parallel}}{e}R^2\partial_\chi P \underbrace{\frac{\mathbf{B} \cdot \nabla\varphi}{B^2}}_{=I/B^2R^2}$$

In the chosen system of coordinates we also have $\nabla\bar{\phi}\cdot\nabla\varphi = \partial_\varphi\bar{\phi}/R^2$, therefore equation (E.7) becomes

$$-eB_{||}^{*}\left[\bar{\phi}, P_\varphi\right] = -eB_{||}^{*}\partial_\varphi\bar{\phi} \tag{E.8}$$

Appendix F

Recurrence and closure for the conservation of toroidal momentum

Eq.(3.23) is consistent with the equation derived by Parra and Catto [PC10], as we can show by using a recurrence relation to prove the conservation law for toroidal momentum. Indeed, multiplying the gyrokinetic equation (2.18) by $(u_\varphi)^k$, and using $d_t P_\varphi = -e\partial_\varphi \bar{\phi}$, one gets the recurrence relation

$$\partial_t L_k + \partial_\chi \Pi_k = k\frac{e}{m}\left(\Pi_{k-1} - M_{k-1}\right) \tag{F.1}$$

where

$$\begin{aligned}
L_k &= \sum_{species} \int \mathrm{d}\tau^* \bar{F} m u_\varphi^k && \text{(F.2)}\\
\Pi_k &= \sum_{species} \int \mathrm{d}\tau^* \bar{F} m u_\varphi^k v_G^\chi && \text{(F.3)}\\
M_k &= \sum_{species} \int \mathrm{d}\tau^* \bar{F} m u_\varphi^k \partial_\varphi \bar{\phi} && \text{(F.4)}
\end{aligned}$$

Obviously, Eq.(3.23) corresponds to Eq.(F.1) for $k = 1$. The ordering chosen by Parra and Catto leads them to neglecting the left-hand side of Eq.(F.1) for $k = 3$. In that case, $M_2 \simeq \Pi_2$ and

$$\begin{aligned}
\Pi_1 &= M_1 + \frac{m}{2e}\partial_\chi M_2 + \frac{m}{2e}\partial_t L_2\\
&= m\left\langle \partial_\varphi\bar{\phi}\int \mathrm{d}^3v \bar{F} u_\varphi \right\rangle + \frac{m}{2e}\partial_\chi \left\langle \partial_\varphi\bar{\phi}\int \mathrm{d}^3v \bar{F} m u_\varphi^2 \right\rangle + \frac{m}{2e}\partial_t \left\langle \int \mathrm{d}^3v \bar{F} m u_\varphi^2 \right\rangle \quad \text{(F.5)}
\end{aligned}$$

In the limit $\Pi_0 = \mathcal{J}^\chi = 0$ (vanishing radial current of gyrocenters) and $M_0 = 0$ (no Maxwell stress tensor), one recovers the conservation equation in [PC10]. We note however that this conservation relies on a closure assumption. Although this closure appears reasonable, we believe that Eq.(3.23) is more appropriate, because it is exact within the framework of the gyrokinetic model, but also because it does not involve a time derivative of the pressure in the r.h.s. (like the last term of Eq.(F.5)), which is delicate to compute numerically with accuracy.

Appendix G

Polarization stress

In this appendix, we compute the following integral from Eq. (3.23).

$$
\begin{aligned}
\partial_\chi T^\chi_\varphi &= \sum_{species} e \int \mathrm{d}\tau^* \bar{F} \partial_\varphi \bar{\phi} \\
&= \underbrace{\sum_{species} e \int \mathrm{d}\tau^* (J \cdot \bar{F}) \partial_\varphi \phi +}_{\mathcal{I}_1} \underbrace{\sum_{species} e \int \mathrm{d}\tau^* \left\{ \bar{F} \partial_\varphi \left(J \cdot \phi \right) - (J \cdot \bar{F}) \partial_\varphi \phi \right\}}_{\mathcal{I}_2}
\end{aligned}
\tag{G.1}
$$

In order to compute the first integral, we use the gyrokinetic quasi-neutrality equation (2.16). The first polarization term in expression (G.1) becomes

$$
\mathcal{I}_1 = -\int \frac{\mathrm{d}\theta \mathrm{d}\varphi}{\mathbf{B} \cdot \nabla\theta} \partial_\varphi \phi \nabla \cdot \left\{ \frac{n_{eq} m}{B^2} \nabla_\perp \phi \right\} \tag{G.2}
$$

We can integrate by parts this expression (see appendix D.2 for details), which yields

$$
\begin{aligned}
\mathcal{I}_1 &= \int \frac{\mathrm{d}\theta \mathrm{d}\varphi}{\mathbf{B} \cdot \nabla\theta} \frac{n_{eq} m}{B^2} \underbrace{\partial_\varphi \left(\nabla_\perp \phi \right) \cdot \nabla_\perp \phi}_{\frac{1}{2} \partial_\varphi |\nabla_\perp \phi|^2} - \partial_\chi \int \frac{\mathrm{d}\theta \mathrm{d}\varphi}{\mathbf{B} \cdot \nabla\theta} \frac{n_{eq} m}{B^2} R^2 \left(\nabla\varphi \cdot \nabla\phi \right) \left(\nabla\chi \cdot \nabla\phi \right) \\
&= -\partial_\chi \int \frac{\mathrm{d}\theta \mathrm{d}\varphi}{\mathbf{B} \cdot \nabla\theta} \frac{n_{eq} m}{B^2} \partial_\varphi \phi \left(\nabla\chi \cdot \nabla\phi \right)
\end{aligned}
\tag{G.3}
$$

In order to compute the second integral in (G.1), we use the low wavenumber approximation of the gyroaverage operator

$$
J \simeq 1 + \frac{1}{2} \nabla \cdot \left(\frac{m\mu}{e^2 B} \nabla_\perp \right)
$$

With this approximation, the integral can be written

$$
\mathcal{I}_2 = \frac{m}{2e} \int \mathrm{d}\tau^* \bar{F} \partial_\varphi \left[\nabla \cdot \left(\frac{\mu}{B} \nabla_\perp \phi \right) \right] - \frac{m}{2e} \int \mathrm{d}\tau^* \partial_\varphi \phi \nabla \cdot \left(\frac{\mu}{B} \nabla_\perp \bar{F} \right) \tag{G.4}
$$

The sum over species is omitted for simplicity as the calculation is independent for each species. We can integrate both these terms by parts as done previously for $\mathcal{I}_1$ (see appendix D.2 for details), which leads to

$$
\begin{aligned}
\mathcal{I}_2 = &- \frac{m}{2e} \partial_\chi \int \mathrm{d}\tau^* \frac{\mu}{B} R^2 \left(\nabla\varphi \cdot \nabla\bar{F} \right) \left(\nabla\chi \cdot \nabla\phi \right) + \frac{m}{2e} \int \mathrm{d}\tau^* \frac{\mu}{B} \partial_\varphi \left(\nabla_\perp \bar{F} \right) \cdot \nabla_\perp \phi \\
&- \frac{m}{2e} \partial_\chi \int \mathrm{d}\tau^* \frac{\mu}{B} R^2 \left(\nabla\varphi \cdot \nabla\phi \right) \left(\nabla\chi \cdot \nabla\bar{F} \right) + \frac{m}{2e} \int \mathrm{d}\tau^* \frac{\mu}{B} \partial_\varphi \left(\nabla_\perp \phi \right) \cdot \nabla_\perp \bar{F}
\end{aligned}
$$

Combining the second and fourth terms leads to $\int \mathrm{d}\tau^* \frac{\mu}{B}\partial_\varphi \left(\nabla_\perp\phi \cdot \nabla_\perp \bar{F}\right) = 0$ so we find

$$\mathcal{I}_2 = -\frac{m}{2e}\partial_\chi \int \mathrm{d}\tau^* \frac{\mu}{B} R^2 \left\{\left(\nabla\varphi \cdot \nabla\bar{F}\right)\left(\nabla\chi \cdot \nabla\phi\right) + \left(\nabla\varphi \cdot \nabla\phi\right)\left(\nabla\chi \cdot \nabla\bar{F}\right)\right\} \tag{G.5}$$

Combining equations (G.3) and (G.5), using the gyrocenter perpendicular pressure defined by $\bar{P}_\perp = \int \mathrm{d}^3 v \bar{F} \mu B$, we obtain the complete expression of the polarization terms for the conservation of angular momentum:

$$T^\chi_\varphi = \int \frac{\mathrm{d}\theta \mathrm{d}\varphi}{\mathbf{B}\cdot\nabla\theta} \left\{-\frac{m}{2eB^2}\left(\nabla\chi \cdot \nabla\phi\right)\partial_\varphi \bar{P}_\perp - \frac{m}{2eB^2}\left(\nabla\chi \cdot \nabla\bar{P}_\perp\right)\partial_\varphi\phi - \frac{n_{eq} m}{B^2}\left(\nabla\chi \cdot \nabla\phi\right)\partial_\varphi\phi\right\} \tag{G.6}$$

Appendix H

Radial currents

From the gyrocenter equations of motion, Eq. (2.21), the radial current of gyrocenters $\mathcal{J}^\chi$ can be decomposed into two components, coming respectively from the curvature and $E \times B$ drifts, noted $\mathcal{J}_D^\chi$ and $\mathcal{J}_E^\chi$.

H.1 Neoclassical viscous damping

In this section we derive the radial current due to curvature drift. In the axisymmetric case, it can be verified that the radial current due to curvature drift is of the form

$$\mathcal{J}_D^\chi = -\sum_{species} e \int \mathrm{d}\theta \mathrm{d}\varphi \int 2\pi B \mathrm{d}\mu \mathrm{d}v_{G\parallel} \left(m {v_{G\parallel}}^2 + \mu B \right) I \frac{\partial_\theta B}{B^2} \bar{F} \tag{H.1}$$

where we have used the approximation $B_\parallel^* = B$. This is nothing other than the neoclassical viscous damping term. Indeed equation (H.1) can be recast as

$$\mathcal{J}_D^\chi = -\sum_{species} e \int \mathrm{d}\theta \mathrm{d}\varphi \frac{I}{B} \left(\bar{P}_\parallel + \bar{P}_\perp \right) \partial_\theta \ln B \tag{H.2}$$

which is the conventional fluid expression for the radial current.

An explicit expression for $\mathcal{J}_D^\chi$ can be easily found in the plateau regime for a large aspect-ratio tokamak, i.e. when the ratio of the minor radius to the major radius is small. In this high collisionality regime, the quasi-linear approach can be followed, modeling the collision operator as a simple resonance broadening. For this neoclassical derivation, as we are only interested in the large scales, we consider the gyroaveraging operator $J \simeq 1$. We also assume $\mathbf{B}^* = \mathbf{B}$ and $B_\parallel^* = B$. The solution of the kinetic equation reads $\bar{F} = F_M + \delta\bar{F}$ where F_M is a shifted Maxwellian distribution

$$F_M(\chi, v_{G\parallel}, H) = \frac{n_{eq} \exp\left(e\phi_{eq}/T_{eq} \right)}{\left(2\pi T_{eq}/m \right)^{3/2}} \exp\left(-\frac{H}{T} \right) \left(1 + \frac{m v_{G\parallel} V_\parallel}{T_{eq}} \right) \tag{H.3}$$

where H is the energy, i.e. $H = m{v_{G\parallel}}^2 + \mu B + e\phi_{eq}$. The mean density n_{eq}, temperature T_{eq} and potential ϕ_{eq} are functions of χ only. The radial current is dominated by the ion contribution. Assuming a simplified geometry of concentric toroidal magnetic flux surfaces with circular cross-sections, the magnetic field amplitude is $B = B_0(r) \left[1 - (r/R) \cos\theta \right]$ where B_0 is constant on a given flux-surface and r (respectively R) is the minor (resp.

major) radius. As the aim is to compute the radial current, we focus only on the resonant part of $\delta\bar{F}$ (i.e. in $\sin\theta$) which contributes to transport [HS02]:

$$\delta\bar{F}_{res} = \pi\,\delta\left(\frac{v_{G\parallel}}{qR}\right)\left(m{v_{G\parallel}}^2 + \mu B\right) I\frac{\partial_\theta B}{B^2}\frac{\mu R}{e}\left\{\partial_r - \frac{erB_0}{mqR}\partial_{v_{G\parallel}}\right\}F_M \tag{H.4}$$

where $q = \mathbf{B}\cdot\nabla\varphi/\mathbf{B}\cdot\nabla\theta$ is the safety factor. Using the expression of F_M in equation (H.3), we can compute the radial flux $\langle(\mathbf{v}_D\cdot\nabla\chi)\delta\bar{F}\rangle$, which leads to

$$\mathcal{J}_D^\chi = -\sqrt{\frac{\pi}{2}}\frac{n_{eq}m}{B^2}\frac{qv_T}{R}\left(\partial_\chi\langle\phi\rangle - \partial_\chi\langle\phi_{neo}\rangle\right) \tag{H.5}$$

where we define

$$\partial_\chi\langle\phi_{neo}\rangle = \frac{B}{I}V_{\parallel eq} - \frac{T_{eq}}{e}\partial_\chi \ln n_{eq} - \frac{3}{2}\frac{T_{eq}}{e}\partial_\chi \ln T_{eq} \tag{H.6}$$

Note that, when the system is completely axisymmetric, there is a degeneracy between the radial electric field and the parallel velocity. Using the radial force balance equation (3.39), Eq. (H.6) can be interpreted either as an equation on the radial electric field or on the poloidal velocity. Hence the equation $\partial_t\sigma = -\mathcal{J}_D^\chi$ can be seen as describing the relaxation of the poloidal velocity towards the neoclassical value with a damping rate of the order of qv_T/R. Indeed the force balance equation Eq.(3.39) implies that $\mathbf{V}\cdot\nabla\theta$ must relax towards $-1/(2qe)\partial_\chi T_{eq}$. As expected, radial transport in the plateau regime does not depend on the value of the collision frequency. In the banana regime, calculation leads to a similar equation with the appropriately modified damping rate and poloidal velocity.

H.2 Taylor theorem

We define, for a given vector $\mathbf{H}$, the projection on the local flux-surface as

$$H_\wedge = \left(\frac{\mathbf{B}}{B^2}\times\nabla\chi\right)\cdot\mathbf{H} \tag{H.7}$$

In this section, we assume, for any scalar field h, that $J\cdot(\nabla h)_\wedge = (J\cdot\nabla h)_\wedge$, i.e. the radial projection of the gradient and the gyroaveraging operator commute. This is a fairly reasonable assumption, equivalent to ignoring the gyroaverage of metric elements, which are of the order $\mathcal{O}(\rho_*^2)$. Nevertheless, since exact conservation laws are required for numerical tests, the following expressions should not be used for this purpose. Within this approximation, following the same general method used in appendix G, the $E\times B$ drift contribution to the radial current is found to be

$$\mathcal{J}_E^\chi = -\partial_\chi T_\wedge^\chi \tag{H.8}$$

with

$$T_\wedge^\chi = -\int\frac{\mathrm{d}\theta\mathrm{d}\varphi}{\mathbf{B}\cdot\nabla\theta}\left\{\frac{n_{eq}m}{B^2}E^\chi E_\wedge + \sum_{species}\frac{1}{2}\frac{m}{eB^2}\left(E^\chi\mathcal{G}_\wedge + \mathcal{G}^\chi E_\wedge\right)\right\} \tag{H.9}$$

Given the definition of the radial projection Eq. (H.7), $E_\wedge$ and $\mathcal{G}_\wedge$ can be understood as projections of the perpendicular gradients of $\bar{\phi}$ and $\bar{P}_\perp$ on the local flux-surface. The expressions (H.8) and (H.9) require comment. Note that, at least in slab geometry, we recover the standard fluid expression of the polarization current including the correct diamagnetic contribution, as the factor 1/2 in front of the pressure gradients results from the presence of pressure terms in the definition of the generalized vorticity Eq. (3.31). A comparison with Eq.(3.29) indicates that $T_{\wedge}^{\chi}$ is an off-diagonal component of the Maxwell stress tensor constructed from the polarization field (corrected for FLR effets). However another interpretation of the vorticity is possible. In the cold plasma limit $\bar{P}_{\perp} = 0$, $T_{\wedge}^{\chi}$ is the off-diagonal component of the Reynolds stress tensor. Since σ is then proportional to the poloidal component of the $E \times B$ drift velocity, one recovers the usual expression for the time evolution of the poloidal velocity. In other words, it is found that the flux of vorticity is related to the Reynolds stress, a restatement of Taylor's theorem [Tay15].

Appendix I

Radial force balance equation

In this appendix, we recover the conventional fluid expression for the radial force balance. In the absence of turbulence and collisions, the solution of the gyrokinetic equation (2.18) is a function of the motion invariants: the energy $H = \varepsilon + e\phi_{eq}$ ($\varepsilon = m{v_{G\parallel}}^2/2 + \mu B$ is the kinetic energy, and ϕ_{eq} is the mean electric potential); the magnetic moment μ and the toroidal canonical momentum,

$$P_\varphi = mu_\varphi - e\chi \tag{I.1}$$

with the notation $u_\varphi = (I/B)v_{G\parallel}$. The solution of $\mathcal{C}(\bar{F}) = 0$ (applied to all species) is a Maxwellian. Except in the trivial case where all gradients are vanishing, the presence of particle trapping implies that no solution satisfies both constraints, i.e. no Maxwellian distribution can be found as a function of the motion invariants. The resolution of this dilemma can be seen as the origin of neoclassical transport. However, far from the trapped domain, a solution which satisfies both constraints *can* be found. It is of the form [GDPN+09]

$$F_M\left(H,\mu,P_\varphi\right) = \frac{n_{eq}\exp\left(e\phi_{eq}/T_{eq}\right)}{\left(2\pi T_{eq}/m\right)^{3/2}}\exp\left(-\frac{H}{T_{eq}}\right)\left(1+\frac{mWhv_{G\parallel}}{T_{eq}}\right) \tag{I.2}$$

where the density n_{eq}, temperature T_{eq} and potential ϕ_{eq} are functions of $-P_\varphi/e$ (which is approximately equal to χ at order $\mathcal{O}(\rho_*)$), $hv_{G\parallel}$ is a *motion invariant* close to $v_{G\parallel}$ and the function W is given by

$$hW = V_{\parallel eq} + \frac{T_{eq}}{e}\frac{I}{B}\partial_\chi \Xi \tag{I.3}$$

where $V_{\parallel eq}$ is the equilibrium toroidal velocity and

$$\partial_\chi \Xi = \partial_\chi \ln n_{eq} + \frac{e}{T_{eq}}\partial_\chi \phi_{eq} + \left(\frac{\varepsilon}{T_{eq}} - \frac{3}{2}\right)\partial_\chi \ln T_{eq} \tag{I.4}$$

The flow associated with this distribution (I.2) is consistent with the general expression in toroidal geometry

$$\mathbf{V} = K(\chi)\mathbf{B} - \left(\partial_\chi \phi_{eq} + \frac{\partial_\chi P_{eq}}{n_{eq}e}\right)R^2\nabla\varphi \tag{I.5}$$

with $K = \int 2\pi B \mathrm{d}\mu \mathrm{d}v_{G\parallel}({v_{G\parallel}}^2/v_T^2)hWF_M$ ($v_T = \sqrt{T_{eq}/m}$ being the thermal velocity). With this flow, the radial component of the force balance equation reads:

$$\partial_\chi \phi_{eq} + \frac{\partial_\chi P_{eq}}{n_{eq}e} + \frac{B}{I}V_{\parallel eq} = q\frac{B^2R^2}{I^2}\left(\mathbf{V}\cdot\nabla\theta\right) \tag{I.6}$$

Note that, in the case of an anisotropic pressure tensor, P_{eq} should be replaced by the perpendicular pressure $P_{eq\perp}$ in the radial force balance Eq. (I.6).

Bibliography

[AGG$^+$11] J. Abiteboul, V. Grandgirard, X. Garbet, S. J. Allfrey, Ph. Ghendrih, G. Latu, Y. Sarazin, and A. Strugarek. Conservation equations and calculation of mean flows in gyrokinetics. *Physics of Plasmas*, 18(8):082503, 2011.

[ALG$^+$11] J. Abiteboul, G. Latu, V. Grandgirard, A. Ratnani, E. Sonnendrücker, and A. Strugarek. Solving the Vlasov equation in complex geometries. In *ESAIM: Proceedings*, volume 32, pages 103–117, 2011.

[ASD89] ASDEX Team. The H-Mode of ASDEX. *Nuclear Fusion*, 29(11):1959, 1989.

[BDT90] H. Biglari, P. H. Diamond, and P. W. Terry. Influence of sheared poloidal rotation on edge turbulence. *Physics of Fluids B*, 2(1):1, 1990.

[BH07] A. J. Brizard and T. S. Hahm. Foundations of nonlinear gyrokinetic theory. *Review of Modern Physics*, 79(2):421, 2007.

[BHG$^+$09] M. Bécoulet, G. Huysmans, X. Garbet, E. Nardon, D. Howell, A. Garofalo, M. Schaffer, T. Evans, K. Shaing, A. Cole, J.-K. Park, and P. Cahyna. Physics of penetration of resonant magnetic perturbations used for Type I edge localized modes suppression in tokamaks. *Nuclear Fusion*, 49(8):085011, 2009.

[BL85] C. K. Birdsall and A. Langdon. *Plasma physics via computer simulation.* McGraw-Hill, New York, 1985.

[BM08] N. Besse and M. Mehrenberger. Convergence of classes of high-order semi-Lagrangian schemes for the Vlasov-Poisson system. *Mathematics of Computation*, 77(61):93, 2008.

[Bri10] A. J. Brizard. Noether derivation of exact conservation laws for dissipationless reduced-fluid models. *Physics of Plasmas*, 17(11):112503, 2010.

[BT11] A. J. Brizard and N. Tronko. Exact momentum conservation laws for the gyrokinetic Vlasov-Poisson equations. *Physics of Plasmas*, 18(8):082307, 2011.

[BTW87] P. Bak, C. Tang, and K. Wiesenfeld. Self-organized criticality: An explanation of the 1/f noise. *Physical Review Letters*, 59(4):381, 1987.

[BVS$^+$11] A. Bottino, T. Vernay, B. Scott, S. Brunner, R. Hatzky, S. Jolliet, B. F. McMillan, T. M. Tran, and L. Villard. Global simulations of tokamak microturbulence: finite-β effects and collisions. *Plasma Physics and Controlled Fusion*, 53(12):124027, 2011.

[BW94] A. Bondeson and D. J. Ward. Stabilization of external modes in tokamaks by resistive walls and plasma rotation. *Physical Review Letters*, 72(17):2709, 1994.

[CAB+09] K. Crombé, Y. Andrew, T. M. Biewer, E. Blanco, P. C. de Vries, C. Giroud, N. C. Hawkes, A. Meigs, T. Tala, M. von Hellermann, K.-D. Zastrow, and JET EFDA Contributors. Radial electric field in JET advanced tokamak scenarios with toroidal field ripple. *Plasma Physics and Controlled Fusion*, 51(5):055005, 2009.

[CBD+10] Y. Camenen, A. Bortolon, B. P. Duval, L. Federspiel, A. G. Peeters, F. J. Casson, W. A. Hornsby, A. N. Karpushov, F. Piras, O. Sauter, A. P. Snodin, and G. Szepesi. Experimental evidence of momentum transport induced by an up-down asymmetric magnetic equilibrium in toroidal plasmas. *Physical Review Letters*, 105(13):135003, 2010.

[CHC07] A. J. Cole, C. C. Hegna, and J. D. Callen. Effect of neoclassical toroidal viscosity on error-field penetration thresholds in tokamak plasmas. *Physical Review Letters*, 99(6):065001, 2007.

[CHS+96] B. A. Carreras, C. Hidalgo, E. Sánchez, M. A. Pedrosa, R. Balbin, I. Garcia-Cortes, B. Van Milligen, D. E. Newman, and V. E. Lynch. Fluctuation-induced flux at the plasma edge in toroidal devices. *Physics of Plasmas*, 3(7):2664, 1996.

[CIJP11] Y. Camenen, Y. Idomura, S. Jolliet, and A. G. Peeters. Consequences of profile shearing on toroidal momentum transport. *Nuclear Fusion*, 51(7):073039, 2011.

[CMS10] N. Crouseilles, M. Mehrenberger, and H. Sellama. Numerical solution of the gyroaverage operator for the finite gyroradius guiding-center model. *Communications in Computational Physics*, 8(3):484, 2010.

[CNLD96] B. A. Carreras, D. Newman, V. E. Lynch, and P. H. Diamond. A model realization of self-organized criticality for plasma confinement. *Physics of Plasmas*, 3(8):2903, 1996.

[CPA+09] Y. Camenen, A. G. Peeters, C. Angioni, F. J. Casson, W. A. Hornsby, A. P. Snodin, and D. Strintzi. Transport of parallel momentum induced by current-symmetry breaking in toroidal plasmas. *Physical Review Letters*, 102(12):125001, 2009.

[CPC+09] F. J. Casson, A. G. Peeters, Y. Camenen, W. A. Hornsby, A. P. Snodin, D. Strintzi, and G. Szepesi. Anomalous parallel momentum transport due to $E \times B$ flow shear in a tokamak plasma. *Physics of Plasmas*, 16(9):092303, 2009.

[CRS67] B. Coppi, M. N. Rosenbluth, and R. Z. Sagdeev. Instabilities due to temperature gradients in complex magnetic field configurations. *Physics of Fluids*, 10(3):582, 1967.

[CW94] J .W. Connor and H .R. Wilson. Survey of theories of anomalous transport. *Plasma Physics and Controlled Fusion*, 36(5):719, 1994.

[CW03a] J. Candy and R. E. Waltz. An Eulerian gyrokinetic-Maxwell solver. *Journal of Computational Physics*, 186(2):545, 2003.

[CW03b] J. Candy and R. E. Waltz. Anomalous transport scaling in the DIII-D tokamak matched by supercomputer simulation. *Physical Review Letters*, 91(4):45001, 2003.

[D$^+$94] P. H. Diamond et al. Dynamics of L-H transition, VH mode evolution, Edge Localized Modes and RF driven confinement control in tokamaks. In *Proceedings of the 15th International Conference on Plasma Physics and Controlled Nuclear Fusion, Seville*, volume 3, page 323. IAEA, 1994.

[DBB$^+$00] A. M. Dimits, G. Bateman, M. A. Beer, B. I. Cohen, W. Dorland, G. W. Hammett, C. Kim, J. E. Kinsey, M. Kotschenreuther, A. H. Kritz, et al. Comparisons and physics basis of tokamak transport models and turbulence simulations. *Physics of Plasmas*, 7(3):969, 2000.

[deG09] J. S. deGrassie. Tokamak rotation sources, transport and sinks. *Plasma Physics and Controlled Fusion*, 51(12):124047, 2009.

[DHCS91] W. D. D'haeseleer, W. N. G. Hitchon, J. D. Callen, and J. L. Shohet. *Flux Coordinates and Magnetic Structure, A Guide to a Fundamental Tool of Plasma Theory.* Springer, Berlin, 1991.

[DIIH05] P. H. Diamond, S. I. Itoh, K. Itoh, and T. S. Hahm. Zonal flows in plasma—a review. *Plasma Physics and Controlled Fusion*, 47(5):R35, 2005.

[DJKR00] W. Dorland, F. Jenko, M. Kotschenreuther, and B. N. Rogers. Electron temperature gradient turbulence. *Physical Review Letters*, 85(26):5579, 2000.

[DK95] R. E. Denton and M. Kotschenreuther. δf algorithm. *Journal of Computational Physics*, 119(2):283, 1995.

[DMG$^+$08] P. H. Diamond, C. J. McDevitt, Ö. D. Gürcan, T. S. Hahm, and V. Naulin. Transport of parallel momentum by collisionless drift wave turbulence. *Physics of Plasmas*, 15(1):012303, 2008.

[DPDG$^+$10] G. Dif-Pradalier, P. H. Diamond, V. Grandgirard, Y. Sarazin, J. Abiteboul, X. Garbet, Ph. Ghendrih, A. Strugarek, S. Ku, and C. S. Chang. On the validity of the local diffusive paradigm in turbulent plasma transport. *Physical Review E*, 82(2):025401, 2010.

[DPDG$^+$11] G. Dif-Pradalier, P. H. Diamond, V. Grandgirard, Y. Sarazin, J. Abiteboul, X. Garbet, Ph. Ghendrih, G. Latu, A. Strugarek, S. Ku, and C. S. Chang. Neoclassical physics in full distribution function gyrokinetics. *Physics of Plasmas*, 18(6):062309, 2011.

[DPGS$^+$08] G. Dif-Pradalier, V. Grandgirard, Y. Sarazin, X. Garbet, Ph. Ghendrih, and P. Angelino. On the influence of initial state on gyrokinetic simulations. *Physics of Plasmas*, 15(4):042315, 2008.

[DPGS+09] G. Dif-Pradalier, V. Grandgirard, Y. Sarazin, X. Garbet, and Ph. Ghendrih. Interplay between gyrokinetic turbulence, flows and collisions: perspectives on transport and poloidal rotation. *Physical Review Letters*, 103(6):065002, 2009.

[DS93] R. R. Dominguez and G. M. Staebler. Anomalous momentum transport from drift wave turbulence. *Physics of Fluids B*, 5:3876, 1993.

[dVSP+08] P. C. de Vries, A. Salmi, V. Parail, C. Giroud, Y. Andrew, T. M. Biewer, K. Crombé, I. Jenkins, T. Johnson, V. Kiptily, A. Loarte, J. Lönnroth, A. Meigs, N. Oyama, R. Sartori, G. Saibene, H. Urano, K.-D. Zastrow, and JET EFDA Contributors. Effect of toroidal field ripple on plasma rotation in JET. *Nuclear Fusion*, 48(3):035007, 2008.

[EJH+04] L.-G. Eriksson, T. Johnson, T. Hellsten, C. Giroud, V. G. Kiptily, K. Kirov, J. Brzozowski, M. DeBaar, J. DeGrassie, M. Mantsinen, A. Meigs, J.-M. Noterdaeme, A. Staebler, D. Testa, A. Tuccillo, and K.-D. Zastrow. Plasma rotation induced by directed waves in the ion-cyclotron range of frequencies. *Physical Review Letters*, 92(23):235001, 2004.

[ES12] D. F. Escande and F. Sattin. Calculation of transport coefficient profiles in modulation experiments as an inverse problem. *Physical Review Letters*, 108(12):125007, 2012.

[FC82] E. A. Frieman and L. Chen. Nonlinear gyrokinetic equations for low-frequency electromagnetic waves in general plasma equilibria. *Physics of Fluids*, 25(3):502, 1982.

[FGG+09] N. Fedorczak, J. P. Gunn, Ph. Ghendrih, P. Monier-Garbet, and A. Pocheau. Flow generation and intermittent transport in the scrape-off-layer of the Tore Supra tokamak. *Journal of Nuclear Materials*, 390(1):368, 2009.

[FGG+11] N. Fedorczak, J. P. Gunn, Ph. Ghendrih, G. Ciraolo, H. Bufferand, L. Isoardi, P. Tamain, and P. Monier-Garbet. Experimental investigation on the poloidal extent of the turbulent radial flux in tokamak scrape-off layer. *Journal of Nuclear Materials*, 415(1):S467, 2011.

[FGT+11] C. Fenzi, X. Garbet, E. Trier, P. Hennequin, C. Bourdelle, T. Aniel, G. Colledani, P. Devynck, C. Gil, Ö. D. Gürcan, L. Manenc, M. Schneider, J.-L. Segui, and the Tore Supra team. On plasma rotation with toroidal magnetic field ripple and no external momentum input. *Nuclear Fusion*, 51(10):103038, 2011.

[FSB01] F. Filbet, E. Sonnendrücker, and P. Bertrand. Conservative numerical schemes for the Vlasov equation. *Journal of Computational Physics*, 172(1):166, 2001.

[GAS+10] X. Garbet, J. Abiteboul, Y. Sarazin, A. Smolyakov, S. Allfrey, V. Grandgirard, Ph. Ghendrih, G. Latu, and A. Strugarek. Entropy production rate in tokamak plasmas with helical magnetic perturbations. *Journal of Physics: Conference Series*, 260(1):012010, 2010.

[GAS$^+$12] X. Garbet, J. Abiteboul, A. Strugarek, Y. Sarazin, G. Dif-Pradalier, Ph. Ghendrih, V. Grandgirard, C. Bourdelle, G. Latu, and A. Smolyakov. Thermodynamics of neoclassical and turbulent transport. *Plasma Physics and Controlled Fusion*, 54(5):055007, 2012.

[GAT$^+$10] X. Garbet, J. Abiteboul, E. Trier, Ö. Gürcan, Y. Sarazin, A. Smolyakov, S. Allfrey, C. Bourdelle, C. Fenzi, V. Grandgirard, Ph. Ghendrih, and P. Hennequin. Entropy production rate in tokamaks with nonaxisymmetric magnetic fields. *Physics of Plasmas*, 17(7):072505, 2010.

[GBB$^+$06] V. Grandgirard, M. Brunetti, P. Bertrand, N. Besse, X. Garbet, Ph. Ghendrih, G. Manfredi, Y. Sarazin, O. Sauter, E. Sonnendrücker, et al. A drift-kinetic semi-Lagrangian 4D code for ion turbulence simulation. *Journal of Computational Physics*, 217(2):395, 2006.

[GBD$^+$07] J. P. Gunn, C. Boucher, M. Dionne, I. Ďuran, V. Fuchs, T. Loarer, I. Nanobashvili, R. Pánek, J. Y. Pascal, F. Saint-Laurent, et al. Evidence for a poloidally localized enhancement of radial transport in the scrape-off layer of the Tore Supra tokamak. *Journal of Nuclear Materials*, 363(1):484, 2007.

[GDH$^+$10] Ö. D. Gürcan, P. H. Diamond, P. Hennequin, C. J. McDevitt, X. Garbet, and C. Bourdelle. Residual parallel Reynolds stress due to turbulence intensity gradient in tokamak plasmas. *Physics of Plasmas*, 17(11):112309, 2010.

[GDHS07] Ö. D. Gürcan, P. H. Diamond, T. S. Hahm, and R. Singh. Intrinsic rotation and electric field shear. *Physics of Plasmas*, 14(4):042306, 2007.

[GDPN$^+$09] X. Garbet, G. Dif-Pradalier, C. Nguyen, Y. Sarazin, V. Grandgirard, and Ph. Ghendrih. Neoclassical equilibrium in gyrokinetic simulations. *Physics of Plasmas*, 16(6):062503, 2009.

[GIVW10] X. Garbet, Y. Idomura, L. Villard, and T.-H. Watanabe. Gyrokinetic simulations of turbulent transport. *Nuclear Fusion*, 50(4):043002, 2010.

[GLB$^+$11] T. Görler, X. Lapillonne, S. Brunner, T. Dannert, F. Jenko, S. K. Aghdam, P. Marcus, B. F. McMillan, F. Merz, O. Sauter, D. Told, and L. Villard. Flux- and gradient-driven global gyrokinetic simulation of tokamak turbulence. *Physics of Plasmas*, 18(5):056103, 2011.

[GS] V. Grandgirard and Y. Sarazin. “Gyrokinetic simulations of magnetic fusion plasmas”. Panoramas et synthèses (in press).

[GSA$^+$07] V. Grandgirard, Y. Sarazin, P. Angelino, A. Bottino, N. Crouseilles, G. Darmet, G. Dif-Pradalier, X. Garbet, Ph. Ghendrih, S. Jolliet, et al. Global full-f gyrokinetic simulations of plasma turbulence. *Plasma Physics and Controlled Fusion*, 49(12B):B173, 2007.

[GSB$^+$99] X. Garbet, Y. Sarazin, P. Beyer, Ph. Ghendrih, R .E. Waltz, M. Ottaviani, and S. Benkadda. Flux driven turbulence in tokamaks. *Nuclear Fusion*, 39(11Y):2063, 1999.

[GSG$^+$02] X. Garbet, Y. Sarazin, Ph. Ghendrih, S. Benkadda, P. Beyer, C. Figarella, and I. Voitsekhovitch. Turbulence simulations of transport barriers with toroidal velocity. *Physics of Plasmas*, 9(9):3893, 2002.

[Hah88] T. S. Hahm. Nonlinear gyrokinetic equations for tokamak microturbulence. *Physics of Fluids*, 31(9):2670, 1988.

[HDGR07] T. S. Hahm, P. H. Diamond, Ö. D. Gürcan, and G. Rewoldt. Nonlinear gyrokinetic theory of toroidal momentum pinch. *Physics of Plasmas*, 14(7):072302, 2007.

[Hen06] P. Hennequin. Scaling laws of density fluctuations in tokamak plasmas. *Comptes Rendus Physique*, 7(6):670, 2006.

[HH76] F. L. Hinton and R. D. Hazeltine. Theory of plasma transport in toroidal confinement systems. *Review of Modern Physics*, 48(2):239, 1976.

[HJKO08] J. A. Heikkinen, S. J. Janhunen, T. P. Kiviniemi, and F. Ogando. Full f gyrokinetic method for particle simulation of tokamak transport. *Journal of Computational Physics*, 227(11):5582, 2008.

[HK92] T. Hwa and M. Kardar. Avalanches, hydrodynamics, and discharge events in models of sandpiles. *Physical Review A*, 45(10):7002, 1992.

[HM92] R. D. Hazeltine and J. D. Meiss. *Plasma Confinement*. Addison-Wesley, Redwood City, 1992.

[HS02] P. Helander and D. J. Sigmar. *Collisional Transport in Magnetized Plasmas*. Cambridge University Press, Cambridge, UK, 2002.

[HVF$^+$10] P. Hennequin, L. Vermare, N. Fedorczak, J. Bernardo, Ö. D. Gürcan, E. Trier, N. Stuyck, C. Fenzi, J. P. Gunn, P. Monier-Garbet, C. Bourdelle, Ph. Ghendrih, and X. Garbet. The effect of SOL flows on edge and core radial electric field and rotation in Tore Supra. In *37th EPS Conference on Plasma Physics, Dublin*, page P1.1040, 2010.

[HW06] F. L. Hinton and R. E. Waltz. Gyrokinetic turbulent heating. *Physics of Plasmas*, 13(10):102301, 2006.

[ICC$^+$10] L. Isoardi, G. Chiavassa, G. Ciraolo, P. Haldenwang, E. Serre, Ph. Ghendrih, Y. Sarazin, F. Schwander, and P. Tamain. Penalization modeling of a limiter in the Tokamak edge plasma. *Journal of Computational Physics*, 229(6):2220, 2010.

[ITK03] Y. Idomura, S. Tokuda, and Y. Kishimoto. Global gyrokinetic simulation of ion temperature gradient driven turbulence in plasmas using a canonical Maxwellian distribution. *Nuclear Fusion*, 43(4):234, 2003.

[IUAT09] Y. Idomura, H. Urano, N. Aiba, and S. Tokuda. Study of ion turbulent transport and profile formations using global gyrokinetic full-f Vlasov simulation. *Nuclear Fusion*, 49(6):065029, 2009.

[Jac75] J. D. Jackson. *Classical electrodynamics*. Wiley, New York, 1975.

[JBA+07] S. Jolliet, A. Bottino, P. Angelino, R. Hatzky, T. M. Tran, B. F. McMillan, O. Sauter, K. Appert, Y. Idomura, and L. Villard. A global collisionless PIC code in magnetic coordinates. *Computer Physics Communications*, 177(5):409, 2007.

[JI12] S. Jolliet and Y. Idomura. Plasma size scaling of avalanche-like heat transport in tokamaks. *Nuclear Fusion*, 52(2):023026, 2012.

[KAD+12] S. Ku, J. Abiteboul, P. H. Diamond, G. Dif-Pradalier, J. M. Kwon, Y. Sarazin, T. S. Hahm, X. Garbet, C. S. Chang, G. Latu, E. S. Yoon, Ph. Ghendrih, S. Yi, A. Strugarek, W. Solomon, and V. Grandgirard. Physics of intrinsic rotation in flux-driven ITG turbulence. *Nuclear Fusion*, 52(6):063013, 2012.

[KCA+06] S. Ku, C.-S. Chang, M. Adams, J. Cummings, F. Hinton, D. Keyes, S. Klasky, W. Lee, Z. Lin, S. Parker, and the CPES team. Gyrokinetic particle simulation of neoclassical transport in the pedestal/scrape-off region of a tokamak plasma. *Journal of Physics: Conference Series*, 46:87, 2006.

[KCD09] S. Ku, C. S. Chang, and P. H. Diamond. Full-f gyrokinetic particle simulation of centrally heated global ITG turbulence from magnetic axis to edge pedestal top in a realistic tokamak geometry. *Nuclear Fusion*, 49(11):115021, 2009.

[KDG91] Y. B. Kim, P. H. Diamond, and R. J. Groebner. Neoclassical poloidal and toroidal rotation in tokamaks. *Physics of Fluids B*, 3(8):2050, 1991.

[KDG10] Y. Kosuga, P. H. Diamond, and Ö. D. Gürcan. On the efficiency of intrinsic rotation generation in tokamaks. *Physics of Plasmas*, 17(10):2313, 2010.

[KMS95] B. N. Kuvshinov, A. B. Mikhailovskii, and S. E. Sharapov. Plasma rotation in a rippled-field tokamak in the absence of a fast-ion beam. *Plasma Physics Reports*, 21:713, 1995.

[Kov99] L. M. Kovrizhnykh. Plasma rotation in stellarators and rippled tokamaks. *Plasma Physics Reports*, 21:760, 1999.

[KYR+12] J. M. Kwon, S. Yi, T. Rhee, P. H. Diamond, K. Miki, T. S. Hahm, J. Y. Kim, Ö. D. Gürcan, and C. McDevitt. Analysis of symmetry breaking mechanisms and the role of turbulence self-regulation in intrinsic rotation. *Nuclear Fusion*, 52(1):013004, 2012.

[Lan36] L. D. Landau. The kinetic equation in the case of Coulomb interactions. *Phys. Z. Sowj. Union*, 10, 1936.

[Law57] J. D. Lawson. Some criteria for a power producing thermonuclear reactor. *Proceedings of the Physical Society*, B70:6, 1957.

[LB58] A. Lenard and I. B. Bernstein. Plasma oscillations with diffusion in velocity space. *Physical Review*, 112(5):1456, 1958.

[Lee83] W. W. Lee. Gyrokinetic approach in particle simulation. *Physics of Fluids*, 26(2):556, 1983.

[LEHT02] Z. Lin, S. Ethier, T. S. Hahm, and W. M. Tang. Size scaling of turbulent transport in magnetically confined plasmas. *Physical Review Letters*, 88(19):195004, 2002.

[LHL+98] Z. Lin, T. S. Hahm, W. W. Lee, W. M. Tang, and R. B. White. Turbulent transport reduction by zonal flows: Massively parallel simulations. *Science*, 281(5384):1835, 1998.

[LHL+99] Z. Lin, T. S. Hahm, W. W. Lee, W. M. Tang, and P. H. Diamond. Effects of collisional zonal flow damping on turbulent transport. *Physical Review Letters*, 83(18):3645, 1999.

[LRH+04] B. LaBombard, J. E. Rice, A. E. Hubbard, J. W. Hughes, M. Greenwald, J. Irby, Y. Lin, B. Lipschultz, E. S. Marmar, C. S. Pitcher, et al. Transport-driven Scrape-Off-Layer flows and the boundary conditions imposed at the magnetic separatrix in a tokamak plasma. *Nuclear Fusion*, 44(10):1047, 2004.

[MDGH09a] C. J. McDevitt, P. H. Diamond, Ö. D. Gürcan, and T. S. Hahm. A novel mechanism for exciting intrinsic toroidal rotation. *Physics of Plasmas*, 16(5):052302, 2009.

[MDGH09b] C. J. McDevitt, P. H. Diamond, Ö. D. Gürcan, and T. S. Hahm. Toroidal rotation driven by the polarization drift. *Physical Review Letters*, 103(20):205003, 2009.

[Mik95] A. B. Mikhailovskii. Plasma rotation in a rippled-field tokamak. *Plasma Physics Reports*, 21:529, 1995.

[MJT+09] B. F. McMillan, S. Jolliet, T. M. Tran, L. Villard, A. Bottino, and P. Angelino. Avalanchelike bursts in global gyrokinetic simulations. *Physics of Plasmas*, 16(2):022310, 2009.

[MLB+10] B. F. McMillan, X. Lapillonne, S. Brunner, L. Villard, S. Jolliet, A. Bottino, T. Görler, and F. Jenko. System size effects on gyrokinetic turbulence. *Physical Review Letters*, 105(15):155001, 2010.

[MOT77] W. M. Manheimer, E. Ott, and W. M. Tang. Anomalous electron-ion energy exchange from the trapped electron mode. *Physics of Fluids*, 20(5):806, 1977.

[NII+11] Y. Nagashima, S. I. Itoh, S. Inagaki, H. Arakawa, N. Kasuya, A. Fujisawa, K. Kamataki, T. Yamada, S. Shinohara, S. Oldenbürger, M. Yagi, Y. Takase, P. H. Diamond, and K. Itoh. Non-Gaussian properties of global momentum and particle fluxes in a cylindrical laboratory plasma. *Physics of Plasmas*, 18(7):070701, 2011.

[NJE+10] M. F. F. Nave, T. Johnson, L.-G. Eriksson, K. Crombé, C. Giroud, M.-L. Mayoral, J. Ongena, A. Salmi, T. Tala, and M. Tsalas. Influence of magnetic field ripple on the intrinsic rotation of tokamak plasmas. *Physical Review Letters*, 105(10):105005, 2010.

[Noe18] E. Noether. Invariante Variationsprobleme. *Nachr. d. König. Gesellsch. d. Wiss. zu Göttingen, Math-phys. Klasse*, pages 235–257, 1918.

[OBC$^+$97] M. Ottaviani, M. A. Beer, S. C. Cowley, W. Horton, and J. A. Krommes. Unanswered questions in ion-temperature-gradient-driven turbulence. *Physics Reports*, 283(1):121, 1997.

[PAA05] A. G. Peeters, C. Angioni, and ASDEX Upgrade Team. Linear gyrokinetic calculations of toroidal momentum transport in a tokamak due to the ion temperature gradient mode. *Physics of Plasmas*, 12(7):072515, 2005.

[PAS07] A. G. Peeters, C. Angioni, and D. Strintzi. Toroidal momentum pinch velocity due to the Coriolis drift effect on small scale instabilities in a toroidal plasma. *Physical Review Letters*, 98(26):265003, 2007.

[PC08] F. I. Parra and P. J. Catto. Limitations of gyrokinetics on transport time scales. *Plasma Physics and Controlled Fusion*, 50(6):065014, 2008.

[PC10] F. I. Parra and P. J. Catto. Transport of momentum in full f gyrokinetics. *Physics of Plasmas*, 17(5):056106, 2010.

[PLB$^+$95] C. C. Petty, T. C. Luce, K. H. Burrell, S. C. Chiu, J. S. deGrassie, C. B. Forest, P. Gohil, C. M. Greenfield, R. J. Groebner, R. W. Harvey, R. I. Pinsker, R. Prater, R. E. Waltz, R. A. James, and D. Wròblewski. Nondimensional transport scaling in DIII-D: Bohm versus gyro-Bohm resolved. *Physics of Plasmas*, 2(6):2342, 1995.

[PPJ$^+$08] P. A. Politzer, C. C. Petty, R. J. Jayakumar, T. C. Luce, M. R. Wade, J. C. DeBoo, J. R. Ferron, P. Gohil, C. T. Holcomb, A. W. Hyatt, et al. Influence of toroidal rotation on transport and stability in hybrid scenario plasmas in DIII-D. *Nuclear Fusion*, 48(7):075001, 2008.

[PSC$^+$09] A. G. Peeters, D. Strintzi, Y. Camenen, C. Angioni, F. J. Casson, W. A. Hornsby, and A. P. Snodin. Influence of the centrifugal force and parallel dynamics on the toroidal momentum transport due to small scale turbulence in a tokamak. *Physics of Plasmas*, 16(4):042310, 2009.

[RH98] M. N. Rosenbluth and F. L. Hinton. Poloidal flow driven by ion-temperature-gradient turbulence in tokamaks. *Physical Review Letters*, 80(4), 1998.

[RICd$^+$07] J. E. Rice, A. Ince-Cushman, J. S. deGrassie, L.-G. Eriksson, Y. Sakamoto, A. Scarabosio, A. Bortolon, K. H. Burrell, B. P. Duval, C. Fenzi-Bonizec, M. J. Greenwald, R. J. Groebner, G. T. Hoang, Y. Koide, E. S. Marmar, A. Pochelon, and Y. Podpaly. Inter-machine comparison of intrinsic toroidal rotation in tokamaks. *Nuclear Fusion*, 47(11):1618, 2007.

[Rid97] T. H. Rider. Fundamental limitations on plasma fusion systems not in thermodynamic equilibrium. *Physics of Plasmas*, 4(4):1039, 1997.

[SC91] A. Staniforth and J. Côté. Semi-Lagrangian integration schemes for atmospheric models: A review. *Monthly Weather Review*, 119(9):2206–2223, 1991.

[SCH$^+$90] J. A. Snipes, D. J. Campbell, T. C. Hender, M. Von Hellermann, and H. Weisen. Plasma stored energy and momentum losses during large MHD activity in JET. *Nuclear Fusion*, 30(2):205, 1990.

[SG98] Y. Sarazin and Ph. Ghendrih. Intermittent particle transport in two-dimensional edge turbulence. *Physics of Plasmas*, 5(12):4214, 1998.

[SGA$^+$10] Y. Sarazin, V. Grandgirard, J. Abiteboul, S. Allfrey, X. Garbet, Ph. Ghendrih, G. Latu, A. Strugarek, and G. Dif-Pradalier. Large scale dynamics in flux driven gyrokinetic turbulence. *Nuclear Fusion*, 50(5):054004, 2010.

[SGA$^+$11] Y. Sarazin, V. Grandgirard, J. Abiteboul, S. Allfrey, X. Garbet, Ph. Ghendrih, G. Latu, A. Strugarek, G. Dif-Pradalier, P. H. Diamond, S. Ku, C. S. Chang, B. F. McMillan, T. M. Tran, L. Villard, S. Jolliet, A. Bottino, and P. Angelino. Predictions on heat transport and plasma rotation from global gyrokinetic simulations. *Nuclear Fusion*, 51(10):103023, 2011.

[SGF$^+$05] Y. Sarazin, V. Grandgirard, E. Fleurence, X. Garbet, Ph. Ghendrih, P. Bertrand, and G. Depret. Kinetic features of interchange turbulence. *Plasma Physics and Controlled Fusion*, 47(10):1817, 2005.

[Sha96] K. C. Shaing. Theory of high-mode phenomena for stellarators. *Physical Review Letters*, 76(23):4364, 1996.

[Sha03] K. C. Shaing. Magnetohydrodynamic-activity-induced toroidal momentum dissipation in collisionless regimes in tokamaks. *Physics of Plasmas*, 10(5):1443, 2003.

[SLP05] N. Smick, B. LaBombard, and C. S. Pitcher. Plasma profiles and flows in the high-field side scrape-off layer in Alcator C-Mod. *Journal of Nuclear Materials*, 337(1):281, 2005.

[SRBG99] E. Sonnendrücker, J. Roche, P. Bertrand, and A. Ghizzo. The semi-Lagrangian method for the numerical resolution of the Vlasov equation. *Journal of Computational Physics*, 149(2):201, 1999.

[SS10] B. D. Scott and J. Smirnov. Energetic consistency and momentum conservation in the gyrokinetic description of tokamak plasmas. *Physics of Plasmas*, 17(11):112302, 2010.

[SSDP$^+$10] Y. Sarazin, A. Strugarek, G. Dif-Pradalier, J. Abiteboul, S. Allfrey, X. Garbet, Ph. Ghendrih, V. Grandgirard, and G. Latu. Flux-driven gyrokinetic simulations of ion turbulent transport at low magnetic shear. *Journal of Physics: Conference Series*, 260(1):012017, 2010.

[SSK$^+$12] R. Singh, R. Singh, P. Kaw, Ö. D. Gürcan, P. H. Diamond, and H. Nordman. Symmetry breaking effects of density gradient on parallel momentum transport: A new ρ_s^* effect. *Physics of Plasmas*, 19(1):012301, 2012.

[Sta00] P. C. Stangeby. *The plasma boundary of magnetic fusion devices*. Institute of Physics Publishing, Bristol, 2000.

[SvMC05] R. Sanchez, B. P. van Milligen, and B. A. Carreras. Probabilistic transport models for plasma transport in the presence of critical thresholds: Beyond the diffusive paradigm. *Physics of Plasmas*, 12(5):056105, 2005.

[Tag88] M. Taguchi. Ion thermal conductivity and ion distribution function in the banana regime. *Plasma Physics and Controlled Fusion*, 30(13):1897, 1988.

[Tag93] M. Taguchi. Generation of poloidal electric field by anisotropic heating. *Journal of the Physics Society Japan*, 62(10):3486, 1993.

[Tam07] P. Tamain. *Etude des Flux de Matière dans le Plasma de Bord des Tokamaks : Alimentation, Transport et Turbulence.* PhD thesis, Université de Provence, 2007.

[Tay15] G. I. Taylor. Eddy motion in the atmosphere. *Philosophical Transactions of the Royal Society of London, Series A*, 215:1, 1915.

[TGT+09] P. Tamain, Ph. Ghendrih, E. Tsitrone, Y. Sarazin, X. Garbet, V. Grandgirard, J. Gunn, E. Serre, G. Ciraolo, and G. Chiavassa. 3D modelling of edge parallel flow asymmetries. *Journal of Nuclear Materials*, 390(1):347, 2009.

[UOK+07] H. Urano, N. Oyama, K. Kamiya, Y. Koide, H. Takenaga, T. Takizuka, M. Yoshida, Y. Kamada, and the JT-60 Team. H-mode pedestal structure in the variation of toroidal rotation and toroidal field ripple in JT-60U. *Nuclear Fusion*, 47(7):706, 2007.

[VBB+10] L. Villard, A. Bottino, S. Brunner, A. Casati, J. Chowdhury, T. Dannert, R. Ganesh, X. Garbet, T. Görler, V. Grandgirard, et al. Gyrokinetic simulations of turbulent transport: size scaling and chaotic behaviour. *Plasma Physics and Controlled Fusion*, 52(12):124038, 2010.

[VBV+12] T. Vernay, S. Brunner, L. Villard, B. F. McMillan, S. Jolliet, T. M. Tran, and A. Bottino. Synergy between ion temperature gradient turbulence and neoclassical processes in global gyrokinetic particle-in-cell simulations. *Physics of Plasmas*, 19(4):042301, 2012.

[WCR02] R. E. Waltz, J. M. Candy, and M. N. Rosenbluth. Gyrokinetic turbulence simulation of profile shear stabilization and broken gyroBohm scaling. *Physics of Plasmas*, 9(5):1938, 2002.

[WHE+09] W. X. Wang, T. S. Hahm, S. Ethier, G. Rewoldt, W. W. Lee, W. M. Tang, S. M. Kaye, and P. H. Diamond. Gyrokinetic studies on turbulence-driven and neoclassical nondiffusive toroidal-momentum transport and the effect of residual fluctuations in strong $E \times B$ shear. *Physical Review Letters*, 102(3):35005, 2009.

[WHL+07] W. X. Wang, T. S. Hahm, W. W. Lee, G. Rewoldt, J. Manickam, and W. M. Tang. Nonlocal properties of gyrokinetic turbulence and the role of $E \times B$ flow shear. *Physics of Plasmas*, 14(7):072306, 2007.

[WS08] R. E. Waltz and G. M. Staebler. Gyrokinetic theory and simulation of turbulent energy exchange. *Physics of Plasmas*, 15(1):014505, 2008.

[WSD+97] R. E. Waltz, G. M. Staebler, W. Dorland, G. W. Hammett, M. Kotschenreuther, and J. A. Konings. A gyro-Landau-fluid transport model. *Physics of Plasmas*, 4(7):2482, 1997.

[WSS11] R. E. Waltz, G. M. Staebler, and W. M. Solomon. Gyrokinetic simulation of momentum transport with residual stress from diamagnetic level velocity shears. *Physics of Plasmas*, 18(4):042504, 2011.

[XR91] X. Q. Xu and M. N. Rosenbluth. Numerical simulation of ion-temperature-gradient-driven modes. *Physics of Fluids B*, 3(3):627, 1991.

[YKT$^+$06] M. Yoshida, Y. Koide, H. Takenaga, H. Urano, N. Oyama, K. Kamiya, Y. Sakamoto, Y. Kamada, and the JT-60 Team. Effects of ripple loss of fast ions on toroidal rotation in JT-60U. *Plasma Physics and Controlled Fusion*, 48(11):1673, 2006.

[Yus90] P. N. Yushmanov. *Review of Plasma Physics*, volume 16. Consultants Bureau, New York, 1990.

Index